THEORETIAL ANALYSIS OF OSCILLATING MOTION, HEAT TRANSFER, MINIMUM MENISCUS RADIUS AND CHARGING PROCEDURE IN AN OSCILLATING HEAT PIPE

A Dissertation
presented to
the Faculty of the Graduate School
at the University of Missouri-Columbia

In Partial Fulfillment
of the Requirement for the Degree

Doctor of Philosophy

By

PENG CHENG

Dr. Hongbin Ma, Dissertation Supervisor

December 2008

The undersigned, appointed by the dean of the Graduate School, have examined the dissertation entitled

THEORETIAL ANALYSIS OF OSCILLATING MOTION, HEAT TRANSFER, MINIMUM MENISCUS RADIUS AND CHARGING PROCEDURE IN AN OSCILLATING HEAT PIPE

Presented by Peng Cheng,

a candidate of the degree of doctor of philosophy,

and hereby certify that, in their opinion, it is worthy of acceptance,

_____

Dr. Hongbin Ma

_____

Dr. Yuwen Zhang

_____

Dr. Gary L. Solbrekken

_____

Dr. Qingsong Yu

_____

Dr. Sanju Gupta

ACKNOWLEDGEMENTS

I would like to express my sincere thanks to my advisor, Dr. Hongbin Ma, for his supervision, encouragement and invaluable suggestions throughout this period of study. More importantly, what I have learned from him is beyond the academic research. And I deeply appreciate his Research Assistantship support during my stay at University of Missouri-Columbia.

I am grateful to Dr. Yuwen Zhang, Dr. Gary L. Solbrekken, Dr. Qingsong Yu and Dr. Sanju Gupta for serving as my committee members and for their discussions and suggestions in my research. And my classmates and colleagues in Dr. Ma's group, Brian Borgmeyer (Ph.D candidate), Anjun Jiao (Ph.D), and Corey Wilson (Ph.D candidate) deserve my sincere appreciation for their help and encouragement.

I would like also to say thanks to Melanie Gerlach and Pat Frees for their perfect work and help during my study.

I also want to express my thanks to my wife, my parents and sister, and the coming baby for their support and encouragement.

TABLE OF CONTENTS

LIST OF FIGURES

Figure

LIST OF TABLES

LIST OF SYMBOLS

a	dimensionless crosssectional area
A	Hamaker constant in Section 3.1, J; cross sectional area of tube, m^2
A_{gap}	area of the gap
c	specific heat, J/kg K
c_p	specific heat at constant pressure, J/Kg K
c_v	specific heat at constant volume, J/Kg K
C_T	constant
C_f	friction coefficient
dx	differential length, m
D	diameter of tube ， m
E	potential energy, J
f	friction factor
G	mass flux, $G=\overline{u}\overline{\rho}$, kg/m^2
h	convection heat transfer coefficient (W/m^2 K)
h_{lv}	latent heat of vaporization, J/kg
H	enthalpy, J/kg
$J_{0(1,2)}$	Bessel function of the first kind of order 0 (1, 2)
k	thermal conductivity, W/(m-K); constant in Section 4.2

K	curvature, m^{-1}
L	length, m
m	vapor mass in Chapter 2
$\dot{m}$	mass flow rate, kg/s
M	number of angles around one particle
Ma	Mach number
N	number of the edges in one structure in Eq. (4-17); Number of particles
Nu	Nusselt number
p	pressure, N/m^2
p_{vac}	vacuum pressure, N/m^2
$\Delta p_{c,\max}$	maximum capillary pressure drop, N/m^2
P_{gap}	perimeter of the gap, m
Pr	Prandtl number
P_R	reference pressure, N/ m^2
q	heat transfer, W
$q"$	heat flux, W/ m^2
Q	heat, J
r	radius, m
$r_{c,e}$	effective porous radius, m
R	edge length of structure in Section 4.2, m; gas constant
Re	Reynolds number

S	total area, m^2
t	time, s
T	temperature, K
u	velocity in x-direction, m/s
u'	fluctuating velocity, m/s
$\bar{u}$	mean velocity in x-direction, m/s
v	velocity in y-direction, m/s
V	volume, m^3
W	work, w
x	coordinate, m; coordination of axial direction in Section 3.1.2.2, m; mass percentage in Section 4.1
X	percentage of the edge of the structure
y	coordinate, m
Y	percentage of particle
z	coordinate, m

Greek symbols

α	thermal diffusivity (m^2/s); structure angles in Eqs. (4-17, 18); angle upward in Eqs. (4.-21~25), degree
β	angle downward in Eqs. (4-21~25), degree
δ	film thickness, m
δ_0	non-evaporating film thickness, m

ε	porosity
φ	filled liquid ratio
γ	dimensionless amplitude
μ	viscosity, N-s/m^2
ν	kinematic viscosity (m^2/s)
θ	dimensionless temperature; start angle in Section 4.2
ρ	density, kg/m^3
σ	surface tension, N/m
τ	shear stress, N/ m^2; dimensionless period $2\pi / \omega^*$ in Section 3.1.2.2
ω	frequency

Subscripts

0	initial value; reference state in Chapter 2.
∞	ambient
a	average
b	bottom in Section 3.1.2.1
ba	bulk average value
bm	bulk mean value
c	condenser
d	disjoining
e	evaporator

eff	effecitve
hp	shell of heat pipe
i	structure edges; inside in Section 4.1
j	particle radius
l	liquid; upward angle in Eqs. (4-21~23); left wall in Section 3.1.2.1
lv	liquid-vapor interface
m	mean value; structure in Eq. (4-17); downward angles in Eqs. (4-21~23)
n	node value; particles along the line in Section 4.2
o	outside
r	radius; right wall in Section 3.1.2.1
s	steady state; surface in Section 4.1
sat	saturated
t	temporal
v	vapor
w	wall; wick in Chapter 4
x	angle in one structure
y	angle around one particle

ABSTRACT

With the rapid development of electronic technology, investigation and application of devices with high performance of heat removal have become competitive issues recently. Different from traditional heat transfer strategy, many new promising ideas and technologies were introduced into thermal management, one of which is Oscillating Heat Pipe (OHP). The OHP is a bundle of connected tubes with liquid and vapor sealed in it. Due to the period variation of vapor in the evaporator and condenser during heating, pulsating flow of liquid slugs and vapor plugs is actuated. Convection and phase change heat transfer caused by such kind of pulsating heat flow could dissipate very high heat flow with relatively very small effective thermal conductivity

In the current investigation, a theoretical analysis predicting the oscillating motion, heat transfer, and thin film evaporation occurring in the OHP is developed. The new model predicting the oscillating motion in an OHP can predict the effects of turn number and gravitational force in addition to the liquid charging ratio, operating temperature, working fluid, and heat input. Using the oscillating motion predicted with the new model developed, a heat transfer model predicting the temperature difference between the evaporator and condenser is developed. A comparison with the experimental data shows that the model can be used to predict the heat transfer performance occurring in an OHP.

The thin film evaporation model includes the momentum effect on the thin film profile and evaporation. The model considers the effects of inertial force, disjoining pressure, surface tension, and curvature. Utilizing the order analysis, the model is

simplified and can be numerically solved for the thin film profile, interfacial temperature, meniscus radius, heat flux distribution, velocity distribution, and mass flow rate in the evaporating thin film region. The prediction shows that the inertial force can affect the thin film profile, interfacial temperature, meniscus radius, heat flux distribution, velocity distribution, and mass flow rate, in particular, near the non-evaporating region. It is found that while a maximum velocity, a maximum heat flux, and a maximum curvature exist for a given superheat, the locations for these maximum values are different.

The minimum meniscus radius occurring in the heat pipe determines the maximum capillary heat transport. The accurate prediction of minimum meniscus radii plays a key role in designing a highly efficient heat pipe cooling device. In the current investigation, a mathematical model predicting the minimum meniscus radius occurring in the sintered particles is developed. If the particle size distribution is given, the model can be used to predict the minimum meniscus radii in sintered particles. Moreover, because the charging process directly affects the heat transfer performance occurring in a heat pipe, a theoretical analysis predicting the charging process is conducted. The results provide a guideline for the charging process.

CHAPTER 1 INTRODUCTION

1.1 Overview

As the performance of electronic devices/systems continuously increases, thermal management plays more and more important role in the product development. Two-phase passive devices, e.g. capillary-driven heat pipes, have been proven able to meet the requirement of high heat dissipation in such electronic components/systems [1, 2]. However there exist several limitations in the heat pipes. One of the usually encountered is the capillary limitation, i.e. the heat pipe fails when no enough liquid is pumped back by the wick structure.

Taking advantage of the natural phenomenon of the formation of liquid plugs and vapor bubbles, oscillating heat pipe (OHP) was proposed by Akachi et al. [3]. His idea was to connect in series a bundle of parallel capillary tubes into a meandering tube without the internal capillary structure. Heat is transferred by the oscillating movement of liquid plugs and vapor bubbles plus the phase change heat transfer. The advantages of the oscillating heat pipe includes: the thermally excited oscillating movement; no external mechanical power source required for the fluid transport; phase-change heat transfer combining with forced convection; simple construction and low manufacturing cost. Since then, extensive investigations on the heat transfer

mechanisms and applications of OHP have been conducted experimentally [4-8] and numerically [9-13]. It was found that the heat transfer performance of OHP depends on many factors such as inner diameter of tubes, working fluid, filling ratio, and tilt angle. However, the heat transfer mechanism governing the pulsating phenomena is still vague and not fully understood. Some researchers even suspected the definition of OHP [14]. For example, the slug flow may take a fixed direction when the heat flux increases to a high level, where the OHP could obtain its best performance [15, 16]. It is not a true “pulsating” heat pipe anymore.

According to the description of Akachi and Polasek [3], there are still two shortcomings for the OHP: low heat flux capability due to limited surface area for boiling with the smooth surfaces in the tubes; and limited capability of working fluid against gravity. Hence some researchers attempted to add wicks and capillary transport into the OHP to improve the heat transfer performance, which is also one of research objectives in the current investigation. In order to better understand the heat transfer mechanisms and fluid flow characteristics, an theoretical analysis on the oscillating motion, heat transfer, and thin film evaporation is conducted including dominating factors affecting the heat transfer performance in the OHP.

1.2 Heat Transfer Mechanism of OHP

As mentioned by Akachi [3], the basic heat transfer mechanism in an oscillating heat pipe is sensitive plus phase change heat transfer with the oscillating movement of

the fluid. The movement of liquid slugs and vapor bubbles is caused by the pressure pulsations between the evaporator and condenser. When heat is added on the evaporation region, vaporization of liquid causes the expansion of vapor volume in this region. Simultaneously, condensation of vapor occurring in the condenser region causes the contraction of vapor volume. Such a pressure difference will drive the mixture of vapor bubbles and liquid slugs from the evaporator to condenser. With the continuous movement of vapor bubbles s and liquid plugs towards the condenser, vapor pressure in the condenser increases continuously until it exceeds the evaporator pressure, then the vapor bubbles and liquid plugs will stop moving and subsequently change flow direction, i.e., from the condenser to the evaporator. Different from the conventional heat pipe, the OHP is a kind of heat pipe with instable two-phase flow driven by non-equilibrium pressure, which is due to the temperature gradient between the evaporator and condenser coupled with inherent real-time perturbations. These perturbations may be caused by the local uniform heating and cooling within the evaporator and condenser, uneven void fraction in the tubes due to unsymmetrical liquid-vapor distributions, and presence of approximately triangular or saw-tooth alternating component of pressure of vapor bubbles [17]. The OHP is a self-sustained thermally driven heat pipe.

The OHP can be classified into two types: open oscillating heat pipe (OOHP) [18] and closed loop oscillating heat pipe (CLOHP) [19]. The former is simpler and easier to be investigated theoretically. However, a closed loop oscillating heat pipe

is thermally better than the former [14]. These two types of OHPs are shown in the following Fig.1.1.

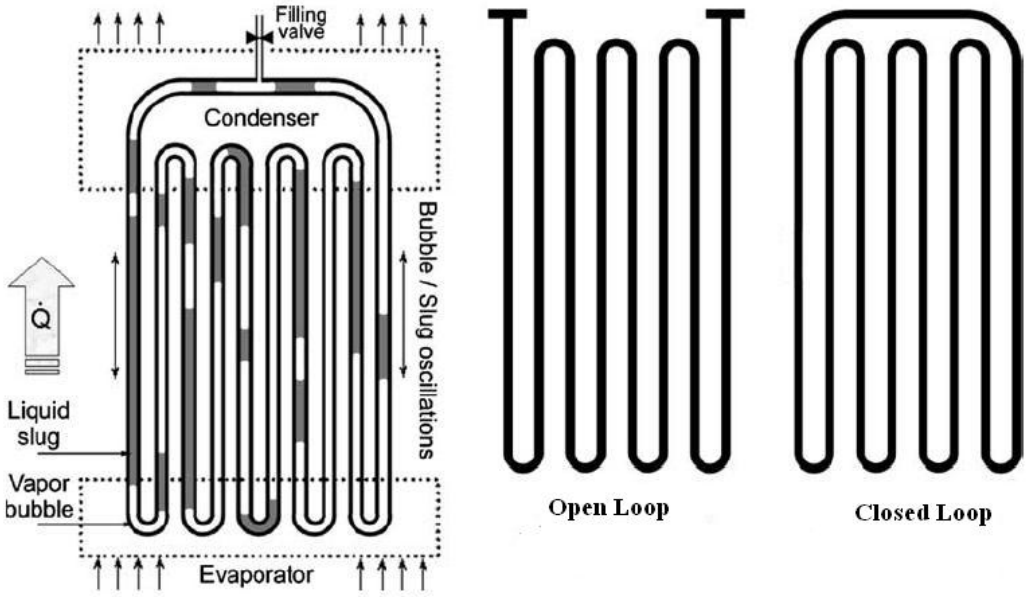

Fig. 1.1 Two types of OHPs [4]

1.2.1 Effect of tube diameter

For a working OHP, liquid slugs and vapor bubbles must co-exist. The motion of the vapor bubble in the liquid is governed by the interaction between buoyancy and forces such as liquid inertia, frictional force and surface tension acting on the bubbles. Previous research revealed that when the non-dimensionless Bond number is approximately equal to 2, the surface tension is the dominating force, and the critical tube diameter could be obtained by:

$$D_{crit} = 2.0\sqrt{\frac{\sigma}{g\left(\rho_l - \rho_v\right)}} \tag{1-1}$$

Consdering the tube material, working fluid, wetting characteristics, hysteresis phenomena [4], it is found that the critical Bond number is about equal to 1.84 [20,

21]. Experimental investigations show that the OHP with a tube diameter satisfying Eq. (1-1) provides a better heat transfer performance [19].

1.2.2 Effect of working fluid

The working fluid selected should have the following properties [22]:

1) *High value of* $(dP/dT)_{sat}$ ensures that a small change in the temperature generates a larger pressure variation inside the generated bubble which aids in the bubble pumping action of the device.
2) *Low viscosity* generates lower shear stress.
3) *Low latent heat* should be desirable because it can help to quickly increase/decreases vapor bubble volume although the sensible heat is the dominant heat transfer mode in an OHP.
4) *High specific heat* is desirable complimenting the low latent heat requirement; although there are no specific studies which explicitly suggest the effect of specific heat of liquid on the heat transfer performance. It should be noticed that when a flow regime changes from slug to annular flow, the sensible-heat-dominated heat transfer might change to the latent-heat-dominated heat transfer as explained earlier. The detailed heat transfer mechanism, however, is not fully understood.
5) *Low surface tension* in conjunction with surface wetting characteristics may create additional pressure drop.

The property effects summarized above are based on the literatures available so far [6, 23].

1.2.3 Effect of filling ratio

The filling ratio is defined as the ratio of working fluid volume present in the channel to the total inside volume of the channels [22]. For the extreme case, when the filling ratio is 0, the heat pipe has no working fluid and it is like a conduction fin, and for the other extreme case, when the filling ratio is 1, the OHP is filled with 100% of liquid. Khanderkar et al. [17] stated that three distinct sub-regions between these two extreme cases. For the sub-region which close to 100% filling ratio, there exist very few bubbles to generate oscillation. Instead, the existence of bubbles hindered the circulation of liquid, which causes the thermal resistance of such mode even higher than that of 100% fill ratio. For another sub-region which close to 0 filling ration, the amount of working fluid in the device is not enough to form slugs. The device acts as a two-phase thermosyphon, but the operational characteristics is not stable [24]. Generally, the filling ratio range for a functional OHP is about 10% to 90%. This range may change with different working fluid, operating parameters and constructional details. And some researchers believed that there exists optimized filling ratio for the best heat transfer performance of OHP. For example, Zhang et al. [6], who conducted an experimental investigation using different working fluid, found that the optimum filling ratio is 70% for all of the tested working fluid, and 60%~80% acceptable range of filling ratio.

1.2.4 Effect of titled angle

The operation orientation is one of the important issues to be considered in the design of OHP. Previous research [4] indicated that there are two factors determining the range of tilted angle of devices, i.e, the gravitational force and t turn number [4]. As mentioned above, the surface tension plays a key role in the formation of vapor bubbles in an OHP. And it is found that when the Bond number is equal or less than the critical value 2.0 or 1.84, the surface tension can help to form the vapor bubble. However, experimental investigations [4] indicated that the shape of liquid slugs and vapor bubbles depends on the inclination angle, which indirectly shows it is not only due to surface tension. It is also clear that in a non-operating, isothermal, partially filled CLOHP, the static pressure distribution traversing across the tube through liquid slugs and vapor bubbles is drastically different in vertical and horizontal orientations [15]. Gravity still affects OHP dynamics even though the boundary conditions satisfy the critical Bond number criterion [25]. Researchers [26,27] experimentally researches [26, 27] also showed that OHP has better performance under micro-gravity or no gravity (horizontal mode).

For the second factor-the turn number, researchers [4] also found that there exists a critical number, beyond which the OHP will not satisfactorily work in the horizontal orientation [4]. If the turn number is smaller than this critical number, the heat transfer performance reaches the highest normally at vertical bottom heating mode,

and then decreases continuously as the device is turned towards horizontal. However, when the turn number is higher than the critical value, although the performance improves with increasing the inclination angle from horizontal orientation, the performance remains nearly comparable from vertical position to about 60 ºC. The critical turn number depends on the working fluid and tube size.

1.3 Theoretical investigation on OHP

1.3.1 Theoretical model of OHP

After the OHP was proposed by Achachi [3] as a new type of cooling device, the theoretical investigation on the heat transfer and fluid flow mechanisms have been conducted. For the liquid-vapor pulsating flow in a capillary tube, one of challenging heat transfer mechanisms is the oscillating motion coupling with phase-change heat transfer which has some random properties. Due to the complexity of the oscillating fluid motion, it's difficult to develop a mathematical model accurately predicting the heat transfer performance in an OHP, and most of current published models have some limitations or are only valid with some presuppositions. Generally the theoretical investigations on the OHP were conducted in two ways: simplified or approximated model by neglecting the random factors; and numerical simulation with all factors included but still based on some ideal assumptions.

For the first case, Miyazaki and Akachi [28] derived the wave equation for

pressure oscillation in an oscillating heat pipe based on self-excited oscillation. Wong et al. [29] presented a theoretical modeling of OHP based on a Lagrangian approach, in which the flow was modeled under adiabatic conditions for the whole OHP, and the liquid thin film between the vapor bubble and wall where the surface tension effect were neglected. Zhang and Faghri [11] presented a simplified model for an oscillating heat pipe with one end open, in which they tried to involve the effect of surface tension and heat transfer through the liquid film between vapor bubble and tube wall. The results showed that for such kind of oscillatingg heat pipe, heat transfer due to sensible heat plays a much more important role than latent heat. In other words, contribution of phase change to the oscillating heat pipe is to supply driving force to the pulsating motion. However this model might be not as over-simplified as the previous investigations. But it was based on a system with one straight pipe and only one vapor plug and liquid slug respectively. It is also noticed that in this model, the evaporator and condenser were distributed in series at the same end, and moreover the length of adiabatic section was set to zero, which is not very common in a typical oscillating heat pipe.

In another paper presented by Zhang et al [12], a dimensionless equation of liquid slug location for a system of two vapor plug and one liquid slug in a U-shaped tube with two ends sealed, can be expressed as

$$X_p = B_0 e^{-16\tau} \cos\left(\sqrt{\omega_0^2 - 16}\tau + \phi_0\right) + \frac{\zeta A \cos(\omega t - \psi)}{\sqrt{\left(\omega_0^2 - \omega^2\right)^2 + 1024\omega^2}} \qquad (1\text{-}2)$$

The results showed that initial displacement of the liquid slug and gravity had no

significant effect on the oscillation motion.

Zuo et al. [30] considered a typical OHP shown in Fig. 1.1 and presented a governing equation as follows:

$$\frac{d^2x}{d\tau^2}+\left(\frac{8\mu_l P\phi_0}{\rho_l DA}\right)\frac{dx}{d\tau}+\frac{2A^2RT_{sat}}{\left(LA\rho_l\phi_0\right)\left[\left(L/2\right)A\rho_l\left(1-\phi_0\right)/\rho_v\right]^2}\cdot\left[\left(L/2\right)A\rho_l\left(1-\phi_0\right)+\frac{Q_e}{h_{fg}}\tau\right]x=0 \tag{1-3}$$

where ϕ_0 is the initial filling ratio of liquid. The equation considers the effect of filling ratio. And in the following part of this paper, a numerical simulation was conducted and verified the optimal filling ratio obtained by Eq. (1-3).

Ma et al. [13] also presented a governing equation for liquid slug in a general heat pipe, in which a function of temperature variation between of the evaporator and condenser was assumed. The equation is as follows:

$$\left(L_l\rho_l+L_v\rho_v\right)A\frac{d^2x}{d\tau^2}+\left[\left(f_l\cdot\mathrm{Re}_l\right)\left(\frac{\mu_l L_l}{2D_h^2}\right)+\left(f_v\cdot\mathrm{Re}_v\right)\left(\frac{\mu_v L_v}{2D_h^2}\right)\right]A\frac{dx}{d\tau}+\frac{A\rho_v RT}{L_v}x=\left(\frac{Ah_{fg}\rho_{v,c}}{T_e}\right)\left(\frac{\Delta T_{\max}-\Delta T_{\min}}{2}\right)\left[1+\cos\left(\omega\tau\right)\right] \tag{1-4}$$

The model considers the effects of tube dimensions, filling ratio, operating temperature, and temperature difference between the evaporator and condenser. Combined with several additional equations determining the heat transfer coefficient for both sensible heat and latent heat, the model can be used to predict the heat ransfer performance in an OHP and results show that sensible heat play a more important role in the heat transfer of heat pipe, which is consistent with the conclusion obtained by

Zhang and Faghri [11].

It is noticed that the models summarized above are based on either simplified cases or neglecting the effect of multi liquid slugs. Shafii et al. [10] conducted a numerical simulation of looped and un-looped OHPs with multi liquid slugs. The results showed that gravity has no significant effect on heat transfer for un-looped OHP with the top heat mode. The total vapor plugs will decrease to the number of bending sections no matter what the initial number is. They also showed that heat transferred by the sensible heat is much larger than latent heat.

1.3.2 Heat transfer in an OHP

As presented in the previous sections, theoretical investigations indicate that heat transfer due to the sensible heat plays a much more important role than latent heat in the OHP [10, 11, and 13]. Some of the experimental investigations [16] also demonstrated that there are two kinds of flow mechanisms in the OHP, i.e., oscillation and circulation. And it was found that the OHP has a better heat transfer performance when the circulation existed. All these models, however, cannot explain this phenomenon very well. It should be noticed that in the models of Zhang et al [11] and Shafii et al [10], the heating and cooling section are adjoining one by one, such that there is no adiabatic section, which is different from the general cases. It is easily imagined that under this kind of situation the liquid slugs would pass through heating and cooling sections alternately very often when oscillation occurs,

and heat transfer is mainly due to convection.

In the model of Ma et al [13], the heat transfer coefficient was divided into two parts by applying the theory of Chen [31]: heat transfer due to the nucleate boiling and heat transfer due to bulk convection. However, it is needed to verify the coefficient is valid for pulsating two-phase flow. In fact pulsating fluid flow and heat transfer occur in many industrial fields. Experimental studies on pulsating turbulent flow were conducted since 1970's. Most of these investigations focus on the single phase flow. Even for the single phase flow, the heat transfer mechanisms of pulsating flow have not been fully understood. Available experimental studies related to heat transfer of pulsating flow show many controversial results. For example, it was reported that frequency had no direct effect on the Nusselt number [32]. Whileno heat transfer enhancement was found in [33, 34], a slight heat transfer reduction was found in [35]. It was also reported that Nusselt number decreases if the frequency is below a certain frequency, and Nusselt number increases if the frequency is above a certain frequency [36]. The heat transfer enhancement occurs only when the oscillating frequency was higher than a certain value [37]. The heat transfer coefficient increases with the pressure oscillation amplitude [38], and high frequency and large oscillation amplitude can enhance heat transfer especially at low Reynolds number [39]. Nusselt number was found to increase with both pulsation amplitude and frequency in a square-sectional duct [40] and so on.

1.3.3 Heat transfer enhancement of OHP

As introduced in the first section, there are many factors affecting the heat transfer performance of OHP, such as setting optimized filling ratio, turn number, gravity, and working fluid. In order to increase the heat transfer performance, a number of investigators employed a number of new approaches. By applying a porous metal wick to the channel wall, an OHP can remove a heat flux of over 200W/cm^2 at a temperature of just 20 K [30]. Holley and Fagrhi [41] presented a numerical simulation of an OHP with capillary wick including the tube diameter effect. In their model, multi liquid slugs were considered, including heat transfer in the wall, wick and working fluid. The results showed that as tube diameter along the channel varies, the heat transport capability in an OHP can be increased and is less sensitive to gravity

1.4 Dissertation objectives

The research objectives of this current investigation are summarizes as follows: 1)to develop a theoretical model of oscillating motion in an OHP which can be used to predict the oscillating motion including the effects of turn number, filling ratio, gravity, heat input, and operating temperature; 2) to develop a heat transfer model predicting the heat transfer performance in an OHP; 3) to develop an thin film evaporation model which considers the fluid momentum effect; 4)to develop a mathematical model predicting minimum meniscus radius occurring in an sintered particle wick; 5) to develop a mathematical model predicting heat transfer occurring

in a sintered wick; and 7) to develop a model predicting the non-condensable gas effect in a charging process.

CHAPTER 2 MATHEMATICAL MODEL OF OSCILLATING MOTION & HEAT TRANSFER IN OHP

2.1 Physical Model

As shown in Fig. 1.1 in previous chapter, a general OHP is considered which can be used for either open loop or close loop the OHP. Based on previous investigation [12-13, 30], the one dimensional assumption of the oscillating motion occurring in an OHP is reasonable. The meandering tube could be taken as a straight one as shown in Fig. 2.1. Sections for heating and cooling distribute alternately. If the OHP works with vertical mode or with any angle other than zero, the direction of gravity would reverse section by section. The vapor bubble and liquid plug appear alternately along the tube. It is noticed that for a closed looped OHP, the number of vapor bubble is the same as that of liquid plug and equal to N, and for an open looped OHP, the number of vapor bubble is $N+1$, and liquid plug N. However, it is also possible for an open looped OHP, that there are $N+1$ liquid plugs and N vapor bubbles, or plugs and bubbles with even number. For these two cases, the extra one or two liquid plugs actually are trapped in the two ends of tubing which are located in the condenser, and are not involved in the system motion, which have very little effect. Hence, it is still reasonable for the number setting aforementioned.

The following assumptions are made for the model:

1) The vapor phase in the OHP is saturated and ideal;

2) The driving force caused by the surface tension is neglected;

3) The mass variation of vapor is neglected during the steady-state process. In other words, the oscillation of vapor mass (or liquid mass) is not significant when the whole system reaches a steady-state;

4) The drag force due to viscosity between the tube wall and vapor phase is neglected;

5) Temperature variations at both the evaporator and condenser are relatively small comparing with the operating temperature (in Kelvin degree).

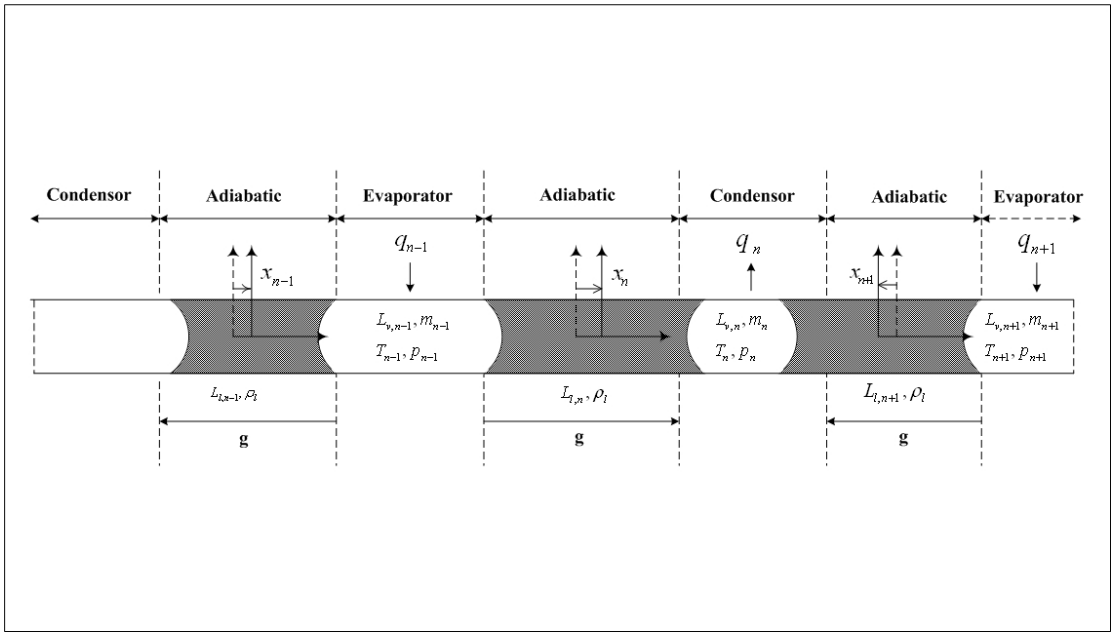

Fig. 2.1 One-dimensional schematic of OHP

Because the vapor phase is saturated, the vapor pressure can be described by the Clapeyon Equation, i.e.,

$$p = p_0 \exp\left(\frac{h_{fg}}{R}\frac{T - T_0}{TT_0}\right) \tag{0-1}$$

where the subscript *0* denotes a reference state Using Taylor series, Eq. (2.1) can be expressed as:

$$p = p_0 + h_{fg}\rho_{v0}\frac{T - T_0}{T} \tag{0-2}$$

where it should be noticed that the higher terms are not considered because higher terms are so small that they can be neglected. Based on the ideal gas assumption, i.e.:

$$\frac{pV}{T} = mR \tag{0-3}$$

Eq. (2-3) can be obtained as

$$Rdm = pd\left(\frac{V}{T}\right) + \frac{V}{T}dp \tag{0-4}$$

Considering Eq. (2-2), two terms on the right side of Eq. (2-4) can be rewritten as:

$$pd\left(\frac{V}{T}\right) = \left(p_0 + h_{fg}\rho_{v0}\frac{T - T_0}{T}\right)d\left(\frac{V}{T}\right) \tag{0-5}$$

$$\frac{V}{T}dp = \frac{V}{T}d\left(p - p_0\right) = -T_o h_{fg}\rho_{v0}\frac{V}{T}d\left(\frac{1}{T}\right) \tag{0-6}$$

respectively. Substituting Eqs. (2-5) and (2-6) into Eq. (2-4), and dividing Eq. (2-4) by $T_0 h_{fg}\rho_{v0}$, it can be found as:

$$\frac{R}{T_o h_{fg}\rho_{v0}}dm = \left(\frac{1}{T_0} + \frac{R}{h_{fg}}\right)d\left(\frac{V}{T}\right) - d\left(\frac{V}{T^2}\right) \tag{0-7}$$

Basing on the steady state assumption, $d\left(V/T\right)$ and $d\left(V/T^2\right)$ could be simplified as:

$$d\left(\frac{V}{T}\right) = \frac{1}{T_0}dV - \frac{V_0}{T_0^2}dT \tag{0-8}$$

$$d\left(\frac{V}{T^2}\right)=\frac{1}{T_0^2}dV-\frac{2V_0}{T_0^3}dT \tag{0-9}$$

respectively. Equation (2-7) can be rewritten as:

$$\frac{R}{h_{fg}T_0}dV+\frac{V_0}{T_0^2}\left(\frac{1}{T_0}-\frac{R}{h_{fg}}\right)dT=\frac{R}{h_{fg}T_0\rho_{v0}}dm \tag{0-10}$$

For such a vapor bubble, the energy balance gives:

$$\delta Q=dH+\delta W=d\left(mc_pT\right)+\delta W=m_0c_pdT+c_pT_0dm+\delta W \tag{0-11}$$

where c_p is the heat capacity, which is assumed to be constant.

Considering Eq. (2-11), Eq. (2-10) can be found as:

$$\frac{R}{h_{fg}}dV+\frac{V_0}{T_0^2}dT=\frac{R\left(qt-\delta W\right)}{h_{fg}\rho_{v0}c_pT_0} \tag{0-12}$$

it should be noticed that $\delta Q=qt$ .Substituting $dV=V-V_0$ and $dT=T-T_0$ into Eq. (2-12), the relation between vapor volume and temperature could be expressed as:

$$\frac{R}{h_{fg}}V+\frac{V_0}{T_0^2}T=\left(\frac{R}{h_{fg}}+\frac{1}{T_0}\right)V_0+\frac{R\left(qt-\delta W\right)}{h_{fg}\rho_{v0}c_pT_0} \tag{0-13}$$

For the nth vapor bubble shown in Fig. 2.1., the original length is $L_{n,0}$, and the volume can be calculated by $V=\left(L_{n,0}+x_{n+1}-x_n\right)A$. Then Eq. (2-13) can be rewritten as:

$$\frac{R}{h_{fg}}\left(1+\frac{x_{n+1}-x_n}{L_{n,0}}\right)+\frac{T_n}{T_0^2}=\frac{R}{h_{fg}}+\frac{1}{T_0}+\frac{R\left(q_nt-\delta W_{n\to n}\right)}{h_{fg}c_pA\rho_{v0}L_{n,0}T_0} \tag{0-14}$$

The momentum equation for the nth liquid plug can be found as:

$$\rho_lAL_{l,n}\frac{d^2x_n}{dt^2}+\left(f\bullet\mathrm{Re}_l\right)\frac{\mu_lL_{l,n}A}{2D_h^2}\frac{dx_n}{dt}=A\left(p_{n-1}-p_n\right) \tag{0-15}$$

Basing on Eq. (2-2), it is known that:

$$p_{n-1}-p_n=\frac{T_0\left(T_{n-1}-T_n\right)}{T_nT_{n-1}}h_{fg}\rho_{v0} \tag{0-16}$$

where T_n and T_{n-1} can be expressed as: $T_n = T_0 + \Delta T_n$ and $T_{n-1} = T_0 + \Delta T_{n-1}$. It is noticed that the deviation of temperature is very small comparing with temperature itself. Hence Eq. (2-16) could be approximated as:

$$p_{n-1} - p_n \approx \frac{\left(T_{n-1} - T_n\right)}{T_0} h_{fg} \rho_{v0} \tag{0-17}$$

For the n[th] liquid plug (subscripts of its neighboring vapor bubbles are *n-1* and *n* respectively), it is noticed that the work done by the vapor bubble on the liquid plug, which is determined by the slug motion, has different sign for different sides of the liquid plug. Basing on Eq. (2-14), it can be found that:

$$\begin{aligned} \frac{T_{n-1} - T_n}{T_0^2} = & \frac{R}{h_{fg} c_p \rho_{v0} A T_0} \left(\frac{q_{n-1} t + \delta W_{n-1 \to n}}{L_{n-1,0}} - \frac{q_n t - \delta W_{n \to n}}{L_{n,0}} \right) + \\ & \frac{R}{h_{fg}} \left(\frac{x_n - x_{n-1}}{L_{n-1,0}} - \frac{x_{n+1} - x_n}{L_{n,0}} \right) \end{aligned} \tag{0-18}$$

Substituting this equation into Eq. (2-17) and then into (2-15), it yields:

$$\begin{aligned} & \rho_l L_{l,n} \frac{d^2 x_n}{dt^2} + \left(f \bullet \mathrm{Re}_l \right) \frac{\mu_l L_{l,n}}{2 D_h^2} \frac{dx_n}{dt} - R \rho_{v0} T_0 \left(\frac{1}{L_{n-1,0}} + \frac{1}{L_{n,0}} \right) x_n + \\ & R \rho_{v0} T_0 \left(\frac{x_{n-1}}{L_{n-1,0}} + \frac{x_n}{L_{n,0}} \right) = \frac{R}{c_p A} \left[\left(\frac{q_{n-1}}{L_{n-1,0}} - \frac{q_n}{L_{n,0}} \right) + \left(\frac{\delta W_{n-1 \to n}}{L_{n-1,0}} + \frac{\delta W_{n \to n}}{L_{n,0}} \right) \right] \end{aligned} \tag{0-19}$$

Equation (2-19) can be expressed in matrix as:

$$\mathbf{M}\ddot{\mathbf{x}} + \mathbf{C}\dot{\mathbf{x}} + \mathbf{S}\mathbf{x} = \mathbf{Q}\left(t\right) + \mathbf{W} \tag{0-20}$$

where:

$$\mathbf{M} = \rho_l \begin{pmatrix} L_{l,1} & 0 & \cdots & 0 \\ 0 & L_{l,2} & \cdots & \vdots \\ \vdots & \vdots & \ddots & \vdots \\ 0 & 0 & \cdots & L_{l,N} \end{pmatrix} \tag{0-21}$$

$$\mathbf{C}=\frac{\left(f\bullet \mathrm{Re}_l\right)\mu_l}{2D_h^2}\begin{pmatrix} L_{l,1} & 0 & \cdots & 0 \\ 0 & L_{l,2} & \cdots & \vdots \\ \vdots & \vdots & \ddots & \vdots \\ 0 & 0 & \cdots & L_{l,N} \end{pmatrix} \tag{0-22}$$

$$\mathbf{S}=R\rho_{v0}T_0\begin{pmatrix} -\frac{1}{L_{1,0}}-\frac{1}{L_{N,0}} & \frac{1}{L_{1,0}} & 0 & \cdots & 0 & \frac{1}{L_{N,0}} \\ \frac{1}{L_{1,0}} & -\frac{1}{L_{2,0}}-\frac{1}{L_{1,0}} & \frac{1}{L_{2,0}} & \ddots & \ddots & 0 \\ 0 & \ddots & \ddots & \ddots & \ddots & \vdots \\ \vdots & 0 & \frac{1}{L_{n-1,0}} & -\frac{1}{L_{n,0}}-\frac{1}{L_{n-1,0}} & \frac{1}{L_{n,0}} & \vdots \\ 0 & \vdots & \ddots & \ddots & \ddots & 0 \\ \frac{1}{L_{N,0}} & 0 & \cdots & 0 & \frac{1}{L_{N-1,0}} & -\frac{1}{L_{N,0}}-\frac{1}{L_{N-1,0}} \end{pmatrix} \tag{0-23}$$

$$\mathbf{Q}\left(t\right)=\frac{Rt}{c_pA}\begin{pmatrix} -\frac{1}{L_{1,0}} & 0 & \cdots & \cdots & \cdots & 0 \\ \frac{1}{L_{1,0}} & -\frac{1}{L_{2,0}} & \ddots & \ddots & \ddots & \vdots \\ 0 & \ddots & \ddots & \ddots & \ddots & \vdots \\ \vdots & \ddots & \frac{1}{L_{n-1,0}} & -\frac{1}{L_{n,0}} & \ddots & \vdots \\ \vdots & \ddots & \ddots & \ddots & \ddots & 0 \\ 0 & \cdots & \cdots & 0 & -\frac{1}{L_{N-1,0}} & -\frac{1}{L_{N,0}} \end{pmatrix}\begin{pmatrix} q_1 \\ \vdots \\ \vdots \\ q_n \\ \vdots \\ q_N \end{pmatrix} \tag{0-24}$$

$$\mathbf{W}=\frac{R}{c_pA}\begin{pmatrix} \frac{\delta W_{N\to 1}}{L_{N,0}}+\frac{\delta W_{1\to 1}}{L_{1,0}} \\ \frac{\delta W_{1\to 2}}{L_{1,0}}+\frac{\delta W_{2\to 2}}{L_{2,0}} \\ \vdots \\ \frac{\delta W_{n-1\to n}}{L_{n-1,0}}+\frac{\delta W_{n\to n}}{L_{n,0}} \\ \vdots \\ \frac{\delta W_{N-1\to N}}{L_{N-1,0}}+\frac{\delta W_{N\to N}}{L_{N,0}} \end{pmatrix} \tag{0-25}$$

It is noticed that equations discussed above are valid only for the case of closed looped OHP in horizontal mode. For other cases, using the approaches presented

above, the equations and matrix can be readily obtained.

For an open looped OHP in horizontal mode, the matrix S will be different which can be found as:

$$\mathbf{S} = R\rho_{v0}T_0 \begin{pmatrix} -\frac{1}{L_{1,0}} - \frac{1}{L_{0,0}} & \frac{1}{L_{1,0}} & 0 & \cdots & 0 & 0 \\ \frac{1}{L_{1,0}} & -\frac{1}{L_{2,0}} - \frac{1}{L_{1,0}} & \frac{1}{L_{2,0}} & \ddots & \ddots & 0 \\ 0 & \ddots & \ddots & \ddots & \ddots & \vdots \\ \vdots & 0 & \frac{1}{L_{n-1,0}} & -\frac{1}{L_{n,0}} - \frac{1}{L_{n-1,0}} & \frac{1}{L_{n,0}} & \vdots \\ 0 & \vdots & \ddots & \ddots & \ddots & 0 \\ 0 & 0 & \cdots & 0 & \frac{1}{L_{N-1,0}} & -\frac{1}{L_{N,0}} - \frac{1}{L_{N-1,0}} \end{pmatrix} \quad (0\text{-}26)$$

If the gravitational force is considered, one extra term for both closed and open looped OHPs will be added as follows:

$$\mathbf{M}\ddot{\mathbf{x}} + \mathbf{C}\dot{\mathbf{x}} + \mathbf{S}\mathbf{x} = \mathbf{Q}(t) + \mathbf{W} + \mathbf{G}(t) \quad (0\text{-}27)$$

If all of the liquid plugs keep oscillating in their initial sections, **G** is not a function of time and can be expressed as:

$$\mathbf{G} = \rho_l g \begin{pmatrix} (-1)^{N_{\sec}(1)} L_{l,1} \\ \vdots \\ (-1)^{N_{\sec}(n)} L_{l,n} \\ \vdots \\ (-1)^{N_{\sec}(N)} L_{l,N} \end{pmatrix} \quad (0\text{-}28)$$

where $N_{sec}(n)$ denotes which section of the tube the n^{th} liquid plug is at.

If the liquid plug passes through different sections during oscillating motion, **G** will be a function of time also:

$$\mathbf{G}(t) = \rho_l g \begin{pmatrix} \operatorname{sgn}(1,t) L_{l,1} \\ \vdots \\ \operatorname{sgn}(n,t) L_{l,n} \\ \vdots \\ \operatorname{sgn}(N,t) L_{l,N} \end{pmatrix} \tag{0-29}$$

where *sgn(n,t)* denotes the sign of the nth liquid plug at t.

From the system stiffness, it is noticed that for both open looped and close looped OHPs, the vapor bubbles in the system function similar to linear springs. The whole system could be illustrated in the way shown in Fig. 2.2. It should be noticed that the energy received or released by vapor bubbles is not only from/to kinetic energy, but also from the heating or cooling, which is different from natural springs.

Fig. 2.2 A spring system of OHP

2.2 Model Analysis

By solving the equations shown in the previous section, the oscillation motion in the OHP could be determined. However, there are still some problems existed such as: how to determine the number N which is generally uncertain for an operational

OHP; and how to determine heat transfer into the vapor bubble. It is noticed that the thermal energy received from and released to the surrounding is not only through vapor bubbles, but also through the convection heat transfer of liquid plugs, which has also been discussed in the previous literatures. These problems would be discussed in the following sections including assumptions.

2.2.1 System natural frequencies

The natural frequency of the whole system could be obtained through the mass and stiffness matrix by solving the characteristic equation:

$$\left|\omega^2\mathbf{M}-\mathbf{S}\right|=0 \tag{2-30}$$

Where mass M and stiffness S is expressed as:

$$\mathbf{M}=\rho_l L_l\begin{pmatrix}\alpha_1 & 0 & \cdots & 0\\ 0 & \alpha_2 & \cdots & \vdots\\ \vdots & \vdots & \ddots & \vdots\\ 0 & 0 & \cdots & \alpha_N\end{pmatrix} \tag{2-31}$$

$$\mathbf{S}=-\frac{R\rho_{v0}T_0}{L_v}\begin{pmatrix}\frac{1}{\beta_1}+\frac{1}{\beta_N} & -\frac{1}{\beta_1} & 0 & \cdots & -\frac{1}{\beta_N}\\ -\frac{1}{\beta_1} & \frac{1}{\beta_2}+\frac{1}{\beta_1} & -\frac{1}{\beta_2} & 0 & 0\\ 0 & \ddots & \ddots & \ddots & \vdots\\ \vdots & \vdots & -\frac{1}{\beta_{n-1}} & \frac{1}{\beta_n}+\frac{1}{\beta_{n-1}} & -\frac{1}{\beta_n}\\ -\frac{1}{\beta_N} & 0 & \cdots & -\frac{1}{\beta_{N-1}} & \frac{1}{\beta_N}+\frac{1}{\beta_{N-1}}\end{pmatrix} \tag{2-32}$$

respectively. α, β in Eqs. (2.31) and (2.32)denote the length ratio of each individual slug or plug to the total length of liquid or vapor respectively, i.e. $\alpha_n = L_{l,n}/L_l$, $\beta_n = L_n/L_v$. Then a frequency can be found as:

$$\omega_0 = \sqrt{\frac{R\rho_{v0}T_0}{\rho_l L_l L_v}} \tag{2-33}$$

Where it should be noticed that Eq. (2-33) cannot be used to replace the natural frequency. The real natural frequency should be higher or smaller than this value depending on the mass and stiffness matrix. For the system with one freedom, it is the natural frequency.

Wth this frequency, Eq. (2-30) becomes:

$$\det\left|\left(\frac{\omega}{\omega_0}\right)^2\begin{pmatrix}\alpha_1 & 0 & \cdots & 0\\ 0 & \alpha_2 & \cdots & \vdots\\ \vdots & \vdots & \ddots & \vdots\\ 0 & 0 & \cdots & \alpha_N\end{pmatrix}+\begin{pmatrix}\frac{1}{\beta_1}+\frac{1}{\beta_N} & -\frac{1}{\beta_1} & 0 & \cdots & -\frac{1}{\beta_N}\\ -\frac{1}{\beta_1} & \frac{1}{\beta_2}+\frac{1}{\beta_1} & -\frac{1}{\beta_2} & 0 & 0\\ 0 & \ddots & \ddots & \ddots & \vdots\\ \vdots & \vdots & -\frac{1}{\beta_{n-1}} & \frac{1}{\beta_n}+\frac{1}{\beta_{n-1}} & -\frac{1}{\beta_n}\\ -\frac{1}{\beta_N} & 0 & \cdots & -\frac{1}{\beta_{N-1}} & \frac{1}{\beta_N}+\frac{1}{\beta_{N-1}}\end{pmatrix}\right| = 0 \tag{2-34}$$

which shows that the distribution of liquid plug and vapor bubble in the OHP is one of the dominating factor to the system natural frequency.

Considering $L_{tot}=L_l+L_v$ and filling ratio $\varphi = \frac{V_l}{V_{tot}}$, Eq. (2-33) becomes:

$$\omega_0 = \frac{1}{L_{tot}}\sqrt{\frac{R\rho_{v0}T_0}{\rho_l\phi(1-\phi)}} \tag{2-35}$$

As shown in Eq. (2-35), the liquid filling ratio is also a important parameter determining the frequency.

Consider one simple case, N=4, which has 4 freedom degrees. The equation for

the natural frequency can be found as:

$$\left\{\left[\alpha_3\left(\frac{\omega}{\omega_0}\right)^2+\frac{1}{\beta_2}+\frac{1}{\beta_3}\right]\left[-\frac{1}{\beta_1^2}+\left(\alpha_2\left(\frac{\omega}{\omega_0}\right)^2+\frac{1}{\beta_1}+\frac{1}{\beta_2}\right)\right]\right\}$$
$$\left\{\left[\alpha_1\left(\frac{\omega}{\omega_0}\right)^2+\frac{1}{\beta_1}+\frac{1}{\beta_4}\right]-\left[\frac{\alpha_1}{\beta_2^2}\left(\frac{\omega}{\omega_0}\right)^2+\frac{1}{\beta_1\beta_2^2}+\frac{1}{\beta_4\beta_2^2}\right]\right\}$$
$$\left[\alpha_4\left(\frac{\omega}{\omega_0}\right)^2+\frac{1}{\beta_3}+\frac{1}{\beta_4}\right]-\frac{1}{\beta_3^2}\left[\alpha_2\left(\frac{\omega}{\omega_0}\right)^2+\frac{1}{\beta_1}+\frac{1}{\beta_2}\right]\left[\alpha_1\left(\frac{\omega}{\omega_0}\right)^2+\frac{1}{\beta_1}+\frac{1}{\beta_4}\right] \quad (2\text{-}36)$$
$$-\frac{1}{\beta_4^2}\left[\alpha_2\left(\frac{\omega}{\omega_0}\right)^2+\frac{1}{\beta_1}+\frac{1}{\beta_2}\right]\left[\alpha_3\left(\frac{\omega}{\omega_0}\right)^2+\frac{1}{\beta_2}+\frac{1}{\beta_3}\right]+$$
$$\frac{1}{\beta_1^2\beta_3^2}+\frac{1}{\beta_2^2\beta_4^2}-\frac{2}{\beta_1\beta_2\beta_3\beta_4}=0$$

The roots were listed in Table 2.1. It indicates that the system natural frequencies varied with different distribution of liquid plugs and vapor bubbles. In the real situation, the oscillating motion of the liquid plugs and vapor bubbles may shift from one mode to anther. This indirectly shows that the oscillating motion in the OHP may not be smooth if the system has the bubble generations or collapses. Previous experimental results show that the system can reach a stable condition, but the oscillating motion in terms of frequency and aptitude is not stable. In other words, although the system can reach a stable oscillating motion in terms of a stable average frequency and aptitude, the transient frequency and aptitude is not constant, which depending on the bubble generation and collapse.

Table 2.1 Natural frequency for *N=4*

Case No.	α_1	α_2	α_3	α_4	β_1	β_2	β_3	β_4	$(\omega/\omega_0)^2$
1	0.25	0.25	0.25	0.25	0.25	0.25	0.25	0.25	0,32,64
2	0.3	0.2	0.3	0.2	0.25	0.25	0.25	0.25	0,26.7,40,66.7
3	0.3	0.2	0.2	0.3	0.25	0.25	0.25	0.25	0,30.85,33.3,69.15
4	0.25	0.25	0.25	0.25	0.4	0.1	0.4	0.1	$2.9\text{x}10^{-15}$,20,80,100
5	0.25	0.25	0.25	0.25	0.4	0.1	0.1	0.4	0,25.76,50,124.24
6	0.3	0.2	0.3	0.2	0.3	0.2	0.3	0.2	$1.6\text{x}10^{-15}$,25,44.4,69.44

2.2.2 Average liquid plug velocity in CLOHP

As reported by literatures [14-16], the bulk circulation was observed in the experiments of CLOHP. It is noticed that if getting the sum of Eq. (2-19) for all of the liquid plugs, the terms related to the locomotion *x* and heat flux *q* are canceled out, and finally it becomes:

$$\begin{aligned}&\rho_l L_l \frac{d^2}{dt^2}\left(\sum \alpha_n x_n\right)+\left(f\bullet \mathrm{Re}_l\right)\frac{\mu_l L_l}{2D_h^2}\frac{d}{dt}\left(\sum \alpha_n x_n\right)\\&=\frac{R}{c_p A}\sum\left(\frac{\delta W_{n\to n}+\delta W_{n\to n+1}}{L_{n,0}}\right)\end{aligned} \tag{2-37}$$

where $\sum \alpha_n x_n$ is defined as the center of mass during locomotion, and it should be noticed that $\left(\delta W_{n\to n}+\delta W_{n\to n+1}\right)$ is actually the net work done by the n^{th} vapor bubble to the liquid plugs. If $X=\sum \alpha_n x_n$, Eq. (2-37) becomes:

$$\rho_l L_l \frac{d^2 X}{dt^2} + \left(f \bullet \mathrm{Re}_l \right) \frac{\mu_l L_l}{2 D_h^2} \frac{dX}{dt} = \frac{R}{c_p A} \sum \left(\frac{\delta W_{n,net}}{L_{n,0}} \right) \tag{2-38}$$

However, $\sum \alpha_n x_n$ does not present the center of mass during locomotion in a general sense, because the meandering tube is straightened in the model. It is much better to only use this definition for the average velocity of liquid plugs along the meandering tube. Equation (2-38) indicates that the motion of the liquid plugs in the CLOHP is driven by the expansion and contraction of vapor bubbles. For the n^{th} vapor bubble, the net work from the bubble can be expressed as:

$$\delta W_{n,net} = d\left(pV \right)_n = Rd\left(mT \right)_n = R\left(T_0 dm + m_0 dT \right)_n \tag{2-39}$$

$$\frac{\delta W_{n,net}}{AL_{n,0}} = R \frac{\left(T_0 dm + m_0 dT \right)_n}{V_{n,0}} = R\left(T_0 d\rho_v + \rho_{v0} dT \right)_n \tag{2-40}$$

For a steady-state operation, the vapor generation in the evaporating section is equal to the vapor condensing rate in the condensing section, the total vapor mass in the whole system is constant, i.e., the net change of the total vapor mass in the system is zero. Hence, $\Sigma T_0 d\rho_v$ can be taken as zero. It is clear from the physical model that the energy of the oscillation in OHP comes from the expansion and contraction of vapor plugs in evaporator and condenser respectively. It can be easily found out that the net work of vapor plugs done in adiabatic section could be neglected. The vapor temperature in the evaporating and condensing sections can be assumed to be uniform, respectively. If taking the reference temperature as the surrounding temperature, which is close to the one of condenser, $\sum dT = N_e \left(T_e - T_0 \right) + N_c \left(T_c - T_0 \right) \approx N_e \left(T_e - T_c \right)$. N_e and N_c denote the bubble

number in the evaporator and condenser, respectively. Then Eq. (2-38) can become:

$$\rho_l L_l \frac{d^2 X}{dt^2} + \left(f \bullet \mathrm{Re}_l\right) \frac{\mu_l L_l}{2D_h^2} \frac{dX}{dt} = \frac{R^2 \rho_{v0}}{c_p} N_e \left(T_e - T_c\right) \tag{2-41}$$

From Eq. (2-41), it can be found that the circulating motion in the CLOHP is due to the temperature drop between the evaporator and condenser. A reasonable approximation of N_e is the number of meandering turns, N_{turn} because most of the bubbles would be produced in the evaporator. And one of numerical analysis, [7], also mentioned that when CLOHP comes to steady state, there would be one vapor bubble for each section, no matter what the initial number was. However, the effect of number of bubbles would be still discussed in the later section.

Chen's model [11] was used to determine the convective evaporation in the evaporator section, in which the total heat transfer coefficient, *h*, can be expressed as

$$h = h_{mic} + h_{mac} \tag{2-42}$$

where h_{mic} is due to the nucleate boiling heat transfer, and h_{mac} due to the bulk convection. The microscopic nucleate boiling portion of the heat transfer coefficient could be found by

$$h_{mic} = 0.00122 \left[\frac{k_l^{0.79} c_{pl}^{0.45} \rho_l^{0.49}}{\sigma^{0.5} \mu_l^{0.29} h_{lv}^{0.24} \rho_v^{0.24}} \right] \left[T_w - T_{sat}(P_l)\right]^{0.24} \left[P_{sat}(T_w) - P_l\right]^{0.75} S \tag{2-43}$$

where S is a suppression factor and a function of the two-phase Reynolds number, i.e.,

$$S = (1 + 2.56 \times 10^{-6} \, \mathrm{Re}_{tp}^{1.17})^{-1} \tag{2-44}$$

The two-phase Reynolds number in Eq. (2-44) can be determined by

$$\mathrm{Re}_{tp} = \mathrm{Re}_l [F(X_{tt})]^{1.25} \tag{2-45}$$

where the liquid Reynolds number and the Martinelli parameter, X_{tt}, are defined by

$$\mathrm{Re}_l = \frac{G(1-x)D_i}{\mu_l} \tag{2-46}$$

$$X_{tt} = \left(\frac{1-x}{x}\right)^{0.9}\left(\frac{\rho_v}{\rho_l}\right)^{0.5}\left(\frac{\mu_l}{\mu_v}\right)^{0.1} \tag{2-47}$$

respectively. The function $F(X_{tt})$ shown in Eq. (2-45) depends on the Martinelli parameter, i.e.,

$$F(X_{tt}) = 1 \quad \text{for} \quad X_{tt}^{-1} \le 0.1 \tag{2-48}$$

$$F(X_{tt}) = 2.35(0.213 + \frac{1}{X_{tt}})^{0.736} \quad \text{for} \quad X_{tt}^{-1} > 0.1 \tag{2-49}$$

Utilizing the Martinelli parameter for a two-phase flow, the heat transfer coefficient due to the forced convection caused by oscillating motions can be readily determined by

$$h_{mac} = F\left(X_{tt}\right)h_l \tag{2-50}$$

where h_l is the liquid-phase heat transfer coefficient defined as

$$h_l = 0.023\left(\frac{k_l}{D_i}\right)\mathrm{Re}_l^{0.8}\,\mathrm{Pr}_l^{0.4} \tag{2-51}$$

An empirical model developed by Shar [12] is used to determine the convective condensation in the condenser, in which the heat transfer coefficient is defined as

$$\frac{h}{h_{lo}} = (1-\phi)^{0.8} + \frac{3.8\phi^{0.76}(1-\phi)^{0.04}}{(P/P_{cr})^{0.38}} \tag{2-52}$$

where *P* and *Pcr* are the absolute local pressure and critical pressures, respectively. And

$$h_{lo} = 0.023\left(\frac{k_l}{D}\right)\left(\frac{GD}{\mu_l}\right)^{0.8} \mathrm{Pr}_l^{0.4} \qquad (2\text{-}53)$$

From (2-41) to (2-53), it can be found that there are four variables the evaporator temperature, T_e, condenser temperature, T_c, wall temperature in the evaporator, T_w,, and average velocity of liquid plugs and vapor bubbles in the CLOHP for a constant heat flux adding on the evaporator, u,. However, Eqs. (2-41) to (2-53) describe only three relations among these variables. An additional equation or relation is needed for a unique solution. Examining relations among those variables, such a relation should come from the evaporator, T_e and T_w can be used to determine the latent heat transferred through the evaporator, which can be found out through investigating every single vapor bubble existing in the evaporating section at a given time. However, numerical investigations [6-8] have shown that heat transferred through sensible heat is much larger than that through latent heat. For example, Miyazaki [7] state that about 95% of the total heat is transferred by the sensible heat and Akdag et. al [8] predict over 90%. The equations from (2-41) to (2-53) can be used to find the relation between the percentage of sensible heat over total heat and the evaporator temperature, i.e. given evaporator temperature, achieve average velocity from Eq. (2-41), then basing on the velocity and other equations obtain the sensible heat percentage.

In order to verify the model, the experimental results obtained by Brian et al [62] were used for a comparison. Figure 2.3 illustrates the configuration of the CLOHP. The working fluid is water and the filling ratio is 50%. The experiments were

conducted at an operating temperature of 20 C and 60 C, respectively.

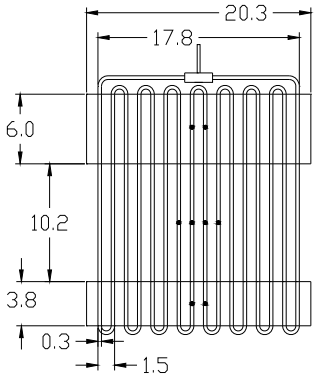

Fig. 2.3 Schematic of 8-turn close-loop oscillating heat pipe

Figure 2.4 shows the evaporator temperature effect on heat transfer occurring in the evaporator at an operating temperature of 60°C. As the evaporator temperature increases, liquid plugs and vapor bubbles in the OHP accelerate, which enhances the convection heat transfer and consequently more heat is transferred through the sensible heat. As shown in Figure 2.4, the power input directly affects the percentage of sensible heat depending on the operating temperature. When the operating temperature is relatively higher, the percentage of the sensible heat decreases as the power input increases. When the operating temperature is relatively lower, the percentage of the sensible heat increases as the power input increases. The reason for this is that the random oscillation of liquid plugs is definitely amplified by a higher temperature, and the average velocity of liquid plugs becomes smaller at a lower operating temperature. . Figure 2.5 illustrates the evaporator temperature effect

on heat transfer occurring in the evaporator at an operating temperature 20°C. It shows a peak value of sensible heat percentage, and the scale of this percentage is much lower than that presented in Fig. 2.4. Obviously, the operating temperature plays a key role in it. And the results of Fig. 2.5 can also prove the conclusion of the existing upper limit for sensible heat at an operating temperature 60°C.

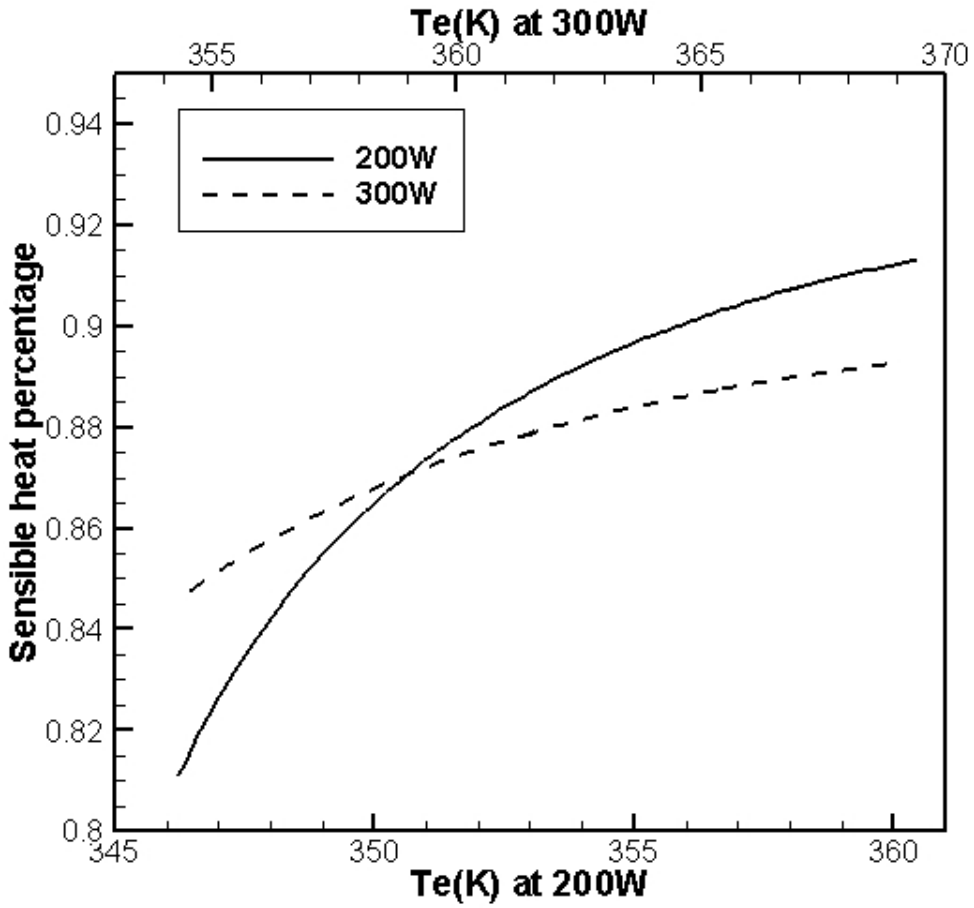

Fig. 2.4 Sensible heat percentage vs. T_e at T_{op}=60°C

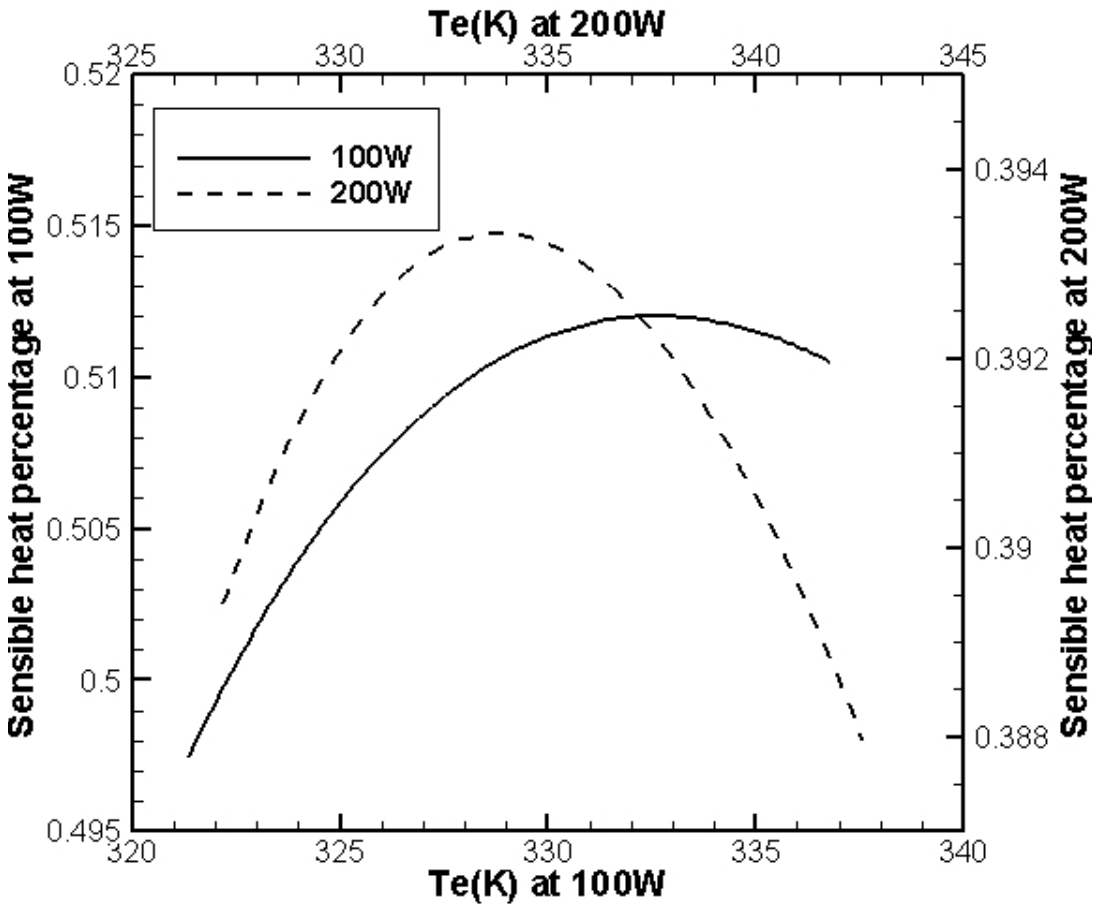

Fig. 2.5 Sensible heat percentage vs. T_e at T_{op}=20°C

As shown on Figures 2.4 and 2.5. The percentage of the sensible heat is basically less than 90%, which is different from the previous prediction [7,8]. It is noticed that in Eq.(2.41), if given the temperature of evaporator and condenser, the right hand term becomes constant, the solution of averaged velocity could be achieved as $\dot{X} = e^{-C_1 t} + C_2$, where C_1 and C_2 are two positive constants, and signal of C_2 is actually determined by right hand side of Eq. (2.41). This means average velocity of liquid slugs will have a fixed direction even the evaporator and condenser's temperature is not constant, which means circulation occurs in OHP. Given Te=75°C, and Tc≈Top=60°C, the average velocity will approaches 1.22m/s. And

given Te=55°C, and Tc≈Top=20°C, the average velocity will approaches 0.18m/s. It could be found that the circulation is much stronger with higher operating temperature, and it is reasonable to see that the sensible heat take a big part under this situation. Actually, different from those analyses in previous investigations, the equations here used are based on the average characteristics, and only capture the properties of heat transfer when circulation occurred obviously. When oscillation is a dominant phenomenon in CLOHP, the average velocity, which is around zero, can not be used to measure the convection heat transfer anymore. But it could be still informed by the trend presented by this model: when temperature or input heat becomes smaller, the average velocity decreased, but the sensible heat percentage increases.

One issue is how to determine the sensible heat percentage in the current model. The thought here is that the CLOHP system prefers stronger convection: more heat transferred into vapor bubbles would induce stronger liquid plug oscillation in the evaporator, and the convection heat transfer would continuously increase until reach to the upper limit. Many factors would affect the percentage upper limit of sensible heat, and as shown in previous discussion, operating temperature and input power are two important parameters. However, a lower percentage might be more reasonable due to the average velocity in the evaporator should be larger than the overall average velocity. And when the system comes to a steady state, the acceleration term in Eq. (2-41) would be eliminated and the equations becomes:

$$\left(f \cdot \mathrm{Re}_l\right)\frac{\mu_l L_l}{2D_h^2}\frac{dX}{dt} = \frac{R^2\rho_{v0}}{c_p}N_e\left(T_e - T_c\right) \tag{2-54}$$

Figure 2.6 shows the temperature drop from evaporator wall and condenser wall for operating temperature is 60°C, and compare between the prediction by model and the experimental results. In the calculation, the percentage was set to a constant equal to 0.87. However this constant is artificial, which is just picked in the range of ±5% of 90%. The predictions in this rage would match partial of the experimental data very well and this selection range is OK just because the working conditions has determined it. For example given constant percentage 0.87 as shown Fig. 2.6, it is noticed that the fixed sensible heat percentage is a little small for lower heat input but a little large for higher heat input. And the prediction trend is not very well; because for very high heat input, the actual sensible heat percentage is much lower than 0.87. This method is not accurate and flexible in the real application. It could be solved in real applications by figuring out the percentage range for each input power, then calculate the temperature difference, as shown in Fig. 2.7, in which the peak value of sensible heat percentage was first determined, and 98% of the peak values was set to the actual value considering liquid plug velocity is a little higher than the average velocity.

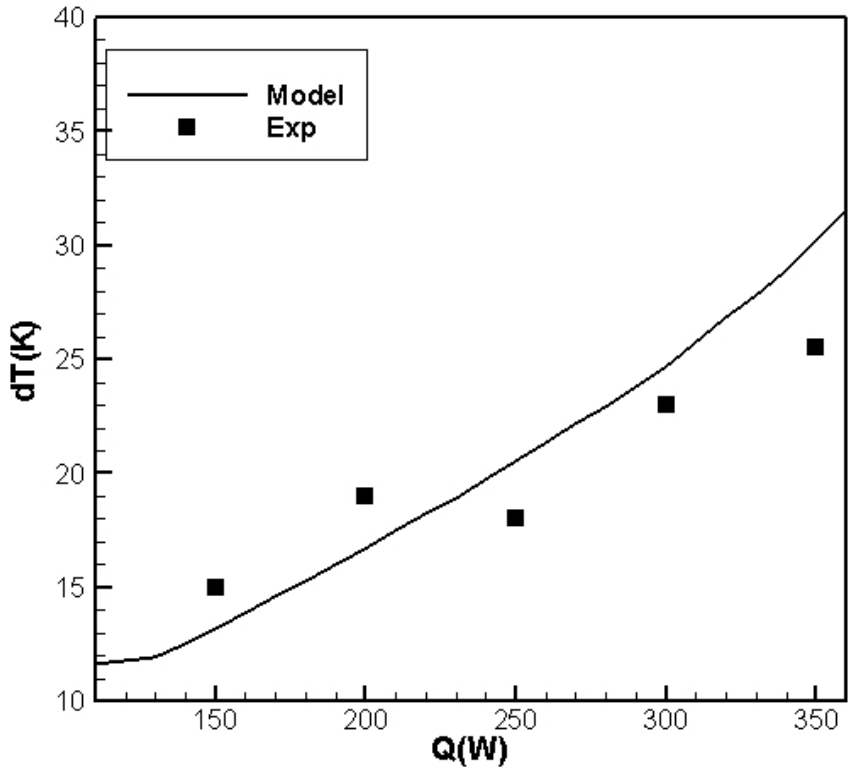

Fig. 2.6 Temperature drop vs. Heat input at T_{op}=60°C

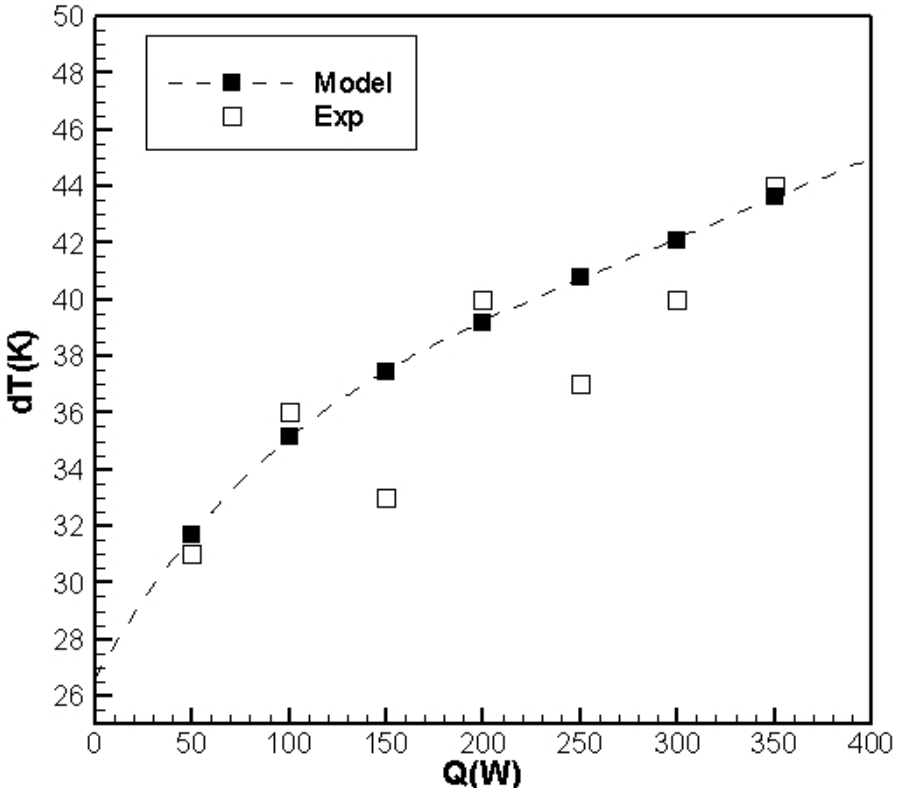

Fig. 2.7 Temperature drop vs. Heat input at T_{op}=20°

2.2.3 Effects of bubble number, meandering turn and gravity

In the previous section, the bubble number in Eq. (2-41) was replaced by the turn number to simulate the turn number effect on the oscillating motion and heat transfer performance in an OHP. If bubble generation and collapse are not considered, the bubble distribution and locomotion will be the only factor determining the bubble number in the evaporator. *Ne* in Eq. (2-41) becomes a function of *X*. To simplify the problem, it is assumed that vapor bubbles were uniformly distributed, and so were liquid plugs. Given the same schematic as Fig. 2.3, and the filling ratio as 50%, the periodic variation of bubble numbers along with locomotion of vapor plugs in the evaporator is presented in Fig. 2.8. The total bubble number is 25 and 50 respectively. Due to the discrete distribution of bubbles and evaporating turns, sometimes only part of a bubble is in the evaporating section, however it still count to 1 here, and hence the curves appear discontinuous. As shown in Fig. 2.8, if there are more bubbles in the system, i.e. higher total number, there would be more bubbles in the evaporator and the frequency of bubble number variation is also increased. To replace the discrete periodic variation in Fig. 2.8, a smoothing periodic function as shown below is presented:

$$N_e = \bar{N}_e + \tilde{N}_e \sin\left(2\pi X / l_{b+l}\right) \tag{2-55}$$

in which, over-bar presents the average value, tilde presents the deviation, and l_{b+l} is the length of a couple of bubble and liquid plug. And use this function in the previous calculations, the variations of average velocity and saturated temperature of

bubbles in evaporator with time are presented in Fig. 2.9 and 2.10 respectively. It could be found that, with 50 bubbles totally, the average velocity is higher and saturated temperature of bubble is lower, which means stronger convection and lower temperature drop between evaporator and condenser. The performance of OHP is definitely improved by having more bubbles in it. The results also show that although the convection is enhanced by adding more bubbles, the stability of the system is worsened, which might result into the bubbles collapse. Therefore using the meandering turns to replace *Ne* is a good approximation.

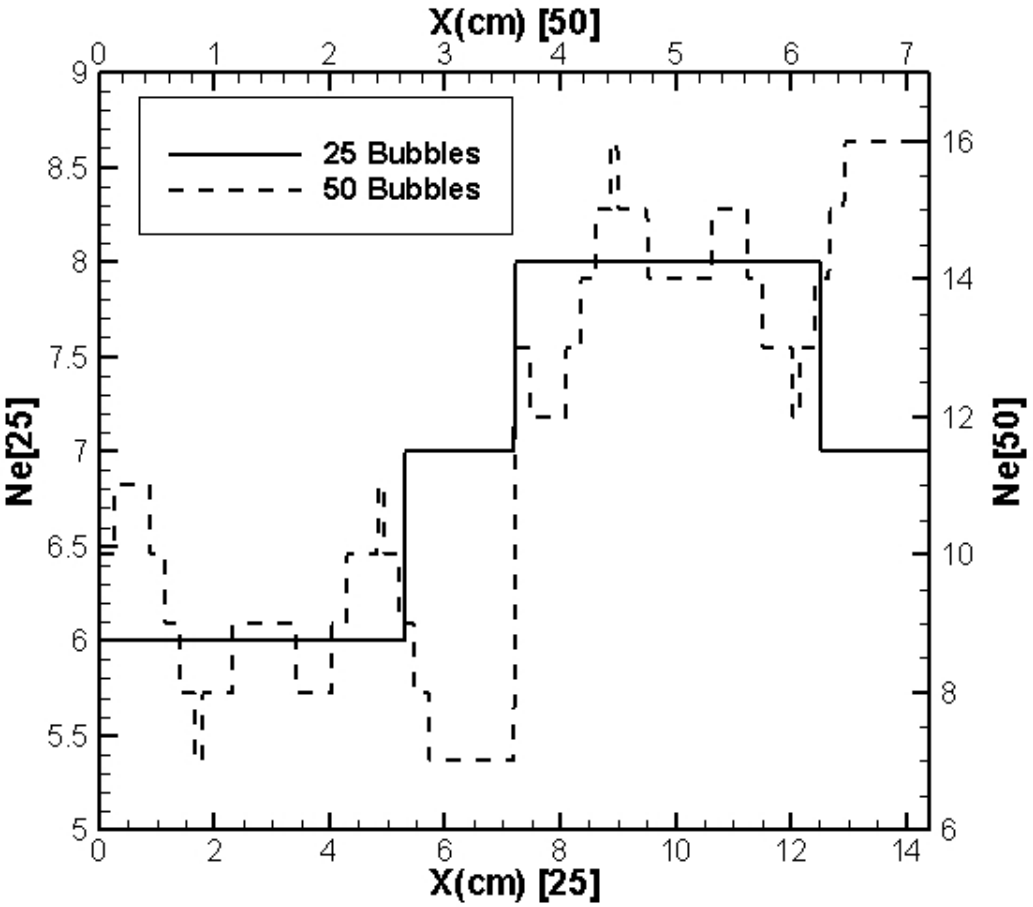

Fig. 2.8 Ne vs. X

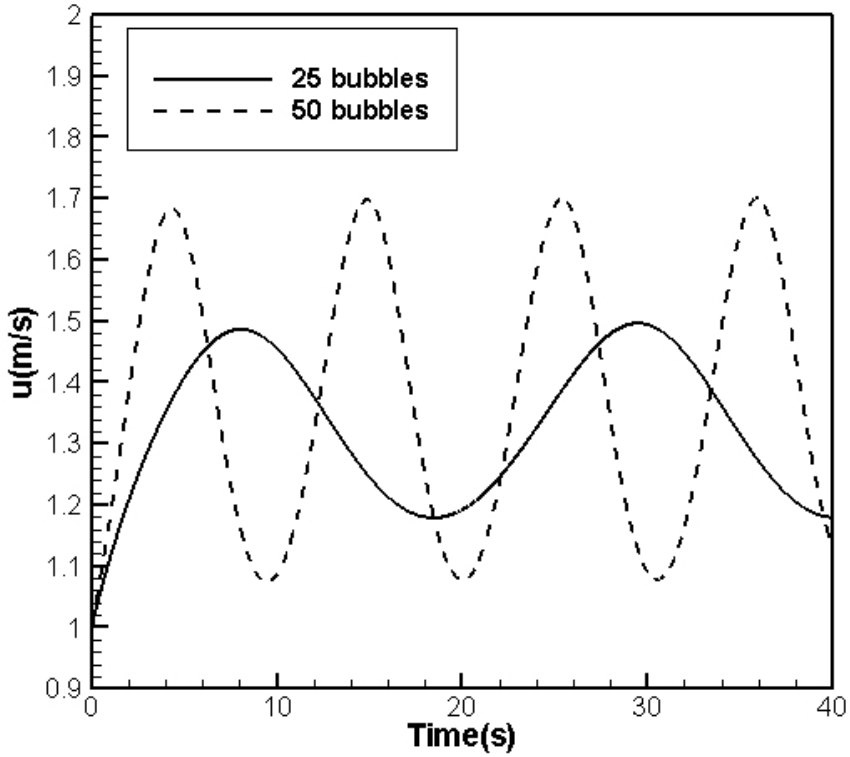

Fig. 2.9 u vs. time, 200W, Top=60°C

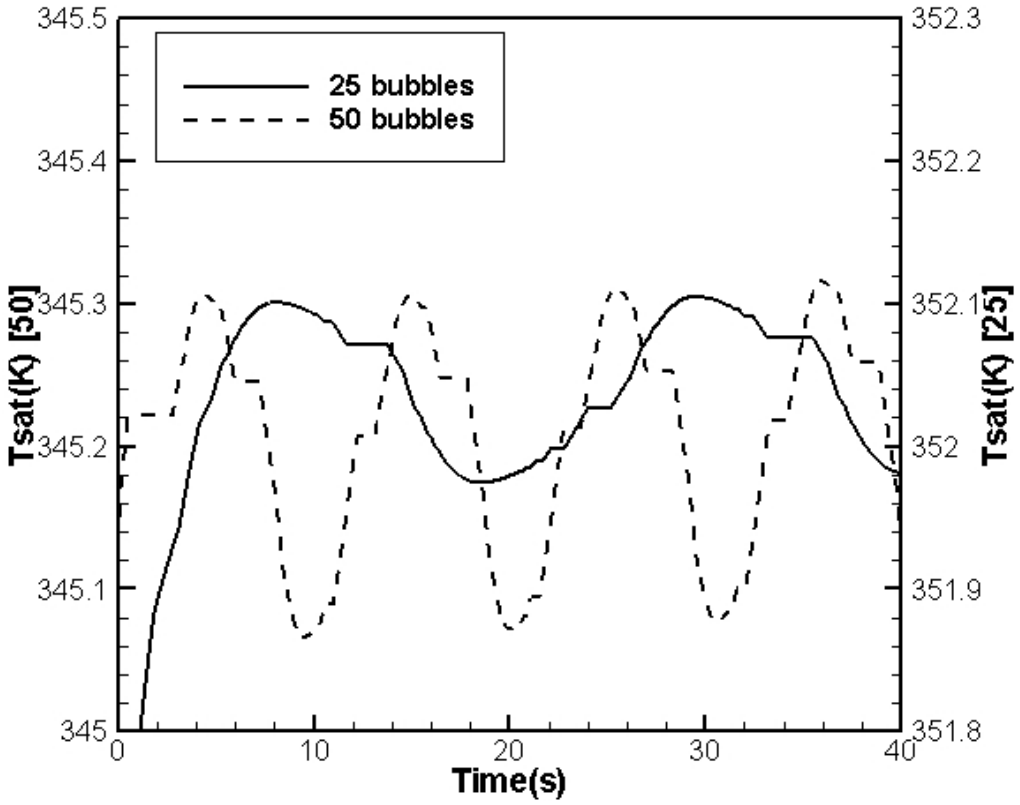

Fig. 2.10 Tsat vs. time, 200W, Top=60°C

As mentioned in one literature [4], a critical turn number exists for a CLOHP in the horizontal mode. Equation (2-41) can be used to explain this phenomenon: as the turn number decreases, a higher temperature drop between the evaporator and condenser is needed to keep the whole system running, however higher temperature means higher pressure drop between evaporator and condenser. It could be concluded that while the temperature drop exceeding some value, the momentum of liquid slugs might be not enough to overcome the very high pressure drop to come back from condenser and then the system is broken down.

In this literature, it was also reported that if a CLOHP worked in a bottom-heating mode, no such a critical turn number exists. Here come to see the effect of gravity. If the gravity is added into the model, Eq. (2-41) becomes:

$$\rho_l L_l \frac{d^2 X}{dt^2} + \left(f \bullet \mathrm{Re}_l\right) \frac{\mu_l L_l}{2 D_h^2} \frac{dX}{dt} + \rho_l g Y = \frac{R^2 \rho_{v0}}{c_p} N_{turn} \left(T_e - T_c\right) \tag{2-57}$$

where Y denotes the deviation of the center of mass from the balance position as shown in Fig. 2.1, and Y actually is the periodic function of X. With the Y term in, the meaning of the equation is very different, which has a similar mechanism to the system shown in Fig. 2.11. In this system, X presents the path of the ball. The driving force needs to do much less work to make the system startup if the gravity effect is included. In other words, if the gravity is included, the system is more unstable as shown in Fig. 2.12, i.e., it is easier to stimulate the oscillation. With more bubbles in the CLOHP, the gravity effect can be reduced. The bubble number is also one factor for system instability. Hence, the bottom-heating mode can definitely

increase the heat transfer performance of CLOHPs. From Fig. 2.13, it is also noticed that the gravity can also decrease the temperature drop between the evaporator and condenser.

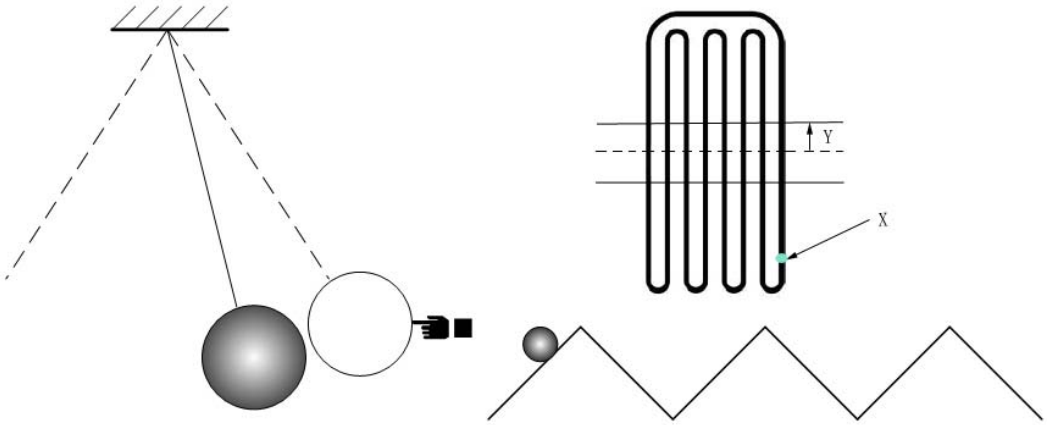

Fig. 2.11 Gravity effect

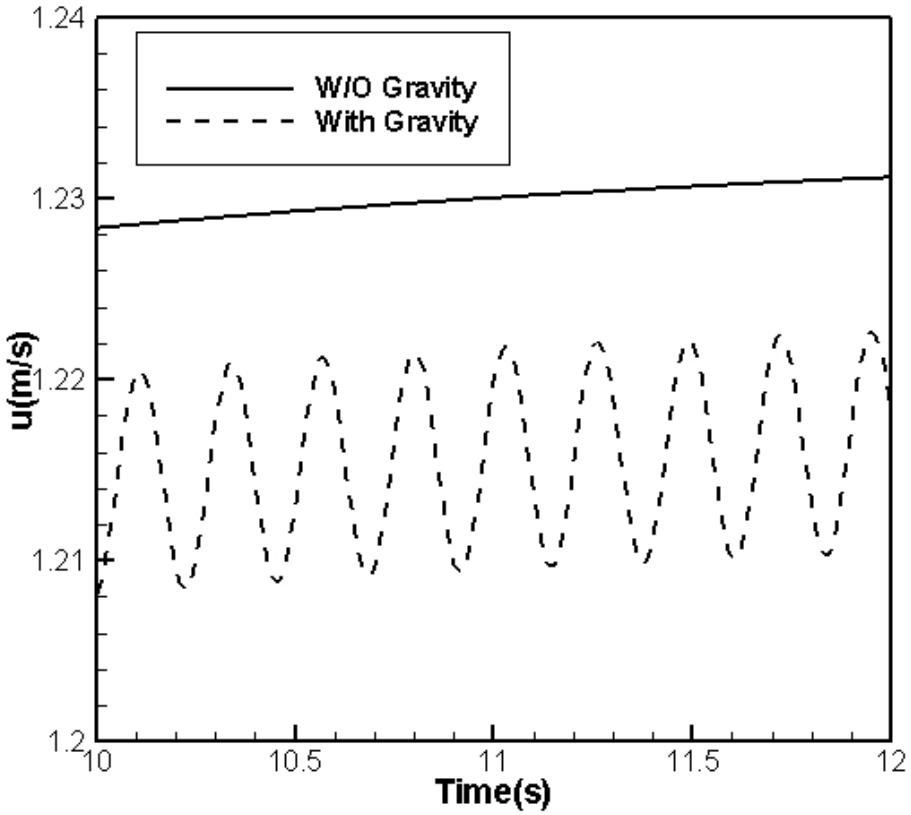

Fig. 2.12, u vs. time, 200W, Top=60°C

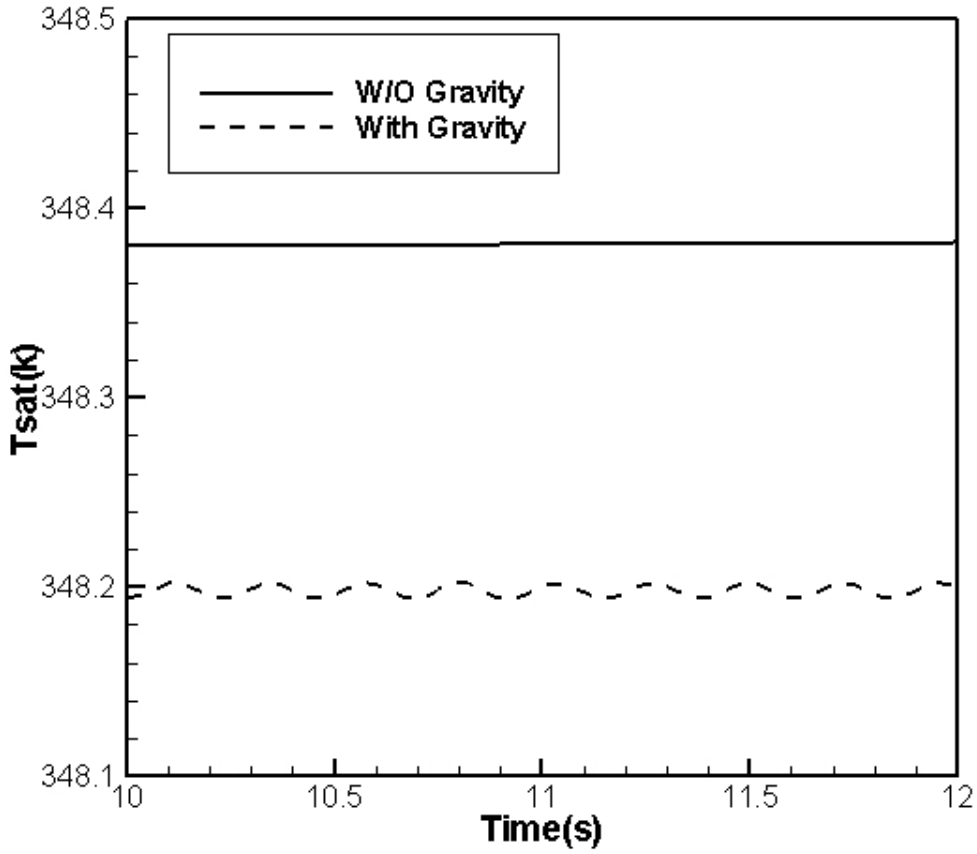

Fig. 2.13 Tsat vs. time, 200W, Top=60°C

2.3 Conclusions

The theoretical model revealed that in the multi-degree vibration of vapor bubbles and liquid plugs in the OHP, vapor bubbles played as linear springs. With continuous volume varying of liquid plugs and vapor bubbles, the system vibration mode shifts smoothly. Both bubble number and gravity affect the system stability. However, the bubble number in the evaporator, which determines the average liquid

plug velocity, can be replaced by the turn number. In this way, it is better to explain the turn number effect in a CLOHP. As the turn number increases, the temperature drop between the evaporator and condenser decreases. The model presented herein can be used to predict the heat transfer performance of a CLOHP. The model can be used to predict the percentage of sensible heat over the total heat, which depending on the operating temperature and input heat. The gravitational force can help to enhance the heat transfer performance of CLOHPs.

CHAPTER 3 HEAT TRANSFER ANALYSIS IN AN OHP

3.1 Heat transfer in the evaporator

When heat is added on the evaporator of the OHP, the heat is transferred through the heat pipe wall and reaches liquid-vapor interface formed between the vapor bubble and liquid plugs. In order to increase the evaporating heat transfer, porous wicks such as sintered particles are added to the tube wall, the temperature drop would be reduced dramatically comparing with smooth wall. Clearly, thin film evaporation does occur in the evaporator of an OHP

3.1.1 Thin film evaporation

3.1.1.1 Theoretical analysis

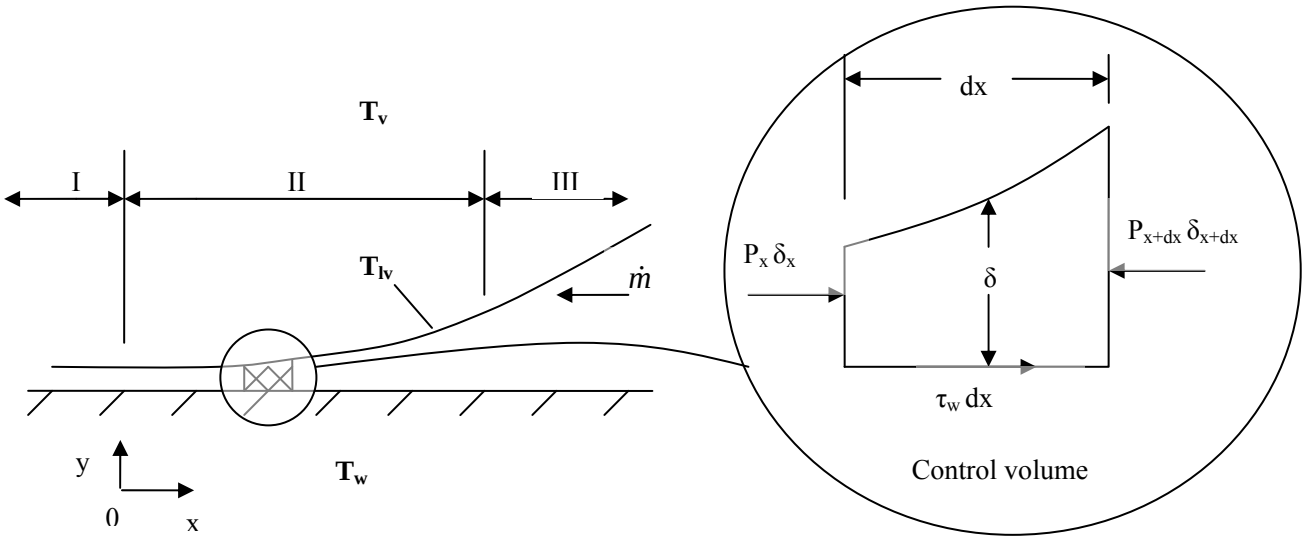

Fig. 3.1: Liquid film on a flat surface with the non-evaporating (I), evaporating thin film (II), and meniscus (III) regions.

For a typical thin film region, as shown in Fig. 3.1, it consists of the non-evaporating film region (Region I), evaporating thin film region (Region II) and meniscus region (Region III). The previous investigation [42] shows that when heat is added on the thin film regions, most of the heat transfers through the evaporating thin film region. In order to develop the equations governing the fluid flow and heat transfer in the evaporating thin film region, a control volume shown in Fig. 3.1 is taken, and the following assumptions are made, i.e., 1) the temperature on the wall is uniform equal to T_w;, 2) the interfacial waves on the fluid flow in the thin film region are neglected; 3) the physical properties are constant at a given temperature; 4) the pressure jump across the liquid-vapor interface is calculated by the Laplace-Young equation; and 5) the disjoining pressure is determined by $p_d = \frac{A}{\delta^3}$ where A is Hamaker's constant. For the control volume shown in Fig. 3.1, the pressure in the liquid film can be found as:

$$p = P_R - \frac{A}{\delta^3} - \sigma K \tag{3-1}$$

where P_R is the reference pressure, δ is the film thickness, and σ is the surface tension. The meniscus curvature, K, can be directly related to the film thickness by:

$$K = \frac{\frac{d^2\delta}{dx^2}}{\left[1+\left(\frac{d\delta}{dx}\right)^2\right]^{3/2}} \tag{3-2}$$

Based on the order analysis, the momentum equation for the control volume in the thin film evaporating region can be written as:

$$\rho_l \frac{\partial u}{\partial t} + \rho_l u \frac{\partial u}{\partial x} = -\frac{3A}{\delta^4}\frac{\partial \delta}{\partial x} + \sigma \frac{\partial K}{\partial x} + \mu_l \frac{\partial^2 u}{\partial x^2} + \mu_l \frac{\partial^2 u}{\partial y^2} \tag{3-3}$$

If the flow is steady and laminar, Eq. (3-3) becomes:

$$\frac{\rho_l}{2}\frac{\partial u^2}{\partial x} = -\frac{3A}{\delta^4}\frac{\partial \delta}{\partial x} + \sigma \frac{\partial K}{\partial x} + \mu_l \frac{\partial^2 u}{\partial x^2} + \mu_l \frac{\partial^2 u}{\partial y^2} \tag{3-4}$$

Integrating Eq. (3-3) in the y-direction from zero to the film thickness results in:

$$\frac{\rho_l}{2}\frac{\partial}{\partial x}\left(\int_0^{\partial} u^2 dy\right) = -\frac{3A}{\delta^4}\frac{\partial \delta}{\partial x}\int_0^{\delta} dy + \sigma \frac{\partial K}{\partial x}\int_0^{\delta} dy + \mu_l \frac{\partial^2}{\partial x^2}\left(\int_0^{\partial} u dy\right) + \mu_l \int_0^{\delta} \frac{\partial^2 u}{\partial y^2} dy \tag{3-5}$$

Assuming that the velocity, u, in the y direction could be expressed as $u = \bar{u} + u'$, where $\bar{u}$ is the mean velocity and u' is the fluctuating velocity, it can be found that: $\int_0^{\delta} u dy = \bar{u}\delta$ and $\int_0^{\delta} u' dy = 0$. Hence, Eq. (3-5) could be expressed as:

$$\frac{\rho_l}{2}\frac{\partial}{\partial x}\left(\bar{u}^2\delta + \int_0^{\delta} u'^2 dy\right) = -\frac{3A}{\delta^4}\frac{\partial \delta}{\partial x}\delta + \sigma \frac{\partial K}{\partial x}\delta + \mu_l \frac{\partial^2 \bar{u}\delta}{\partial x^2} + \mu_l \left.\frac{\partial u}{\partial y}\right|_0^{\delta} \tag{3-6}$$

where $\int_0^{\delta} u'^2 dy$ could be ignored and $\mu_l \left.\frac{\partial u}{\partial y}\right|_0^{\delta} = -\mu_l \left.\frac{\partial u}{\partial y}\right|_0$ due to free flow at the liquid-vapor interface. Therefore, Eq. (3-6) can be reduced to:

$$\frac{\rho_l}{2}\frac{\partial}{\partial x}\left(\bar{u}^2\delta\right) = -\frac{3A}{\delta^4}\frac{\partial \delta}{\partial x}\delta + \sigma \frac{\partial K}{\partial x}\delta + \mu_l \frac{\partial^2 \bar{u}\delta}{\partial x^2} + \mu_l \left.\frac{\partial u}{\partial y}\right|_0 \tag{3-7}$$

The mass flow rate across the thin film region is determined by:

$$\dot{m} = \bar{u}\rho_l\delta \tag{3-8}$$

Evaporation along the interface between liquid and vapor results in a change in mass flow rate in the x-direction based on the superheat and film thickness:

$$\frac{\partial \dot{m}}{\partial x} = \frac{q''}{h_{lv}} = \frac{k_l(T_w - T_{lv})}{h_{lv}\delta} \tag{3-9}$$

The shear stress along the wall surface can be expressed as:

$$\tau_w = \mu_l \left.\frac{\partial u}{\partial y}\right|_0 = \frac{(f \cdot \mathrm{Re})\mu_l \bar{u}}{8\delta} \tag{3-10}$$

Here it is noticed that the velocity $\bar{u}$ should be negative. To help simplify the equations, assume that $\bar{u}$ is positive and then replace it in Eqs. (3-8) and (3-10) by $-\bar{u}$. Combining Eq. (3-7) with Eqs. (3-8) and (3-10), the governing equation becomes:

$$\frac{3A}{\delta^4}\frac{\partial \delta}{\partial x}\delta - \sigma\frac{\partial K}{\partial x}\delta + \frac{\partial}{\partial x}\left(\frac{1}{2}\dot{m}\bar{u} + \frac{\mu_l}{\rho_l}\frac{\partial \dot{m}}{\partial x}\right) = \frac{(f\,\mathrm{Re})\mu_l \bar{u}}{8\delta} \tag{3-11}$$

Based on Eqs. (3-8) and (3-9), Eq. (3-11) can be expressed as:

$$\frac{3A}{\delta^4}\frac{\partial \delta}{\partial x}\delta - \sigma\frac{\partial K}{\partial x}\delta + \frac{\partial}{\partial x}\left(\frac{1}{2}\dot{m}\bar{u} + \frac{\mu_l k_l (T_w - T_{lv})}{\rho_l h_{lv}\delta}\right) = \frac{(f\,\mathrm{Re})\mu_l \dot{m}}{8\rho_l \delta^2} \tag{3-12}$$

From Eqs. (3-8) and (3-9), it could be also obtained that:

$$\frac{\partial \bar{u}}{\partial x} = \frac{k_l (T_w - T_{lv})}{\rho_l h_{lv}\delta^2} - \frac{\bar{u}}{\delta}\frac{\partial \delta}{\partial x} \tag{3-13}$$

The interface temperature shown in Eq. (3-13) is determined by integrating the Clausius-Clapyron equation and is represented as follows:

$$T_{lv} = T_v\left(1 + \frac{\Delta p}{\rho_v h_{lv}}\right) \tag{3-14}$$

where $\Delta p = K\sigma + \frac{A}{\delta^3}$.

In order to solve the governing equations presented above, appropriate boundary conditions must be determined. The calculation starts from the non-evaporation region where the boundary conditions satisfy:

$$\begin{cases} \dot{m}\big|_0 = 0 \\ \bar{u}\big|_0 = 0 \\ K\big|_0 = 0 \\ T_{lv}\big|_0 = T_w \\ \delta\big|_0 = \delta_0 = \left(\dfrac{T_v A}{(T_w - T_v)\rho_v h_{lv}} \right)^{1/3} \\ -\left(\dfrac{1.5A}{\delta^3} + \sigma K \right)\delta + \dfrac{1}{2}\dot{m}\bar{u} + \dfrac{\mu_l k_l (T_w - T_{lv})}{\rho_l h_{lv} \delta}\Bigg|_0 = -\dfrac{1.5A}{\delta_0^2} \end{cases} \tag{3-15}$$

It is noticed that the boundary condition of $\frac{\partial \delta}{\partial x}$ is not given. If it is assumed that $\frac{\partial \delta}{\partial x}$=0, then all of the equations should represent the non-evaporation region and there is no change for each variable solved. On the other hand, in the evaporating region, the boundary condition for $\frac{\partial \delta}{\partial x}$ should be positive i.e. $\frac{\partial \delta}{\partial x} > 0$, and it should be determined by the superheat, T_w-T_{lv}, or heat load and the contact angle.

To solve all of the governing equations, a 4th order Runge-Kutta method was implemented. If $F = -\left(\frac{1.5A}{\delta^3} + \sigma K \right)\delta + \frac{1}{2}\dot{m}\bar{u} + \frac{\mu_l k_l (T_w - T_{lv})}{\rho_l h_{lv} \delta}$, and $\frac{\partial \delta}{\partial x} = G$, the governing equations become:

$$\frac{\partial F}{\partial x} = \frac{(f \cdot \mathrm{Re})\mu_l \dot{m}}{8\rho_l \delta^2} - \sigma K G \tag{3-16}$$

$$\frac{\partial \dot{m}}{\partial x} = \frac{k_l (T_w - T_{lv})}{h_{lv} \delta} \tag{3-17}$$

$$\frac{\partial \bar{u}}{\partial x} = \frac{k_l (T_w - T_{lv})}{\rho_l h_{lv} \delta^2} - \frac{\bar{u}}{\delta} G \tag{3-18}$$

$$\frac{\partial G}{\partial x} = K\left(1 + G^2\right)^{3/2} \tag{3-19}$$

$$\frac{\partial \delta}{\partial x} = G \tag{3-20}$$

At node x_n, the values of F_n, $\dot{m}_n$, $\bar{u}_n$, δ_n, G_n, K_n and $T_{lv,n}$ are known. By

the five first order PDEs above, F_{n+1}, $\dot{m}_{n+1}$ $\dot{m}_n$, $\overline{u}_{n+1}$, δ_{n+1} and G_{n+1} were obtained.

In order to determine the two unknowns (K_{n+1} and $T_{lv,n+1}$), the following expression for F is described in discrete form as.:

$$F_{n+1} = -\left(\frac{1.5A}{\delta_{n+1}^3} + \sigma K_{n+1}\right)\delta_{n+1} + \frac{1}{2}\dot{m}_{n+1}\overline{u}_{n+1} + \frac{\mu_l}{\rho_l}\frac{k_l\left(T_w - T_{lv,n+1}\right)}{h_{lv}\delta_{n+1}} \tag{3-21}$$

The numerical form for Eq. (3-15) can be written as:

$$T_{lv,n+1} = T_v\left[1 + \frac{\sigma K_{n+1} + \dfrac{A}{\delta_{n+1}^3}}{\rho_v h_{lv}}\right] \tag{3-22}$$

Solving these two equations, the two unknown values could be obtained by:

$$\left(\delta_{n+1} + \frac{C_T T_v}{h_{lv}\rho_v}\right)\sigma K_{n+1} = -F_{n+1} - \left(1.5\delta_{n+1} + \frac{C_T T_v}{h_{lv}\rho_v}\right)\frac{A}{\delta_{n+1}^3} + \frac{1}{2}\dot{m}_{n+1}\overline{u}_{n+1} + C_T\left(T_w - T_v\right) \tag{3-23}$$

where $C_T = \dfrac{\mu_l k_l}{\rho_l h_{lv}\delta_{n+1}}$.

3.1.1.2 Results and Discussion

Unless stated otherwise, the physical properties for each of the studies below were based on the saturated water and vapor at 305 K. The gradient of the film thickness with respect to location at the non-evaporating region, G_0, is determined with the program by assuming there is no curvature in the bulk region (disjoining pressure less than 0.01 Pa), i.e. K=0. In order to verify the prediction by the current model, the prediction by the current model is compared with previous models [43].

As shown in Eq. (3-3), when the terms related to the inertial force are not considered, the current model is similar to the models presented by Demsky and Ma [43] and the results agree well with the prediction by Desmky and Ma [43].

Figure 3.2 illustrates the variation of the temperature at the liquid-vapor interface for various superheats. In the non-evaporating thin film region, the interfacial thermal resistance is so large that the temperature at the liquid-vapor interface equal to the wall temperature, and no evaporation occurs in this region. As the location approaches the bulk region, the interfacial thermal resistance reduces and the temperature at the liquid-vapor interface decreases significantly in the evaporating thin film region and becomes close to the vapor temperature in the meniscus region if the curvature in the meniscus region is small. Figure 3.3 shows the superheat effect on the liquid film profile in the evaporating thin film region. As shown, when the superheat increases, the liquid film thickness in the evaporating thin film region significantly increases as the location approaches the bulk region. In other words, the contact angle significantly increases as the superheat increases. However, the non-evaporating film thickness becomes thinner and the interfacial thermal resistance at the non-evaporating film region increases as the superheat increases. Figure 3.4 displays the superheat effect on the heat transfer rate through the evaporating thin film region. When the superheat increases, the heat transfer rate through the evaporating thin film region, as shown in Fig. 3.4, significantly increases. At a superheat of 1 K, the heat transport peaks at roughly 8.5e5 W/m^2. Because of these

high values it is a goal to increase this thin film evaporating region. As shown in Fig. 3.4, heat flux drastically drops off at a location where the film thickness is increased. It is also important to notice the large increase in heat flux due to an increase in wall superheat.

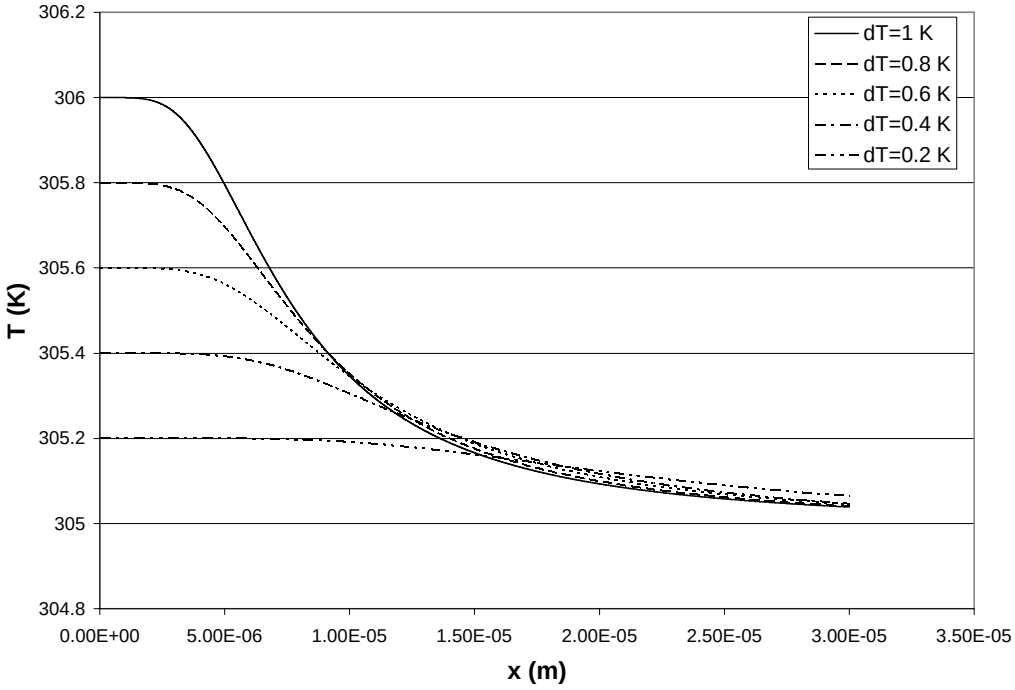

Fig. 3.2: Superheat effect on the liquid-vapor interface temperature.

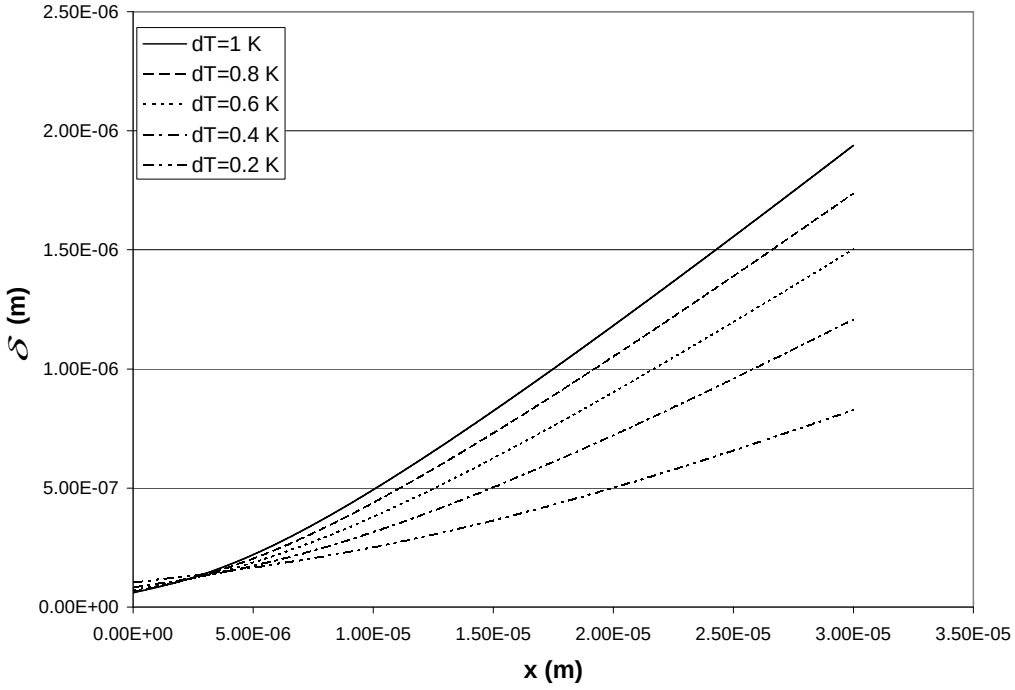

Fig. 3.3: Superheat effect on the liquid film thickness

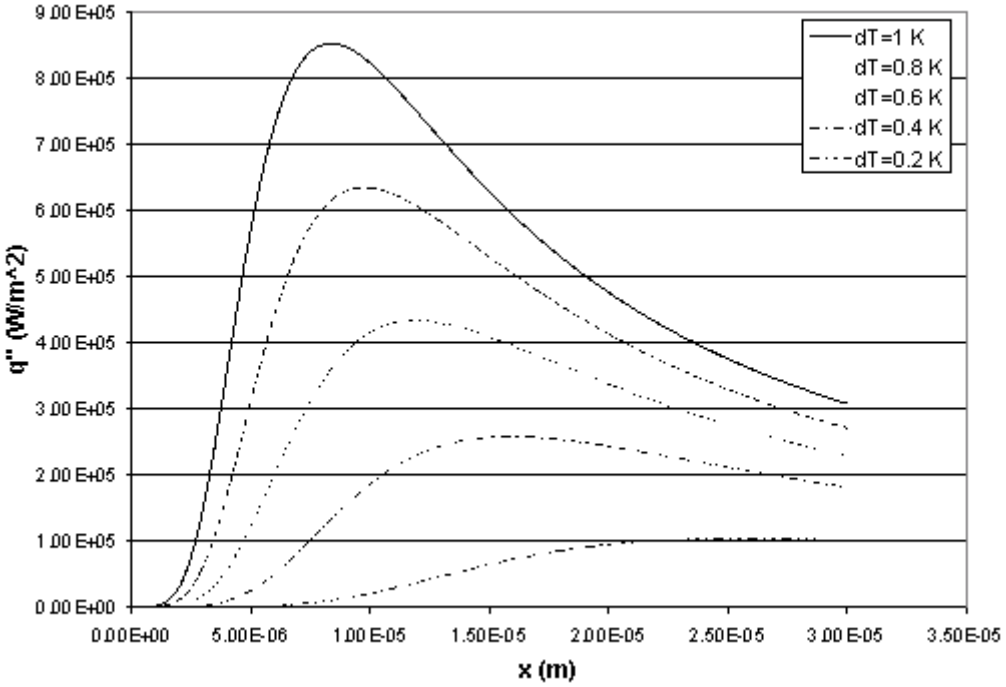

Fig. 3.4: Superheat effect on the heat flux distribution

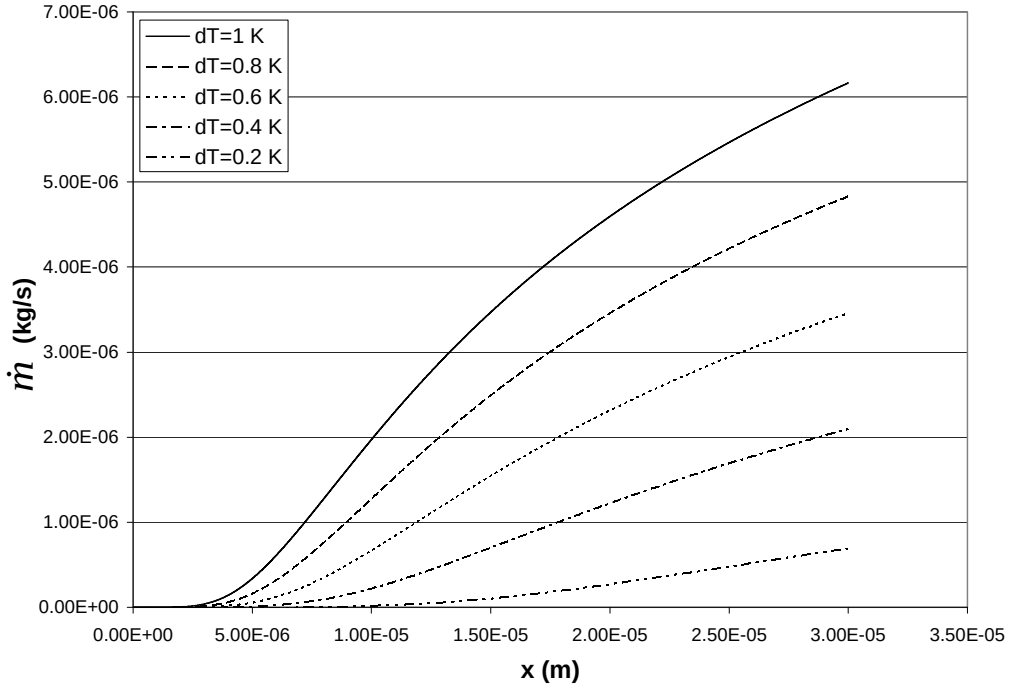

Fig. 3.5: Superheat effect on the mass flow rate.

The model can be used to predict the mass flow rate shown in Fig. 3.5 and the average velocity shown in Fig. 3.6. While the mass flow rate increases as the location approaches to the meniscus region, there exists a maximum average velocity in the evaporating thin film region. And it can be found that for a given superheat, the location where the maximum average velocity exists is different from that where the maximum heat flux exists. For example, at a superheat of 1.0 K, while the maximum average velocity occurs at x=1.35e-0.5 m, the maximum heat flux occurs at x=8.34e-0.6 m. Figure 3.7 shows the superheat effect on the curvature of liquid-vapor interface. As shown, there exists a maximum curvature for a given superheat. The location for the peak value of curvature is also different from that for the peak value

of heat flux through the thin film region.

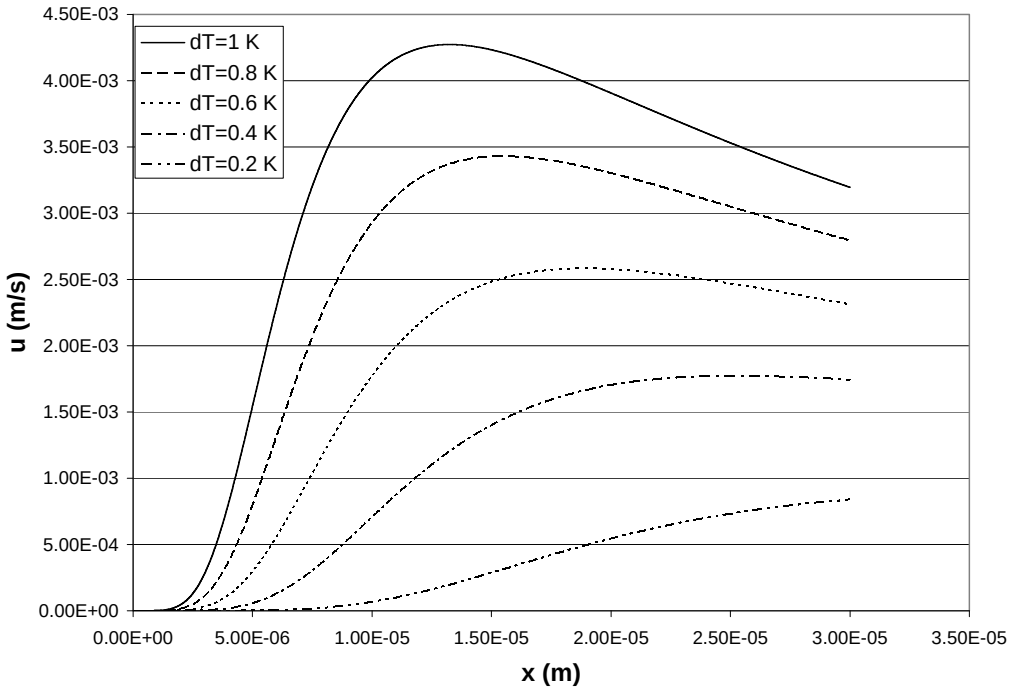

Fig. 3.6: Superheat effect on the average velocity

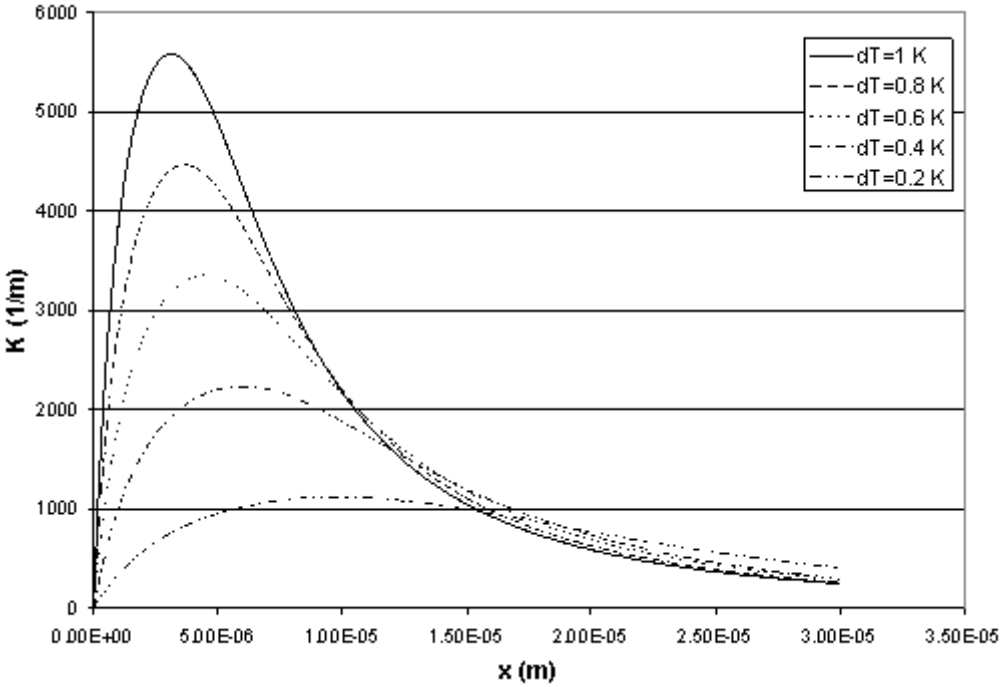

Fig. 3.7: Superheat effect on the curvature

3.1.2 Application of thin film evaporation in rectangular micro grooves

Micro heat pipes utilizing axial grooves as the wicking structure have become widely used in many industries as an efficient means of heat transport. Their usages range from electronics cooling to thermal control of spacecrafts. Heat pipes are a passive phase change heat transfer devices that use a wicking structure to supply the evaporator with fluid and also to create more thin film evaporating regions. Previous studies have shown that large increases in heat transport can be achieved by increasing the thin film evaporating region. The thin film evaporating region is an extended meniscus beyond the apparent contact line at a liquid/solid interface. The thin film is formed from surface tension and disjoining pressure effects at the solid and liquid interface. The fluid flow and evaporation in the thin film region is caused by disjoining pressure and surface tension of the working fluid. Heat transfer also occurs in the bulk fluid region of the axial groove by conduction. Combining heat transfer in both the thin film region and the bulk region will lead to a more complete model. This model can then be used to more accurately model heat transfer in a grooved heat pipe and allow for better optimization of the wicking structures in existing heat pipes.

3.1.2.1 Bulk region

In order to determine the heat transfer through the bulk fluid region, the

temperature distribution must be calculated. The temperature distribution in the bulk region can be determined by the following two-dimensional steady state energy equation:

$$\frac{\partial^2 T}{\partial x^2}+\frac{\partial^2 T}{\partial y^2}=0 \tag{3-24}$$

The wall material is assumed to have a relatively high thermal conductivity and the small dimension of the groove makes it reasonable to assume a constant wall temperature. Therefore, the boundary conditions associated with this problem are:

$$\begin{aligned} T &= T_w \quad at \quad x=\pm W \\ T &= T_w \quad at \quad y=0 \\ T &= T_{lv} \quad at \quad y=H^* \end{aligned} \tag{3-25}$$

where the liquid-vapor interface temperature is equal to the vapor temperature for the bulk region and H^* is the height of interface and can be calculated based on the geometry given in Fig. 3.8 and the assumption of a circular meniscus:

$$H^* = H - r_e\left(\cos\beta - \cos\theta\right) \tag{3-26}$$

$$\beta = \arcsin\left(\frac{x}{r_e}\right),\quad \theta = \arcsin\left(\frac{W}{r_e}\right). \tag{3-27}$$

To simplify and make the governing equation more universal, non-dimensional variables are defined as follows:

$$\phi = \frac{T_w - T}{T_w - T_{lv}},$$

$$\eta = x/W ,$$

(3-28)

$$\varsigma = y/H$$

$$K = W/H ,$$

Substituting the non-dimensional variables into Eq.(3-24) and the boundary conditions given by Eq.(3-25), Eq. (3-24) is converted to:

$$\frac{\partial^2 \phi}{\partial \eta^2} + K^2 \frac{\partial^2 \phi}{\partial \varsigma^2} = 0$$

(3-29)

$$\phi = 0 \quad at \quad \eta = \pm 1 \quad or \quad \varsigma = 0$$

$$\phi = 1 \quad at \quad \varsigma = \varsigma^* ,$$

where $\varsigma^* = H^*/H$.

Using separation of variables method the general solution to problem can be solved as:

$$\phi = \sum_{n=1}^{\infty} C_n \cos\left(\frac{2n-1}{2}\pi\eta\right)\sinh\left(\frac{2n-1}{2K}\pi\varsigma\right).$$

(3-30)

Applying the boundary condition: $\varsigma = \varsigma^*$ results in the following solution:

$$\phi = \sum_{n=1}^{\infty} C_n \cos\left(\frac{2n-1}{2}\pi\eta\right)\sinh\left(\frac{2n-1}{2K}\pi\varsigma^*\right) = 1$$

(3-31)

In order to solve for the constant C_n in a power series, the Galerkin method was used as follows:

$$\begin{pmatrix} A_{11} & A_{12} & \cdots & A_{1n} \\ A_{21} & A_{22} & \cdots & A_{2n} \\ \vdots & \vdots & \vdots & \vdots \\ A_{n1} & A_{n2} & \cdots & A_{nn} \end{pmatrix} \begin{pmatrix} c_1 \\ c_2 \\ \vdots \\ c_n \end{pmatrix} = \begin{pmatrix} b_1 \\ b_2 \\ \vdots \\ b_n \end{pmatrix}$$

(3-32)

where

$$A_{ij} = \int_{-1}^{1} \cos\left(\frac{2i-1}{2}\pi\eta\right)\cos\left(\frac{2j-1}{2}\pi\eta\right)\sinh\left(\frac{2i-1}{2K}\pi\varsigma^*\right)\sinh\left(\frac{2i-1}{2K}\pi\varsigma^*\right)d\eta$$

(3-33)

$$b_i = \int_{-1}^{1} \cos\left(\frac{2i-1}{2}\pi\eta\right)\sinh\left(\frac{2i-1}{2K}\pi\varsigma^*\right)d\eta$$

(3-34)

Once the temperature distribution is determined by the Galerkin method, the heat flux on the leftl, right and bottom surface can be determined by:

$$q_l'' = -k\left.\frac{\partial T}{\partial x}\right|_{x=-W} = \frac{k\left(T_w - T_{lv}\right)}{W}\left.\frac{\partial\phi}{\partial\eta}\right|_{\eta=-1} \qquad (3\text{-}35)$$

$$q_r'' = q_l''$$

(3-36)

$$q_b'' = \frac{k\left(T_w - T_{lv}\right)H}{H}\left.\frac{\partial\phi}{\partial\varsigma}\right|_{\varsigma=0}$$

(3-37)

where

$$\frac{\partial\phi}{\partial\eta} = -\sum_{n=1}^{\infty}\frac{2n-1}{2}\pi C_n \sin\left(\frac{2n-1}{2}\pi\eta\right)\sinh\left(\frac{2n-1}{2K}\pi\varsigma\right)$$

(3-38)

$$\frac{\partial \phi}{\partial \varsigma} = \sum_{n=1}^{\infty} \frac{2n-1}{2K} \pi C_n \cos\left(\frac{2n-1}{2}\pi\eta\right) \cosh\left(\frac{2n-1}{2K}\pi\varsigma\right)$$

(3-39)

Basing on equations above, the heat flux per meter of bulk liquid region at the evaporator can be obtained as

$$q'_{total} = q'_l + q'_r + q'_b \tag{3-40}$$

where

$$q'_l = q'_r = k\left(T_w - T_{lv}\right) \sum_{n=1}^{\infty} C_n \sin\left(\frac{2n-1}{2}\pi\right) \cosh\left(\frac{2n-1}{2K}\pi\varsigma\right)\Big|_0^1 \tag{3-41}$$

$$q'_b = k\left(T_w - T_{lv}\right) \sum_{n=1}^{\infty} C_n \sin\left(\frac{2n-1}{2}\pi\eta\right)\Big|_{-1}^1 \tag{3-42}$$

3.1.2.2 Results

3.1.2.2.1 Error Analysis

To determine the error of the Galerkin approximation method, the error function is defined as:

$$\left\|e_n\right\| = \sqrt{\frac{\int_{-1}^{1} \left(\phi_n - \phi\right)^2 d\eta}{\int_{-1}^{1} \phi^2 d\eta}}$$

(3-43)

where n denotes the number of terms used in the Galerkin approximation. The error was determined for three cases in which the term number is equal to 3, 4, or 5,..

Figure 3.9 shows non-dimensionless temperatures of the Galerkin approximation using 3, 4 or 5 terms. The non-dimensional value at the meniscus was determined to be one, and it is clearly shown that five terms results in the best approximation among three cases. $\|e_n\|$ for the three cases were calculated to be 15.8 %, 34.1 %, and 10%, respectively. The results show that more terms do not necessarily mean a better approximation for the solution, however, five terms resulted in the best approximation with a 10 % error. The calculated error is at the meniscus which is much greater than the error from the rest of the bulk region.

3.1.2.2.2 Solution

A Fortran code was developed to solve the governing equations for the thin film region using a fourth order Runge-Kutta method. A numerical method was implemented to calculate the temperature at the liquid-vapor interface. The length of the thin film evaporating region was determined by the calculated film thickness. It was assumed that as the film thickness becomes larger than 2 μm (i.e. $\delta \geq 2\,\mu m$) or when the disjoining pressure is approximately equal to 0.01 Pa, the thin film governing equations are no longer valid and the liquid film was considered as the bulk fluid. Constant fluid properties for water at a temperature of 305 K were used for the calculation.

The solution to the governing equation for heat transfer through the bulk region was determined by implementing the Galerkin method as stated. A Fortran code was

created to numerically integrate the matrix terms and calculate the power series constants. The contour plot for a given groove geometry is shown in Fig. 3.10 for a superheat of 1 K. The heat transfer rate was then calculated by Eqs. (1.28) and (1.29) using a given groove dimension. The rectangular groove width and height were set at 0.08 mm (i.e. W=0.04 mm) and 0.146 mm, respectively. The values for the contact angle and wall superheat were varied from 0^o to 60^o and 0.5 K to 5 K, respectively, in both the thin film and bulk heat transfer calculations. The effects of these two parameters on the heat transfer rate through of the thin film and bulk regions were investigated.

Figure 3.11 shows the heat transfer contributions of each region along with total heat transfer per longitudinal length along the groove for various wall superheats. For this case contact angle between the liquid and the surface was set to 0^o. As shown, there is a larger increase in the thin film heat transfer per unit length for increasing wall superheat than for the bulk region heat transfer, which appears to have a linear relationship. On the other hand, the effect of increasing contact angle on both heat transfer regions seems to have a similar effect as shown in Fig. 3.12. Both contributions to heat transfer decrease as the contact angle is increased. For the thin film region, this decrease is because a larger contact angle results in a smaller thin film region area. As the contact angle was increased from 0^o to 60^o, the length before the film thickness reaches 2 μm is reduced from 30.8 μm to 25.3 μm, respectively. The contact angles effect on the bulk region heat transfer is due to a

larger amount of fluid in the groove which increases the thermal resistance through this area.

To evaluate the overall effectiveness for the rectangular micro groove given various wall superheats and contact angles, the heat transfer coefficient was calculated for the groove. Figures 3.13 and 3.14 display the total heat transfer coefficient for the combined regions for different values of wall superheat and contact angle, respectively. As can be seen, the heat transfer coefficient decreases for both increasing wall superheat and contact angle. This makes sense considering the heat flux per length for both regions were decreased as the contact angle was increased.

One of the goals of this investigation was to determine the contribution of both the thin film and bulk region heat transfer to the overall heat transfer. In order to determine this, the ratio of the thin film heat transfer to the overall heat transfer was plotted in Fig 3.15 and 3.16 for various wall superheats and contact angles, respectively. For an increase in wall superheat, the contribution of thin film heat transfer reduces from 84 % to 77 % while increasing wall superheat from 0.5 K to 5 K. In contrast, an increase in contact angle increases the amount of heat transfer in the thin film evaporating region with respect to the bulk region. This is because the relative drop in thin film heat transfer is far less than that for bulk region. The key is to reduce the contact angle in order to extend the length of the thin film region and reduce the thermal resistance through the bulk region.

The investigation presented herein has resulted in a model that determines the heat transfer through both the thin film and bulk regions of a fluid in a rectangular micro groove. The model has shown that for a given contact angle and wall superheat, the contribution of the heat transfer through the bulk region can be as high as 23 % of the total heat transfer. It also is shown that the heat transfer contribution for the two regions varies for different contact angles and wall superheats. This model would be a good tool to optimize groove dimensions to obtain a high level of heat transport through both regions.

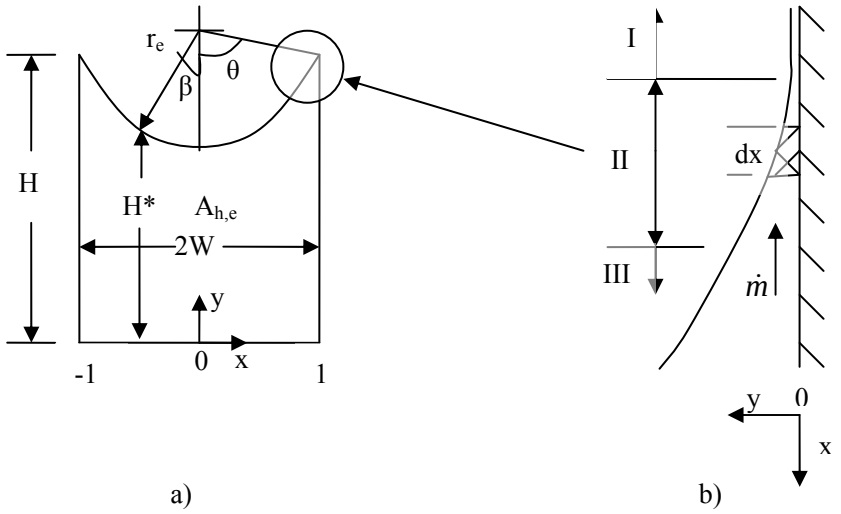

Fig. 3.8. Schematic of the groove and liquid meniscus in the evaporator (a) and the thin film region (b).

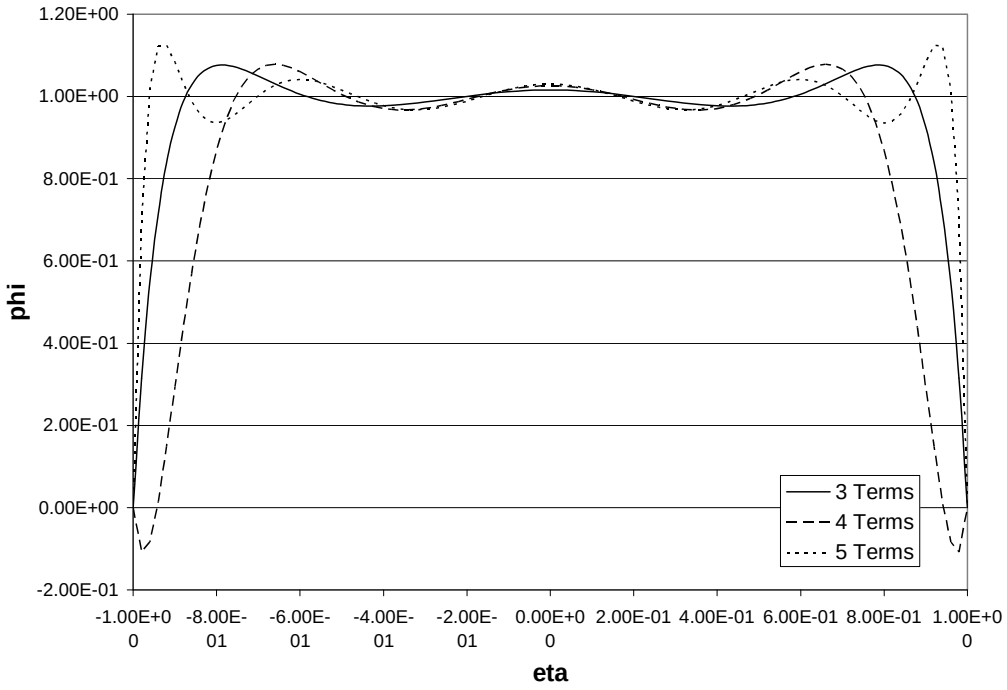

Fig. 3.9. Non-dimensional temperature at the meniscus using increasing number of terms in the Galerkin method.

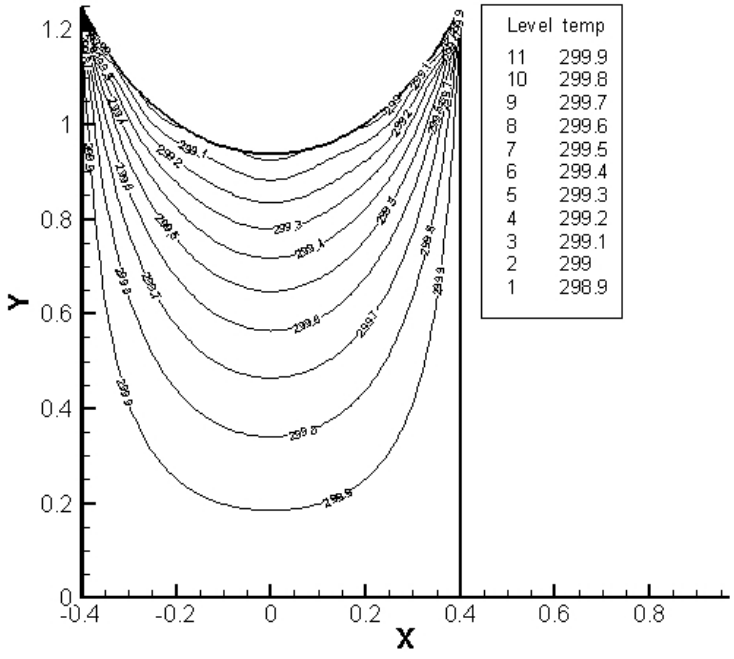

Fig. 3.10. Temperature distribution in the bulk region for a given groove geometry and a superheat of 1 K.

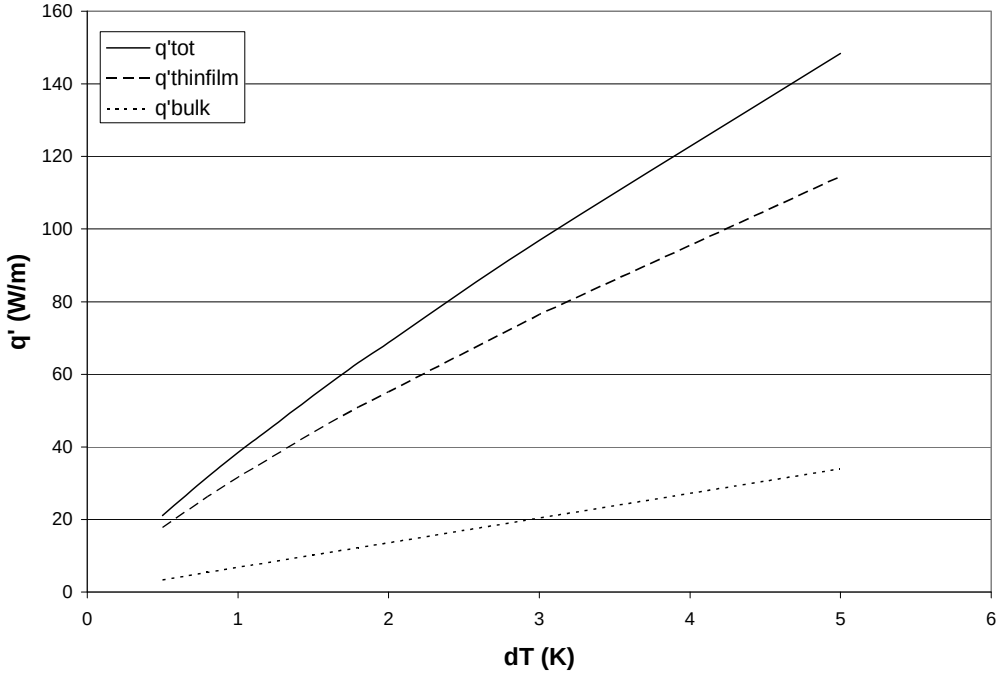

Fig. 3.11. Heat transfer per unit length versus wall superheat for both regions.

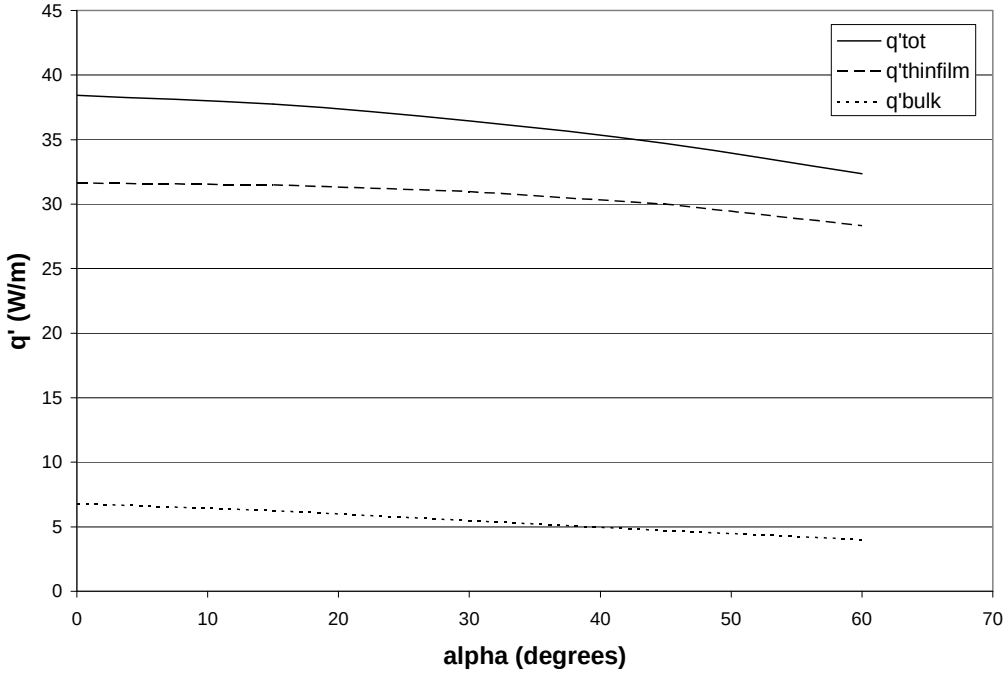

Fig. 3.12. Heat transfer per unit length versus contact angle for both regions.

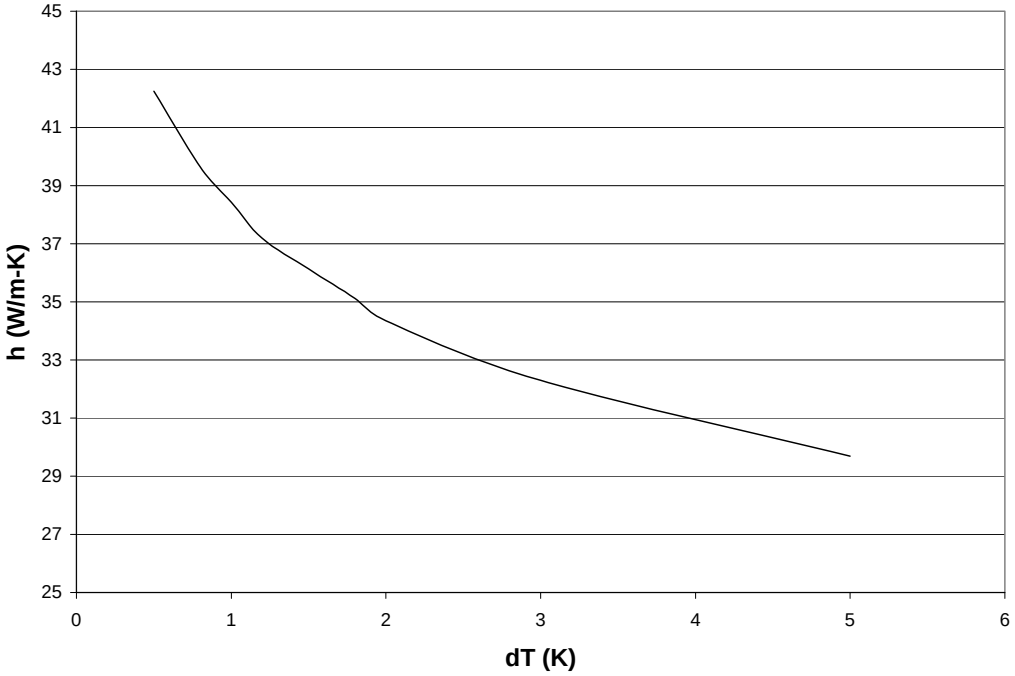

Fig. 3.13. Total heat transfer coefficient versus wall superheat for both regions.

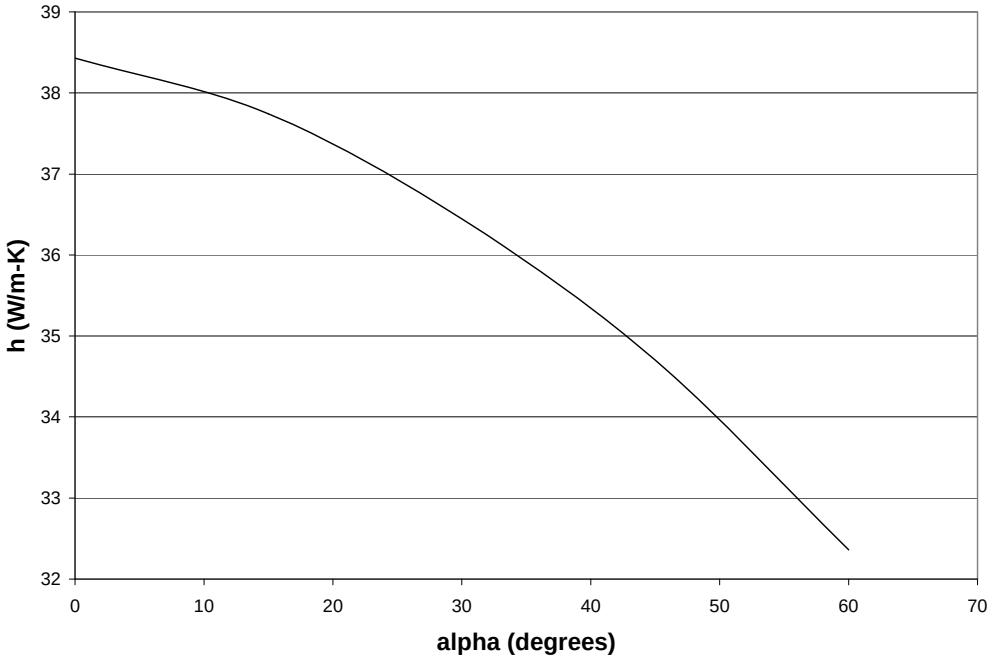

Fig. 3.14. Total heat transfer coefficient versus contact angle for both regions.

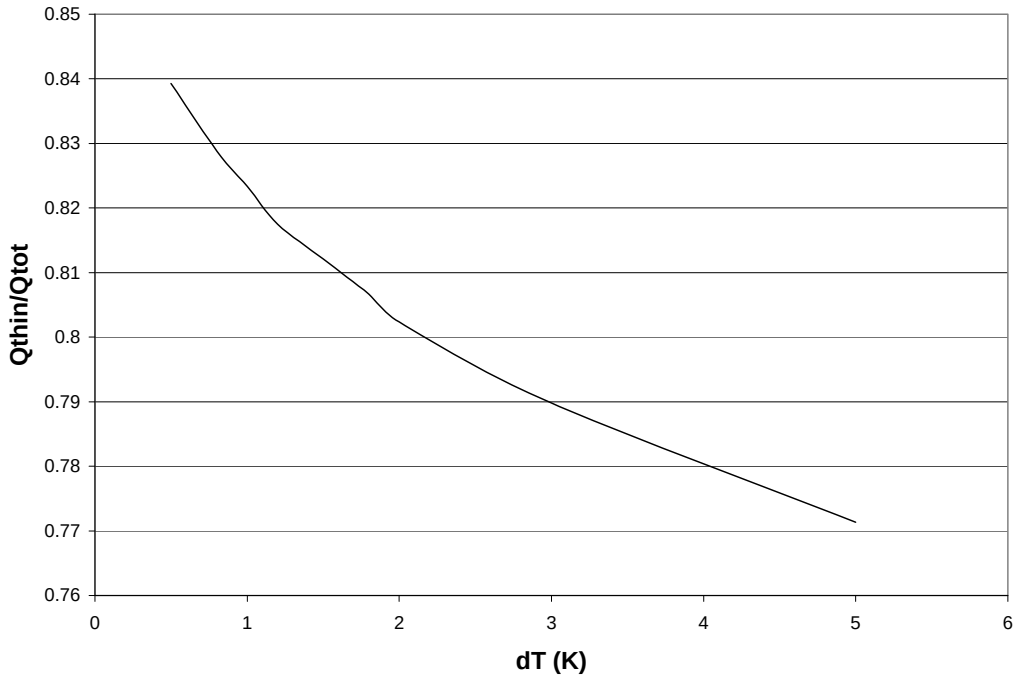

Fig. 3.15. Ratio of heat transfer in thin film region to total heat transfer versus wall superheat.

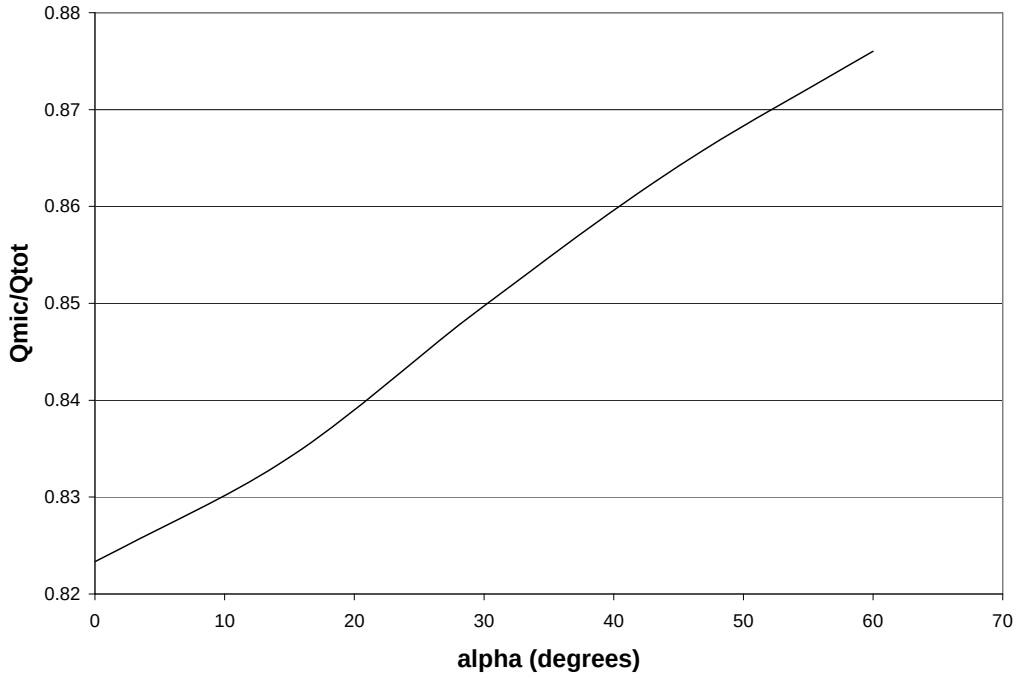

Fig. 3.16. Ratio of heat transfer in thin film region to total heat transfer versus contact angle.

3.1.3 Pulsating motion effect

From the discussion above about the heat transfer coefficient for convection boiling, one may have a question whether it is still valid for two-phase flow with pulsating motion. As introduced in Chapter 1, even for single-phase flow the problem how pulsation affect heat transfer is still not understood completely, no matter what regime the flow is (laminar or turbulent). For the OHP, the liquid slug flow could assume to be laminar or slug flow because the tube diameter is relatively small where surface tension has much more significant influence on the motion. The classical research of Wormley [44] and Uchida [45] has presented the exact solutions of the laminar pulsating flow field. The corresponding heat transfer problem has also been paid much attention and many research results have been presented in recent years. Some of the earliest research [46] demonstrated that the pulsating flow could enhance the heat transfer in a pipe. However some contradictive results were also obtained from the following research. For example, Zhao and Cheng [47], and Yu et al.. [48] found that the pulsating flow in a circular flow with a constant-heat-flux boundary condition has no effect on the convection heat transfer, basing on the analytical solution and numerical results they obtained. Moschandreou and Zamir [49] presented there exist a peak value of frequency for a pulsating flow, with a dimensionless value of 15, whereby the enhancement of heat transfer could be obtained, comparing with steady flow. When the dimensionless

frequency is smaller than 5 or bigger than 25, the pulsating flow would have negative effect on the heat transfer enhancement. However Hemida et al.[50] stated that the analytical solution obtained by Moschandreou and Zamir [49] was not correct. With their corrected solution, the effect of pulsation in the fully developed region was negligible. And in the thermally developing region, the heat transfer was more sensitive to the pulsation, but the spatial average Nusselt number presented negative effect. One interesting topic in their research was that they believed due to the linear boundary conditions applied in most of the published results there should be no enhancement of heat transfer by the pulsating flow, unless non-linear boundary conditions, e.g. radiation and natural convection, was combined with pulsating flow.

To simplify the problem and focus on how the oscillatory motion affects the heat transfer, assumption of sinusoidal slug flow in a circular tube was made. With this assumption, the velocity in the tube is function only with respect to time and could be expressed as:

$$u = u_m\left(1+\gamma\cos\omega t\right) \tag{3-44}$$

The energy equation is:

$$\frac{\partial T}{\partial t}+u\frac{\partial T}{\partial x}=\alpha\frac{1}{r}\frac{\partial}{\partial r}\left(r\frac{\partial T}{\partial r}\right) \tag{3-45}$$

Boundary and initial conditions are:

$$r=0,\ \frac{\partial T}{\partial r}=0 \tag{3-46}$$

$$r=r_0,\ -k\frac{\partial T}{\partial r}=q''_w$$

(3-47)

$$x = 0\,,\ \ t = 0\,,\ \ T = T_0$$

(3-48)

Equation (3-46) indicates that the flow comes into the tube with uniform temperature at the entrance. The dimensionless variables are defined as: $u^* = \frac{u}{u_m}$, $r^* = \frac{r}{r_0}$, $\omega^* = \frac{\omega r_0^2}{\nu}$, $t^* = \frac{\nu t}{r_0^2}$, $x^* = \frac{2x}{\mathrm{Re}_m \,\mathrm{Pr}\, r_0}$, $\theta = \frac{k\left(T_0 - T\right)}{q_w'' r_0}$, and $\mathrm{Re}_m = \frac{2u_m r_0}{\nu}$.

With these dimensionless variables, Eqs. (3-44) and (3-45) become:

$$u^* = 1 + \gamma \cos \omega^* t^* \tag{3-49}$$

$$\mathrm{Pr}\frac{\partial \theta}{\partial t^*} + u^* \frac{\partial \theta}{\partial x^*} = \frac{1}{r^*}\frac{\partial}{\partial r^*}\left(r^* \frac{\partial \theta}{\partial r^*}\right)$$

(3-50)

The boundary and initial conditions become:

$$r^* = 0,\ \ \frac{\partial \theta}{\partial r^*} = 0 \tag{3-51}$$
$$r^* = 1,\ \ \frac{\partial \theta}{\partial r^*} = 1$$

(3-52)

$$x^* = 0,\ \ t^* = 0\,,\ \ \theta = 0 \tag{3-53}$$

For the fully developed flow, it can be assumed that: $\theta\left(r^*, x^*, t^*\right) = \theta_s\left(r^*, x^*\right) + \theta_t\left(r^*, t^*\right)$ [49]. Hence Eq. (3-50) could be divided into two equations:

$$\begin{cases} \dfrac{\partial \theta_s}{\partial x^*} = \dfrac{1}{r^*}\dfrac{\partial}{\partial r^*}\left(r^* \dfrac{\partial \theta_s}{\partial r^*}\right) \\ r^* = 0,\ \ \dfrac{\partial \theta_s}{\partial r^*} = 0;\quad r^* = 1,\ \ \dfrac{\partial \theta_s}{\partial r^*} = 1 \end{cases}$$

(3-54)

$$\begin{cases} \Pr\dfrac{\partial\theta_t}{\partial t^*}+\gamma\cos\left(\omega^* t^*\right)\dfrac{\partial\theta_s}{\partial x^*}=\dfrac{1}{r^*}\dfrac{\partial}{\partial r^*}\left(r^*\dfrac{\partial\theta_t}{\partial r^*}\right) \\ r^*=0,\quad \dfrac{\partial\theta_t}{\partial r^*}=0;\quad r^*=1,\quad \dfrac{\partial\theta_t}{\partial r^*}=0 \end{cases}$$

(3-55)

The solution of Eq. (3-54) is:

$$\theta_s=2x^*+\frac{1}{2}r^{*2}+const$$

(3-56)

If assuming that at the center of the inlet, $\theta_s=0$ $(T=T_0)$, the constant in Eq. (3-56) could be zero.

If $\theta_t\left(r^*,t^*\right)=A\left(t^*\right)B\left(r^*\right)+C\left(t^*\right)$, Eq. (3-55) becomes:

$$\begin{cases} \Pr A'B=AB''+\dfrac{1}{r^*}AB' \\ \Pr C'+2\gamma\cos\left(\omega^* t^*\right)=0 \end{cases}$$

(3-57)

The solution of Eq. (3-57) can be expressed as:

$$\theta_t=\sum_{n=0}^{\infty}c_n J_0\left(\sqrt{\lambda_n}r^*\right)\exp\left(-\lambda_n t^*/\Pr\right)+\frac{-2\gamma}{\Pr\omega^*}\sin\left(\omega^* t^*\right) \quad (3\text{-}58)$$

where $\sqrt{\lambda_n}$ is the eigenvalue of the first kind of Bessel function of order 1. It is noticed that when n=0, $\sqrt{\lambda_n}=0$.

At the inlet, the following condition is satisfied: $\theta=\theta_s+\theta_t=0$ when $t^*=0$. Basing on this condition, the constant could be obtained and the final expression of θ_t can be written as:

$$\theta_t = \sum_{n=1}^{\infty} \frac{2J_2\left(\sqrt{\lambda_n}\right)}{\lambda_n J_0^2\left(\sqrt{\lambda_n}\right)} J_0\left(\sqrt{\lambda_n} r^*\right) \exp\left(-\lambda_n t^* / \mathrm{Pr}\right) + \frac{-2\gamma}{\mathrm{Pr}\,\omega^*} \sin\left(\omega^* t^*\right) - \frac{1}{4} \quad (3\text{-}59)$$

The time-dependent local Nusselt number is defined as:

$$Nu_{Dx,t} = \frac{h_{x,t} D}{k} = \frac{2q_w'' r_0}{k\left(T_w - T_m\right)}$$

(3-60)

$$Nu_{D_{x^*,t^*}} = \frac{-2}{\theta_w\left(x^*, t^*\right) - \theta_{bm}\left(x^*, t^*\right)}$$

(3-61)

where:

$$\theta_w\left(x^*, t^*\right) = \sum_{n=1}^{\infty} \frac{2J_2\left(\sqrt{\lambda_n}\right)}{\lambda_n J_0\left(\sqrt{\lambda_n}\right)} \exp\left(-\lambda_n t^* / \mathrm{Pr}\right) + \frac{-2\gamma}{\mathrm{Pr}\,\omega^*} \sin\left(\omega^* t^*\right) + 2x^* - \frac{1}{4}$$

(3-62)

$$\theta_{bm}\left(x^*, t^*\right) = \frac{\int_0^1 \theta u^* r^* dr^*}{\int_0^1 u^* r^* dr^*} = 2\int_0^1 \theta r^* dr^* = -\frac{2\gamma \sin\left(\omega^* t^*\right)}{\mathrm{Pr}\,\omega^*} + 2x^*$$

(3-63)

It is noticed that the first term in Eq. (3-62) will eliminate with time. It means the time-dependent local Nusselt number would reach to a constant when the system comes to a steady state. And it is also noticed that for any period velocity function $u = u_m\left[1 + \sum_{n=1}^{\infty}\left(a_n \cos \omega t + b_n \sin \omega t\right)\right]$, the same conclusion will be drawn. The conclusion indicated that the pulsating flow has no effect on the convection heat transfer of single-phase slug flow. It is also reasonable if extending it to the case of

two-phase convection boiling in the evaporator of OHP.

3.2 Heat transfer in the condenser

The vapor generated in the evaporating section is condensed in the condensing section if the phase-change driving force exists, and the condensate in the thin film region will flow into the liquid-slug region due to the capillary force. Because the film thickness in the condensing film region is very thin compared with the meniscus thickness in the liquid slug, most of the condensing heat transfer will occur in the thin film region. In this region, the Reynolds number of the condensate is very small, hence the inertial terms can be neglected and based on conservation of momentum in the thin film, the pressure drop due to the viscous flow can be found as:

$$\frac{dp_l}{ds} = \frac{f \cdot \mathrm{Re}_\delta \, \mu_l D_o q_c'' s}{2\delta^3 D_i \rho_l h_{fg}} \tag{3-64}$$

where

$$\mathrm{Re}_\delta = \frac{\bar{U}_{l,c} \delta \rho_l}{\mu_l}$$

(3-65)

By integrating Eq. (3-56) from s=0 to $L_{c,v}/2$ (half of the length of vapor in the condenser), the total pressure drop along half of the bubble length can be found as:

$$\Delta p_l = \int_0^{L_{c,v}/2} \left(\frac{f \cdot \mathrm{Re}_\delta \, \mu_l D_o q_c''}{2\delta^3 D_i \rho_l h_{fg}} \right) s ds$$

(3-66)

There exist numerous vapor slugs in the OHP including the condensing section.

Although the vapor slug distributions, i.e., vapor bubble number, in the OHP was unpredictable, the total vapor space was remained constant for a given liquid filled ratio, ϕ, which is defined as:

$$\phi = \frac{V_l}{V}$$

(3-67)

where V_l is the volume occupied by liquid, and V is the total volume throughout the heat pipe. It is assumed that all of the vapor slugs in the condensing region are combined into one large slug with condensation occurring on its perimeter. Assuming a uniform distribution of vapor throughout the entire length of the heat pipe, the length of the idealized single vapor slug in the condenser may be found by:

$$L_{c,v} = L_c\left(1-\phi\right)$$

(3-68)

The capillary pressure along the condensate film can be found as:

$$\frac{dp_c}{ds} = 2\sigma\frac{dK}{ds}$$

(3-69)

Integrating Eq. (3-61) from $K=1/r_o$ to $K=1/r_c$, the total capillary pressure can be found as:

$$\Delta p_c = 2\sigma\left(\frac{1}{r_c}-\frac{1}{r_0}\right)$$

(3-70)

where r_o is the meniscus radius of the liquid-vapor interface at the line of symmetry, i.e., at s=0, and r_c is the meniscus radius of the liquid-vapor interface at the liquid slug, i.e., at $s=L_{c,v}$, which can be found by:

$$r_0 = \frac{1}{2}\left(D_i - 2\delta_0\right)$$

(3-71)

and

$$r_c = \frac{1}{2}\left(D_i - 2\delta_{0.5L_{c,v}}\right)$$

(3-72)

respectively. Considering Eqs. (3-63) and (3-64), the total capillary pressure can be rewritten as:

$$\Delta p_c = 2\sigma\left[\frac{1}{\left(\frac{D_i}{2}-\delta\right)} - \frac{1}{\left(\frac{D_i}{2}-\delta_0\right)}\right]$$

(3-73)

For the steady-state condensation process of the thin film, the capillary pressure defined by Eq. (3-65) should be equal to the pressure drop determined by Eq. (3-58). With a given heat flux level, i.e., q_c'', Eqs. (3-58) and (3-65) can be readily solved and the condensation film thickness determined.

3.3 Conclusions

In this chapter, the thin film evaporation and condensation in an OHP are studied respectively. The pulsating motion of liquid, which is related to the convection heat

transfer in the OHP is also analyzed. A modified theoretical model of thin film evaporation involving the momentum effect is presented, and the results showed that fluid momentum in the thin film region has almost no effect on the thin film profile and thin film evaporation. By applying this model to the evaporation heat transfer in a groove, where liquid-vapor interface is divided into two sub-region, i.e.: thin film and bulk region, the heat transfer rate through the thin film region and bulk region can be determined respectively and it is found that the heat transfer rate though thin film region is much higher than that through bulk region. Based on laminar flow of single phase, the pulsating flow effect on the convection heat transfer occurring in the OHP was studied and found that the pulsating flow cannot enhance the convection heat transfer for a single phase flow. Because the pulsating flow and its coupled heat transfer occurring in an OHP are much more complicated, the analysis conducted herein by using a single phase flow may not apply for the heat transfer and fluid flow phenomena occurring in an OHP. Clearly, it is necessary to conduct further investigation on this topic.

CHAPTER 4 OTHER FACTORS AFFECTING HEAT TRANSFER ENHANCEMENT IN AN OHP

4.1 Charging process effect on the non-condensable gas in the heat pipe

The non-condensable gas in a heat pipe will significantly affect the heat transfer performance. In order to prevent the non-condensable gas from the heat pipe, a number of charging methods have been developed such as the backing-filling, heating and condensation. These methods can be used to successfully charge various heat pipes. In the mass production, however, these methods may not be the best methods to charge the heat pipe. One approach to charge the heat pipe in the mass production is that after a pre-calculated amount of working fluid is charged to the heat pipe, the vacuum pump connecting to the heat pipe is on and off several times to vacuum the non-condensable gas. The on-time and off-time will directly affect the amount of non-condensable gas left in the heat pipe.

4.1.1 Mathematical model

After a pre-calculated amount of working fluid is charged into the heat pipe, the heat pipe is connected to the vacuum system as shown in Fig. 4.1. The charging tube has a length of L with an inside diameter of d_i ranging from 0.5 mm to 2.0 mm.

The vacuum pump can provide a vacuum pressure (absolute pressure) p_{vac}. Once the valve connecting the vacuum pump and the charging tube is on, the low pressure generated by the vacuum pump will pump air out from the heat pipe. The flow rate can be expressed as:

$$dm/d\tau = \rho u_m \pi D^2/4 = \frac{(p - p_{vac})\pi D^4}{128\nu L} \tag{4-1}$$

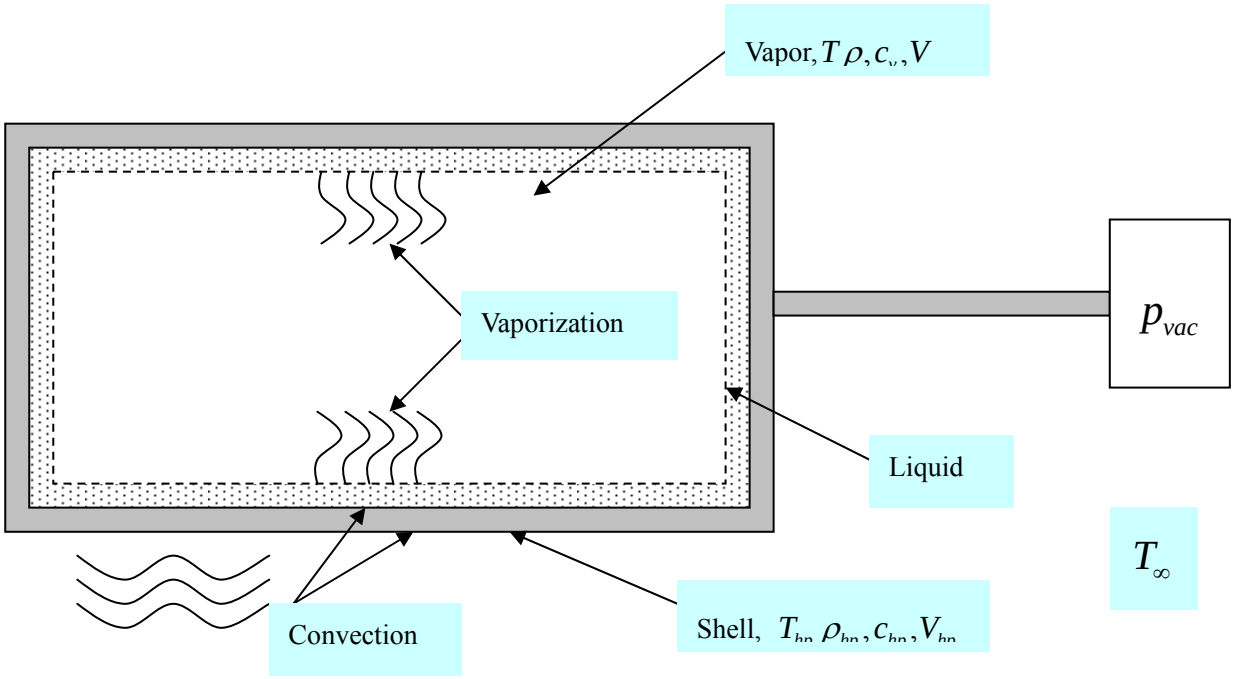

Fig. 4.1 Illustration of Mathematical Model

When the pressure in the heat pipe is lower than the saturation pressure corresponding to the saturation temperature, liquid vaporizes. When the heat pipe is connected to a vacuum pump, vapor is pumped out. Due to the liquid vaporization and the vapor mass loss from the heat pipe through the thin charging tubing, the heat pipe becomes colder than the ambient temperature. Continuous vaporization and mass

loss need the heat transferred from the ambient to the heat pipe. As shown in Fig. 4.1, when heat is transferred from the ambient to the shell by natural convection, the heat transfers through the shell and wick to the liquid in the wick where liquid vaporizes and becomes vapor.

Take the whole vapor in the heat pipe as the control volume, which is an open system with mass flow out through the charging tubing and mass flow in through the interface of vapor and liquid. The mass change rate in the heat pipe can be expressed as:

$$dm/d\tau = -V\frac{d\rho}{d\tau} + \frac{Q}{h_{fg}} \tag{4-2}$$

where V is the total vapor volume of heat pipe, ρ is the gas (vapor plus air) density, and Q is latent heat of the liquid.

Considering the heat transfer from ambient, taking the heat pipe shell including the wick as a control volume, heat transfer from outside and in, natural convection on both sides, the following equation could be obtained:

$$h_o A_{s,o}(T_\infty - T_{hp}) - h_i A_{s,i}(T_{hp} - T) = \rho_{hp} c_{hp} V_{hp}\frac{dT_{hp}}{d\tau} \tag{4-3}$$

where T presents the temperature of the liquid in the heat pipe, which equals to the temperature of vapor in the heat pipe.

Basing on this equation, the heat transferred from the shell and wick to the liquid could also be figured out, and the heat which liquid evaporation needs could be expressed as:

$$Q = h_i A_{s,i}(T_{hp} - T) - c_l m_l \frac{dT}{d\tau} \tag{4-4}$$

Then considering the open system of vapor in the heat pipe, the energy balance shows that:

$$0 = dE + h_{enthalpy,out}\dot{m}_{out} - h_{enthalpy,in}\dot{m}_{in} \tag{4-5}$$

Here assuming that there is no heat transfer between the vapor and liquid, all of the heat transferred into the liquid is used for evaporation. Replacing the terms with detail expression, Eq. (4-5) could be also written as:

$$0 = \rho c_v V \frac{dT}{d\tau} + c_p T \frac{dm}{d\tau} - c_{p,l} T \frac{Q}{h_{fg}} \tag{4-6}$$

It is noticed that the vapor in the heat pipe is the mixture of water vapor and non-condensed gas. In the vacuuming process, the percentage of non-condensed gas will decrease due to the liquid evaporation. Introduce a time-dependence variable x, presenting the mass percentage of non-condensed gas, into the system. The following expression of mass change rate of non-condensed gas could be obtained:

$$\frac{d(xm)}{d\tau} = -V \frac{d(x\rho)}{d\tau} \tag{4-7}$$

Combining with Eq. (4-2), the following equation could be obtained:

$$\frac{dx}{d\tau} = -\frac{x}{m + \rho V} \frac{Q}{h_{fg}} \tag{4-8}$$

From Eq. (4-7), it is also could be derived that:

$$\frac{d\left[x(m + \rho V)\right]}{d\tau} = 0 \Rightarrow x(m + \rho V) = \rho_0 V \tag{4-9}$$

where ρ_0 is the initial value of vapor density in the heat pipe.

Then Eq. (4-8) becomes:

$$\frac{dx}{d\tau} = -\frac{x^2}{\rho_0 V}\frac{Q}{h_{fg}} \tag{4-10}$$

The gas (vapor plus air) in the heat pipe can be assumed an ideal gas and according the law of partial pressure, the total pressure could be expressed as:

$$p = \rho RT = \rho\left[xR_{air} + (1-x) R_{vapor} \right]T \tag{4-11}$$

Similarly, the heat capacities of the vapor mixture are:

$$\begin{aligned} c_p &= xc_{p,air} + (1-x)c_{p,vapor} \\ c_v &= xc_{v,air} + (1-x)c_{v,vapor} \end{aligned} \tag{4-12}$$

Due to the continuous evaporation, liquid mss in the heat pipe will keep decreasing, such that m_l in Eq. (4-4) can not be a constant. This time-dependence variable could be obtained by Eq. (4-1):

$$m_l = m_{l0} - \int_0^\tau \frac{d(1-x)m}{d\tau} d\tau = m_{l0} - \int_0^\tau \frac{(1-x)\left(p - p_{vac} \right)\pi D^4}{128\nu L} d\tau \tag{4-13}$$

Arrange Eq. (4-1~4, 6, 10~13), the governing equations for transient charging are obtained:

$$\begin{cases} d\rho / d\tau = Q / h_{fg} V - \left(p - p_{vac} \right)\pi D^4 / 128\nu LV \\ dT / d\tau = \left[h_i A_{s,i} (T_{hp} - T) - Q \right] / c_l m_l \\ dT_{hp} / d\tau = \left[h_o A_{s,o} (T_\infty - T_{hp}) - h_i A_{s,i} (T_{hp} - T) \right] / \rho_{hp} c_{hp} V_{hp} \\ Q = \left[\dfrac{c_p T}{\rho c_v V} \dfrac{\left(p - p_{vac} \right)\pi D^4}{128\nu L} + \dfrac{h_i A_{s,i} (T_{hp} - T)}{c_l m_l} \right] / \left[\dfrac{c_{p,l} T}{h_{fg} \rho c_v V} + \dfrac{1}{c_l m_l} \right] \\ \dfrac{dx}{d\tau} = -\dfrac{x^2}{\rho_0 V}\dfrac{Q}{h_{fg}} \\ p = \rho RT \end{cases} \tag{4-14}$$

This group of equations could be solved by 4th order Runge-Kutta method.

4.1.2 Results and discussion

To verify the model, experiments of charging heat pipe are conducted. As shown in Fig. 4.2, a 265mm heat pipe with copper shell is tested. The outside diameter of the heat pipe is 7.9mm, inner diameter is 6.9mm. Then length of charging tubing is 10cm and the inner diameter is 0.762mm. The vacuum pump could offer pressure at 10Pa. Three thermal couples are set on the copper shell and one is set at the end of charging tubing to measure the vapor temperature.

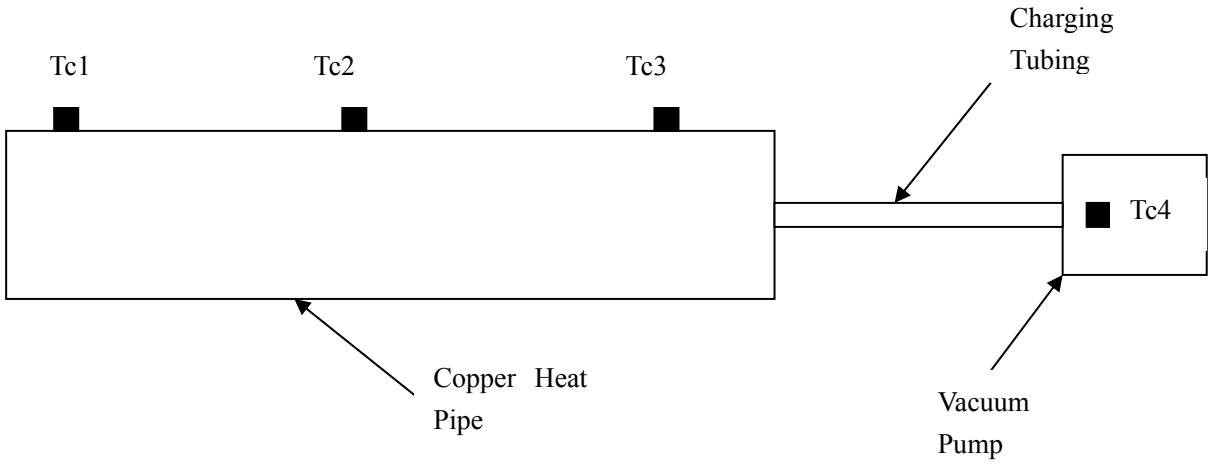

Fig. 4.2 Experimental Setup

In Fig. 4.3, the vapor and shell temperature variation in the experiments are separately compared with the predictions of mathematical model. They show that the model predictions match the experimental data very well. The difference should be mainly caused by the uncertain parameters in the experiments, such as the initial non-condensed gas percentage and the heat transfer coefficient in the heat pipe.

From the mathematical model, it is noticed that some parameters, such as the heat transfer coefficient, initial value of charging liquid mass and non-condensed vapor percentage, and charging tubing dimensions, determine the whole charging process of heat pipes.

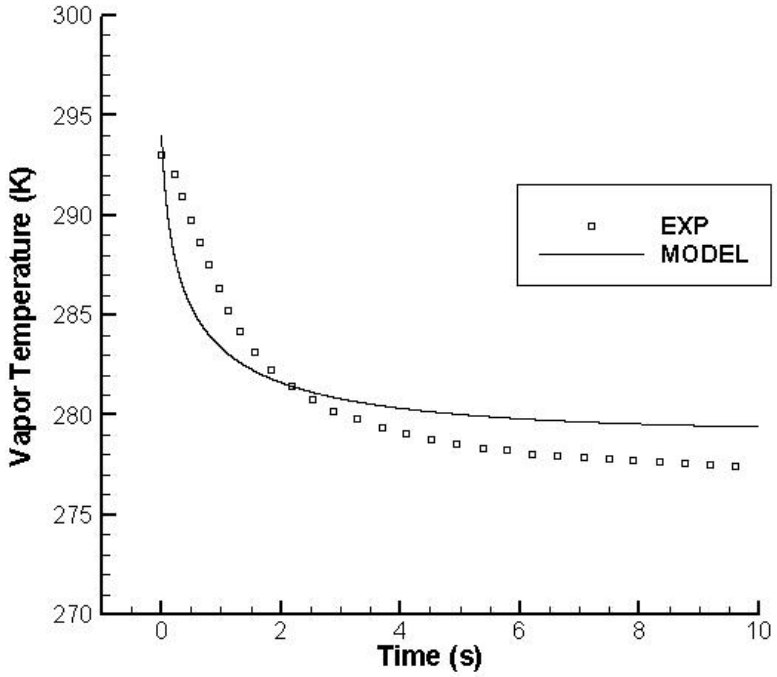

(a) Temperature Variation of the Vapor

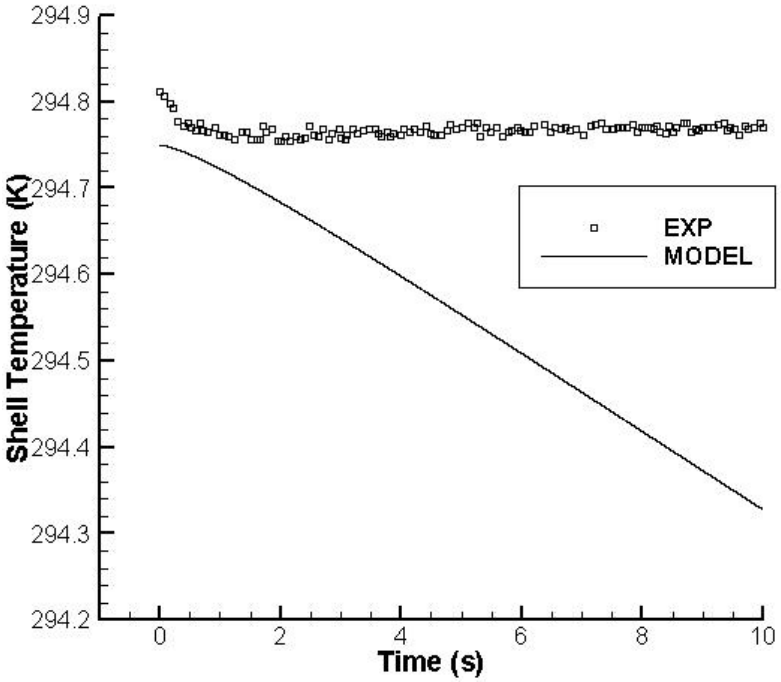

(b) Temperature Variation of the Heat Pipe Shell

Fig. 4.3 Comparison of Model Prediction and Experimental Data

Generally, the heat transfer coefficient for the interface of ambient air and heat pipe could be obtained basing on the operation environment. However, at the interface of heat pipe shell and liquid inside, the heat transfer coefficient is not easy to be figured out due to the rapid decreasing of liquid temperature. Fig. 4.4 shows how the heat transfer coefficient inside affect the temperature drop on the shell and vapor, and the vapor density variation. The results show that the heat transfer coefficient has obvious effect on the temperature drop of both shell and vapor, but little on the vapor density. In fact the temperature drop difference for different heat transfer coefficient is very small unless there exists forced convection in the heat pipe when the heat transfer coefficient inside has a big value. However, experimental results of the temperature drop on the heat pipe shell (Fig. 4.3(b)) indicate that there should no forced convection in the heat pipe and heat transfer coefficient decrease with time due to the great temperature drop of vapor or liquid. So it could be concluded that in the mathematical model the heat transfer coefficient could be taken as a constant presenting the natural convection on both interfaces of ambient-shell and shell-liquid. It would produce a little inaccuracy of temperature drop of shell and vapor which could be ignored however.

The effects of initial charging liquid mass on vapor temperature drop, vapor density and non-condensed gas percentage are shown in Fig. 4.5. Only the vapor temperature at steady state is obviously affected. With more liquid in the heat pipe, the temperature drop is smaller.

Fig. 4.6 shows the effect of initial value of non-condensed gas percentage. Generally, this parameter will influence all of the variables such as the temperature drop, vapor density and non-condensed gas percentage. The most interesting effect which may be useful in the technical application is that the non-condensed gas percentage variation is determined by its initial value greatly. Combining with the density variation, it could be found that when the system comes to the steady state, no matter how long vacuuming continues, the reduction of non-condensed gas in the heat pipe is very small.

Fig. 4.7 and Fig. 4.8 show how the dimensions of charging tubing such as diameter and length, affect the charging process. One reasonable conclusion is that the dimensions of charging tubing have significant effect on charging speed but little on the steady state value of temperature drop, vapor density and non-condensed gas percentage. The results also indicate that the effect of diameter is more obvious than the tubing length.

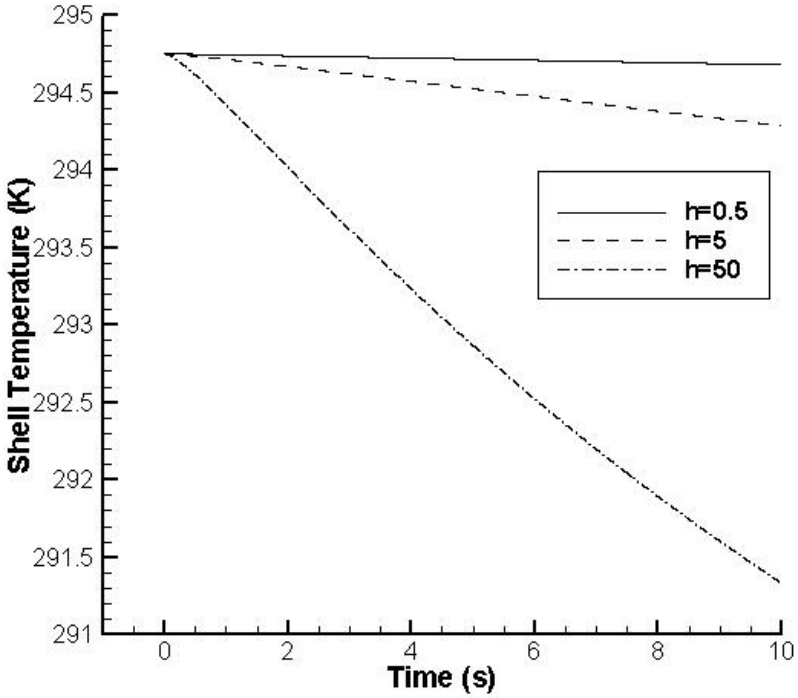

(a) Shell Temperature Variation with Time at Different *h*

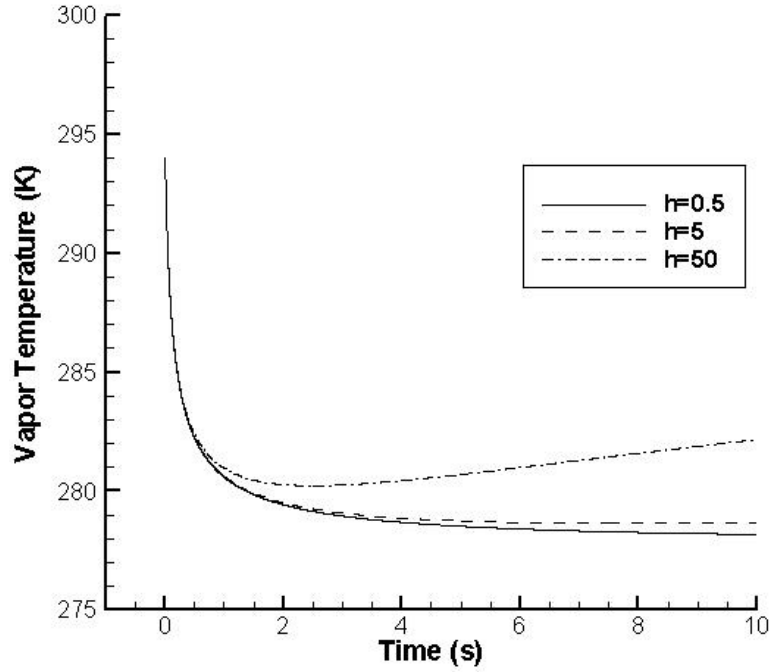

(b) Vapor Temperature Variation with Time at Different *h*

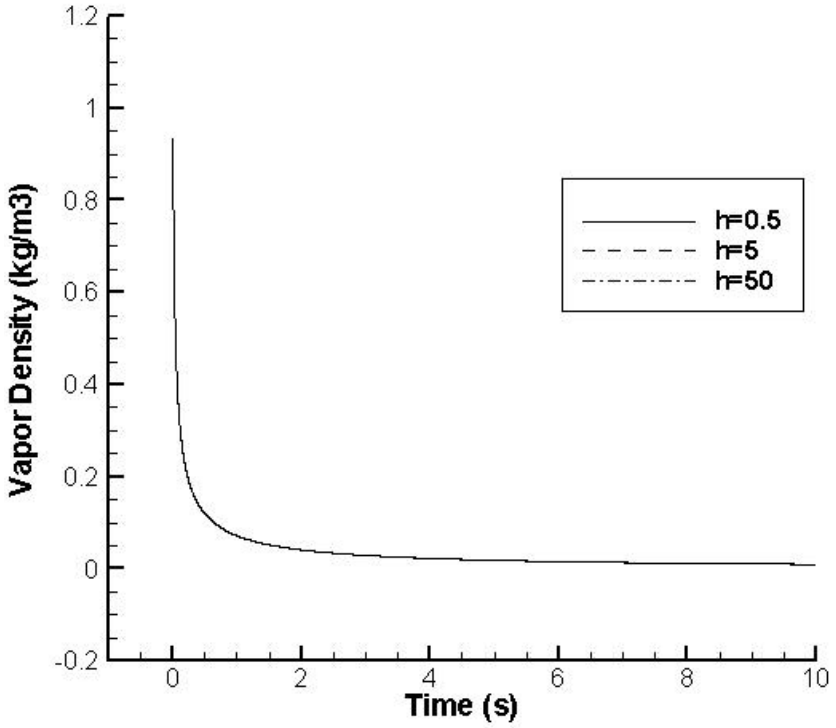

(c) Vapor Density Variation with Time at Different h

Fig. 4.4 Effect of Heat Transfer Coefficient Inside

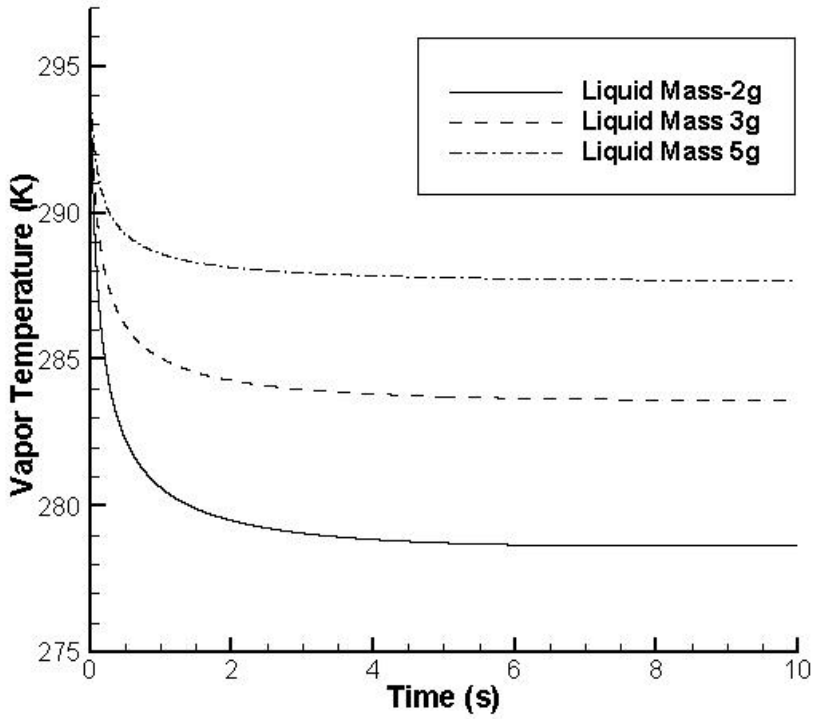

(a) Vapor Temperature Variation with Time at Different m_l

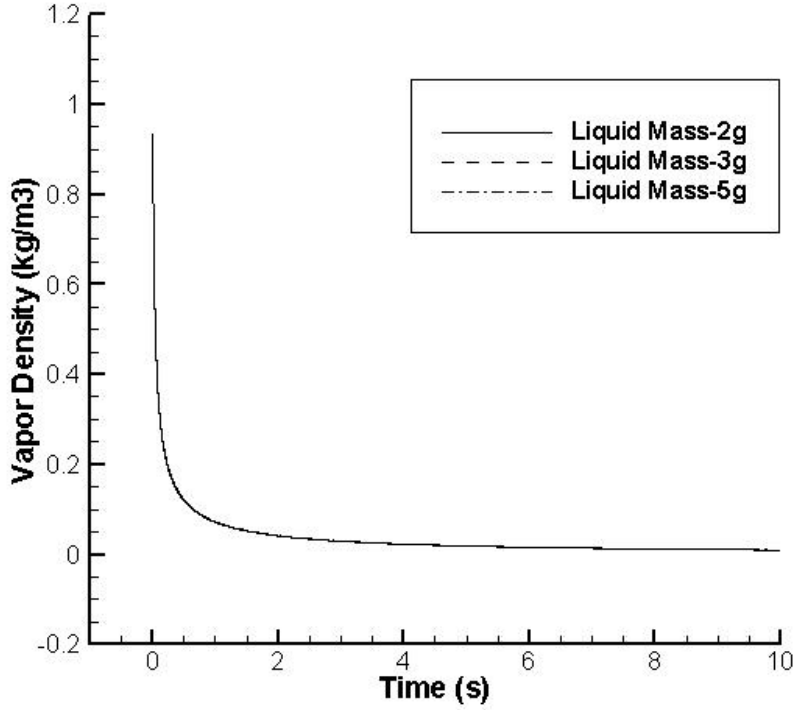

(b) Vapor Density Variation with Time at Different m_l

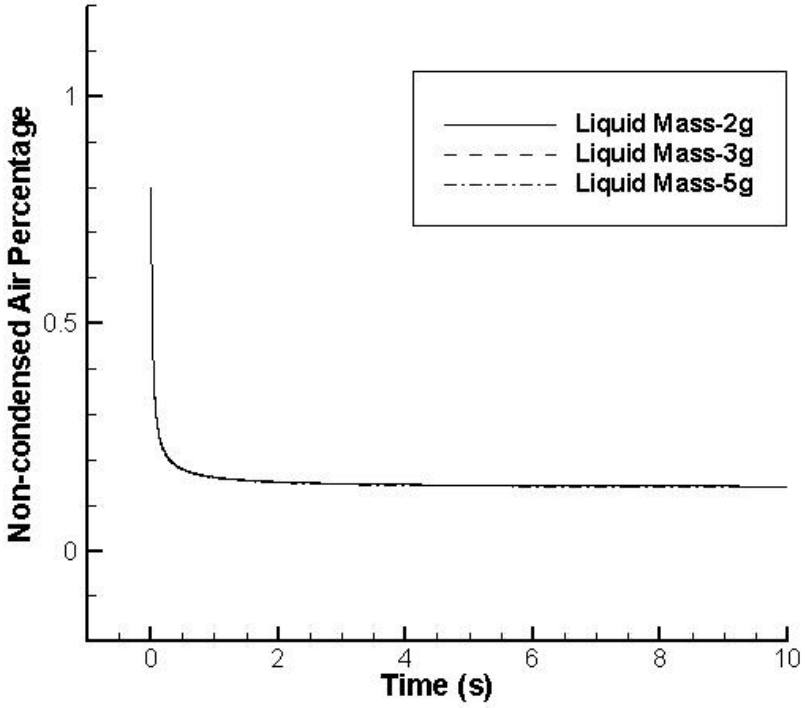

(c) Non-condensed gas Percentage Variation with Time at Different m_l

Fig. 4.5 Effect of Initial Value of Charging Liquid Mass

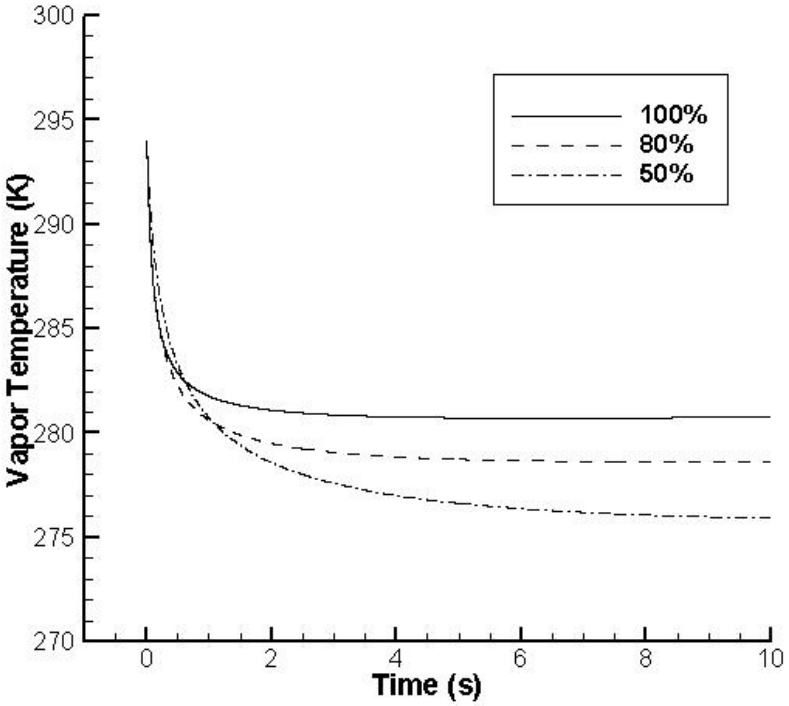

(a) Vapor Temperature Variation with Time at Different *x*

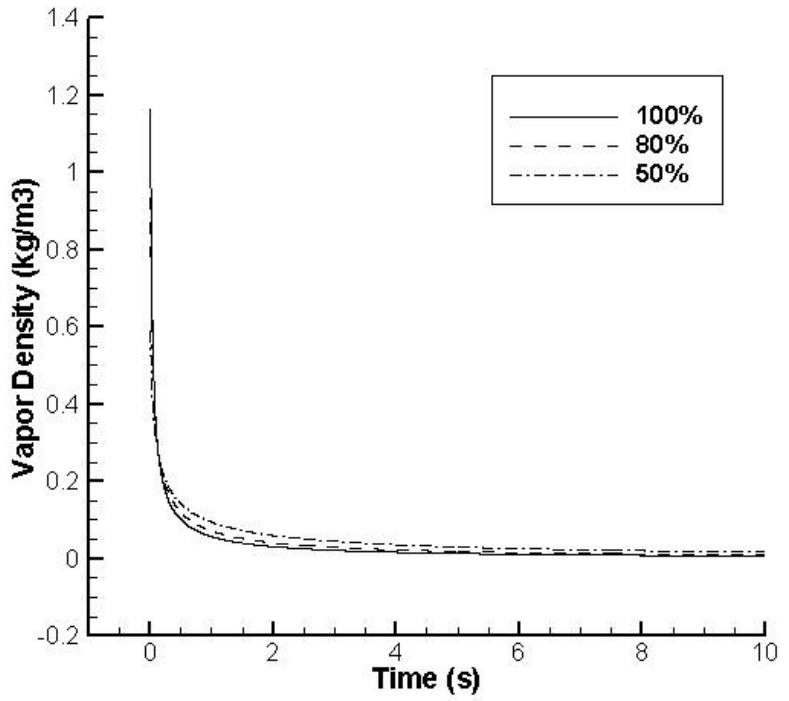

(b) Vapor Density Variation with Time at Different *x*

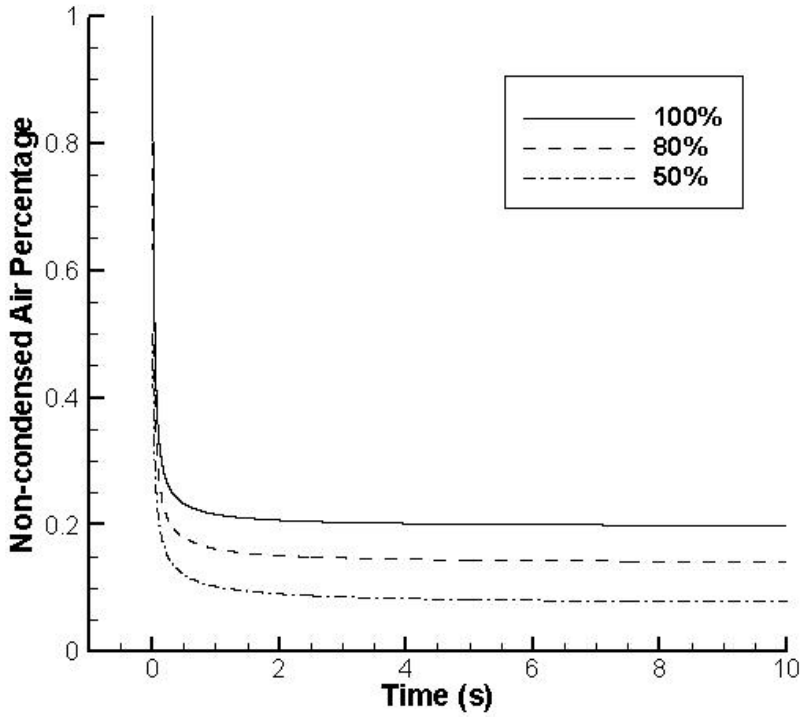

(c) Non-condensed gas Percentage Variation with Time at Different *x*

Fig. 4.6 Effect of Initial Value of Non-condensed gas Percentage

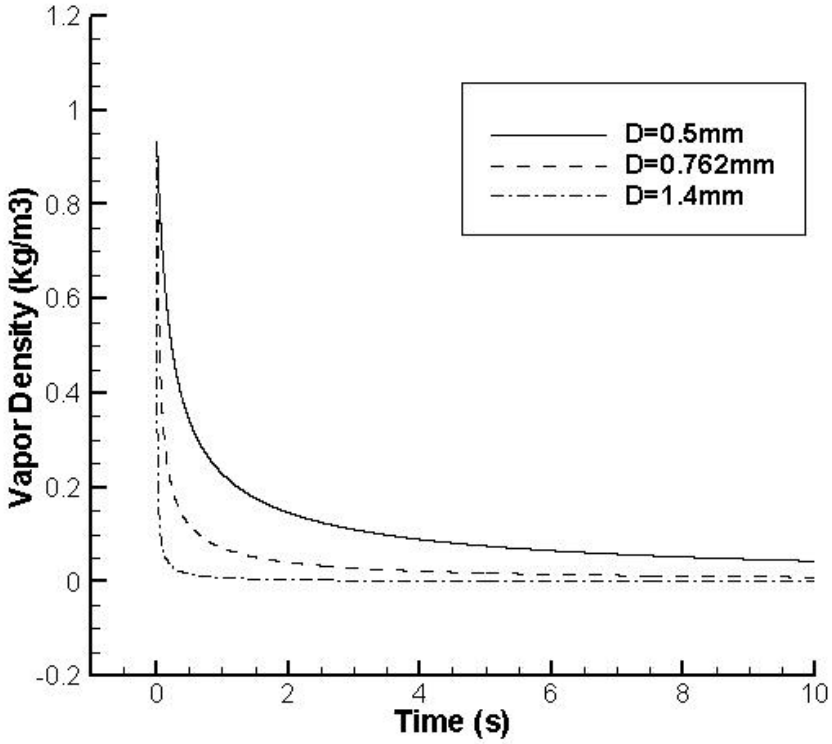

(a) Vapor Density Variation with Time at Different *D*

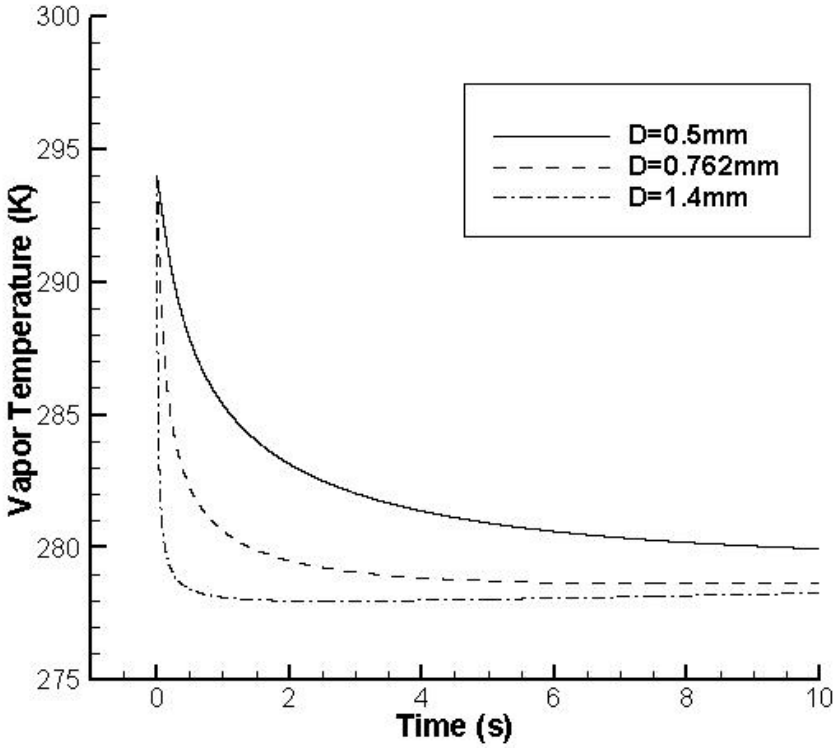

(b) Vapor Temperature Variation with Time at Different *D*

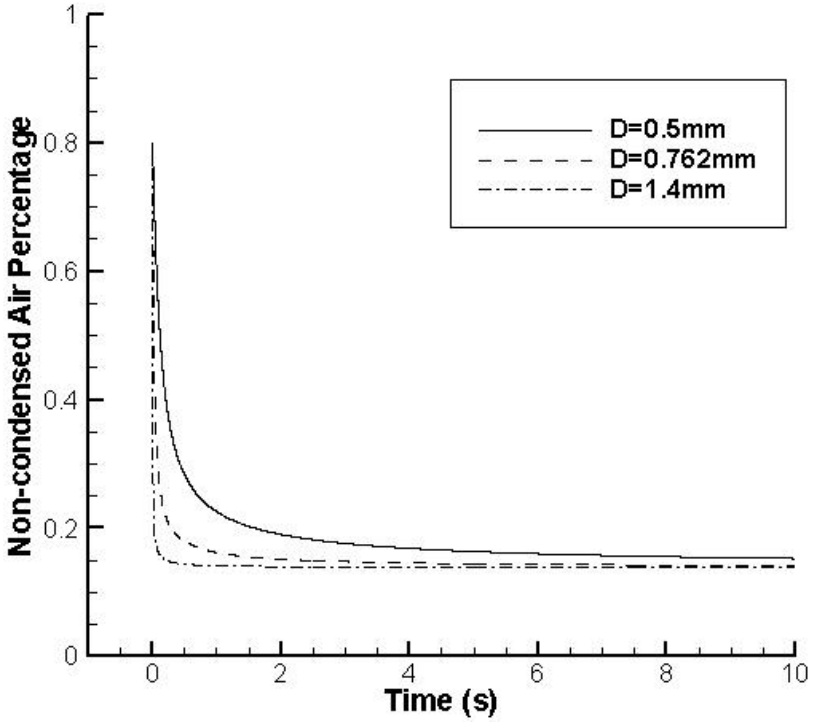

(c) Non-condensed gas Percentage Variation with Time at Different *D*

Fig. 4.7 Effect of Diameter of Charging Tubing

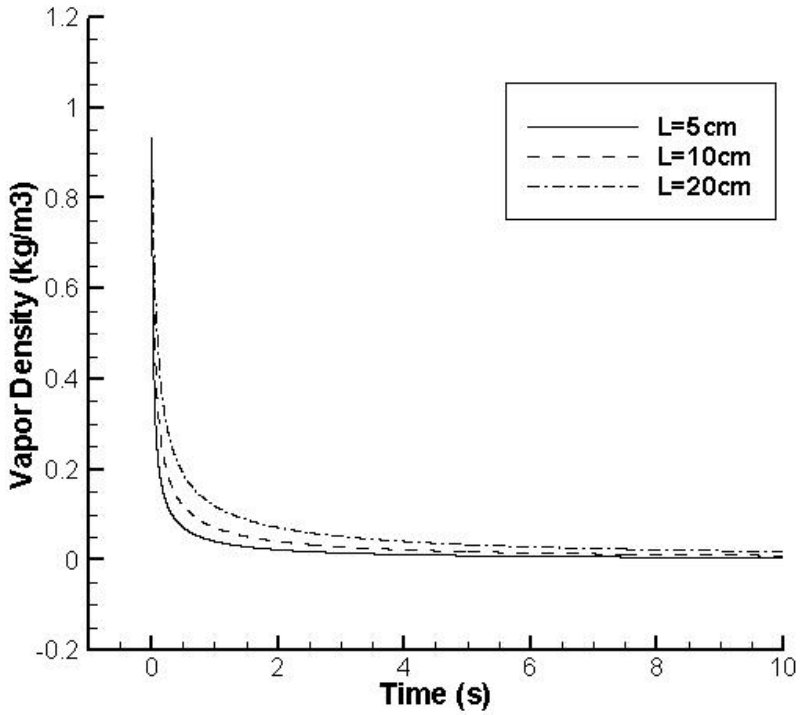

(a) Vapor Density Variation with Time at Different *L*

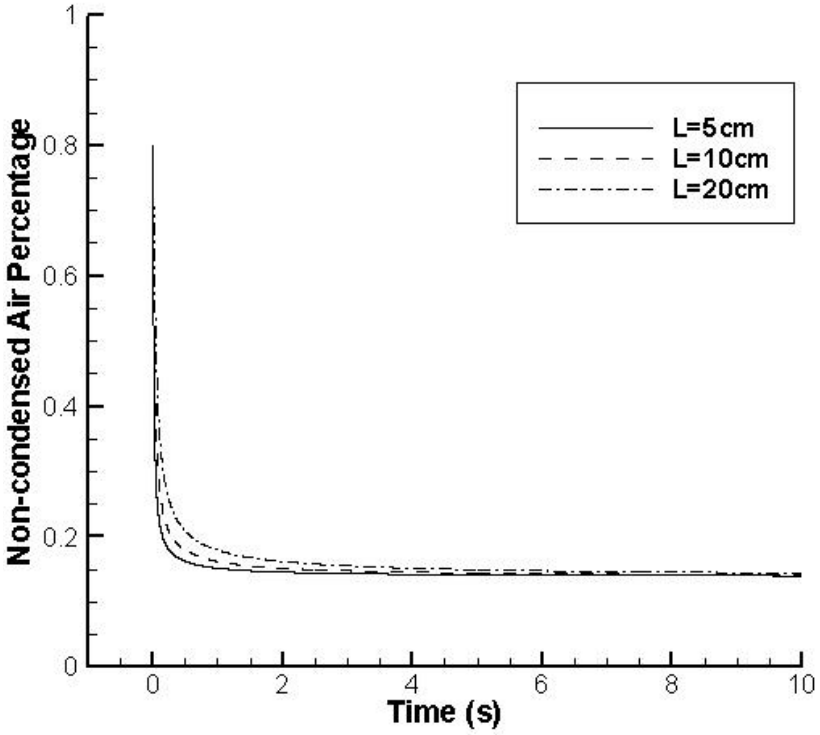

(b) Non-condensed gas Percentage Variation with Time at Different *L*

Fig. 4.8 Effect of Length of Charging Tubing

4.2 Property of sintered particle wick

Sintered particle wick has been widely used in the high heat flux heat pipes [51-53]. Researchers have developed a number of theoretical models to determine the porosity of sintered particles. This property depends on the particle shape, particle size, surface condition, and packing method [54]. The boundary condition and metallurgy process could also determine this property. To simplify the problem, many researchers [55-58] have only focused on the loose packing spherical particles with either one uniform or two different radii. One typical approach is using the high-speed computer and statistical physics to simulate the particle system [56-58]. In addition to the porosity, another important parameter for a heat pipe is the minimum meniscus radius. While the minimum meniscus radius is directly related to the porosity, this property occurring in the sintered particles has not been extensively studied. A number of heat pipe textbooks [52, 53, and 59] have indicated that this property for the sintered particles with a uniform size is equal to 0.41r, where r is the particle radius. All of these heat pipe textbooks cited the reference written by Ferell and Alleavitch [60], who actually did not conduct the investigation, and they cited it from Luikov's work [61]. And Luikov found this value using uniform spherical particles and the radius of a circle inscribed among four adjacent particles [61]. Clearly, it is necessary to conduct an investigation to determine the minimum meniscus radius occurring in the sintered particles.

The current investigation will develop a mathematical model to predict the

minimum meniscus radius of sintered particles. When the system consists of, in particular, mixed particles with different radii, it makes the distribution of particles very complicated. This paper analyzes the possible structures in the uniform spherical particle system to obtain the minimum meniscus radius for this case. Then using this information, a mathematical expression of minimum meniscus radius for mixed particles is presented.

When heat is applied to the evaporating region of a heat pipe, the heat will travel through the solid wall of the container to reach the working fluid. Provided that the heat pipe has not reached the boiling limit, heat will pass through the sintered particles saturated with working fluid and reach the top surface of the working fluid in the wick. The heat will then pass through a thin-film region consisting of three regions: the non-evaporating thin film region, the evaporating thin film region, and the meniscus thin film region [51]. The evaporation in the thin film region makes the liquid-vapor interface recede into the sintered particles. When the heat input in the evaporator increases, the liquid-vapor interface will further recede into and make the meniscus radius become smaller. The decrease in the meniscus radius increases the capillary pressure to overcome the increase of pressure drop occurring in the flow path of working fluid. When the increase of heat input has resulted in a minimum meniscus radius, the heat pipe has reached the capillary limit. Clearly, the minimum meniscus radius is a key in designing a high-heat flux heat pipe.

If heat is added to the sintered porous medium fabricated from the perfectly

spherical particles, the heat is transferred through the sintered particles filled with the working fluid, reaching the top surface where the liquid-vapor-solid interface exists. There, by utilizing the thin film evaporation, the heat is removed. In order to avoid the boiling limit, the thickness of sintered particles in the evaporating section is very thin, in particular, for a high heat flux heat pipe [51]. Clearly, the meniscus radius variation occurring in the top layer of sintered particles will be directly related to the heat transport through the heat pipe. And the minimum meniscus radius occurring in the top layer of sintered particles will determine the maximum capillary heat transport capability of a heat pipe. The minimum meniscus radius is directly related to the maximum capillary pressure, i.e.,

$$\Delta p_{c,\max} = \frac{2\sigma}{r_{c,e}} \tag{4-15}$$

The minimum meniscus radius, $r_{c,e}$, in Eq. is defined by

$$r_{c,e} = \frac{2A_{gap}}{P_{gap}} \tag{4-16}$$

where A_{gap} is the minimum area trapped by particles and P_{gap} perimeter of the trapped area.

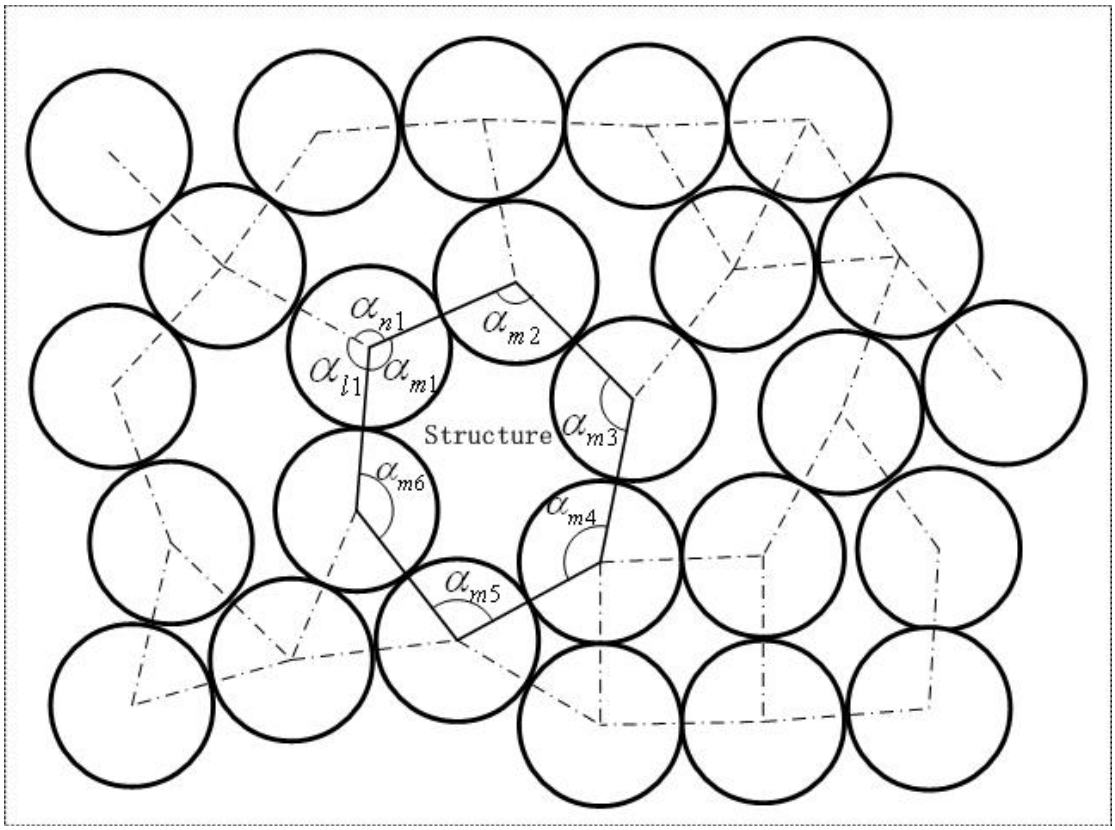

Fig. 4.9 Structures in the particles layer

To simplify the problem, two assumptions are made, i.e.: 1) the whole system is in a stable state; and 2) the particles are spherical. In the stage of pouring particles, the system of these particles (as shown in Fig. 4.9) may be unstable and the properties will be different from those in a stable system. During the transition from the unstable system to the stable system, symmetric structures need more energy to have a new structure because the symmetric structures obtained the maximum energy during the pouring process. In other words, once the symmetric structures during the pouring process are formed, it is not easy to be re-structured during the sintering process. Based on this assumption, only symmetric structures shown in Fig. 4.10 are formed. The second assumption is related to the shape of sintered particles. When the

particles are sintered, they would be combined or “melt” into each other by the diffusion and their shapes are not perfectly spherical any more. This might result in the variation of relative positions of these particles.

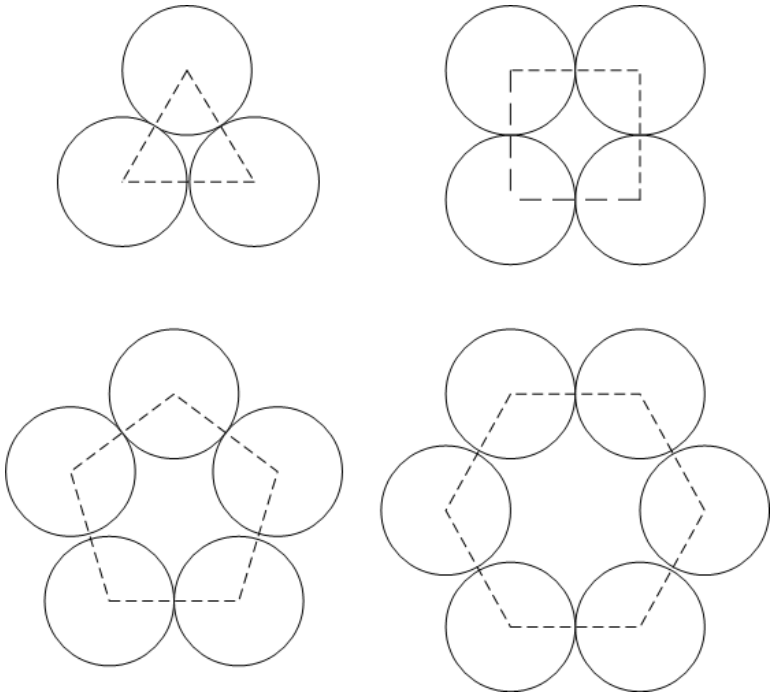

Fig. 4.10 Some stable structures

For a structure to be stable, the following conditions should be satisfied, i.e. :

$$\sum_{x=1}^{N} \alpha_{mx} = (N-2)\pi \tag{4-17}$$

$$\sum_{y=1}^{M} \alpha_{yx} = 2\pi \tag{4-18}$$

where Eq. (4-17) comes from one structure and Eq. (4-18) from one particle. If all particles are uniform and have a same radius, it is found that not all of the symmetric structures satisfy the requirements shown in Eqs. (4-17) and (4-18), and only the triangular, rectangular and hexagonal structures could exist in the system. Therefore,

it can be concluded that the sintered particles investigated here consist of only these three structures. By viewing from one particle, there would be several structures formed around this particle as shown in Fig. 4.11. List all possible arrangements of these structures and consider that each group of those structures has the same possibility. Then the percentage of each structure could be determined. Use A, B, C to represent triangular, rectangular and hexagonal structure, respectively. Table 4.1 lists all the possible groups of structures and the number of arrangements for each group. From Table 4.1, it could be found that the percentages for the triangular, rectangular, and hexagonal structure is 45%, 28%, and 27%, respectively. Using Eq. (4-16) the minimum meniscus radii for these structures can be found as 0.103r, 0.273r and 0.654r, for the triangular, rectangular, and hexagonal structure, respectively. The average minimum meniscus for the sintered particles with a uniform radius can be found by

$$r_{c,e} = 2\frac{A_{gap,A}\cdot 45\% + A_{gap,B}\cdot 28\% + A_{gap,C}\cdot 27\%}{P_{gap,A}\cdot 45\% + P_{gap,B}\cdot 28\% + P_{gap,C}\cdot 27\%} = 0.443r \qquad (4\text{-}19)$$

where r is the particle radius. The minimum meniscus radius of 0.443r derived here agrees well with the one derived by Ferrell and Alleavitch [60], which has been accepted by all heat pipe textbooks [52, 53, 59].

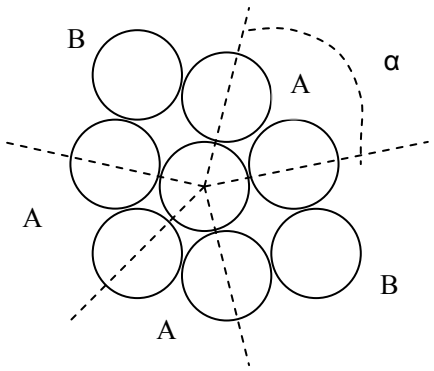

Fig. 4.11 Angles and structures around on single particle

Table 4.1. Possible groups and arrangements.

Group	6A	4B	3C	3A+2B	2A+2C	4A+1C	1A+2B+1C	Total
Arrangement	1	1	1	2	2	1	2	10

If the size of sintered particles is not uniform, the method described above obviously cannot be used to predict the minimum meniscus radius. To solve this problem, draw a long enough line linking any two particles, as shown in Fig. 4.12. The line will pass through all of the possible structures, which could be represented by the angles and their relative edges (consisting of the radius of two neighboring particles). This can transform the 2-D problem into a 1-D.

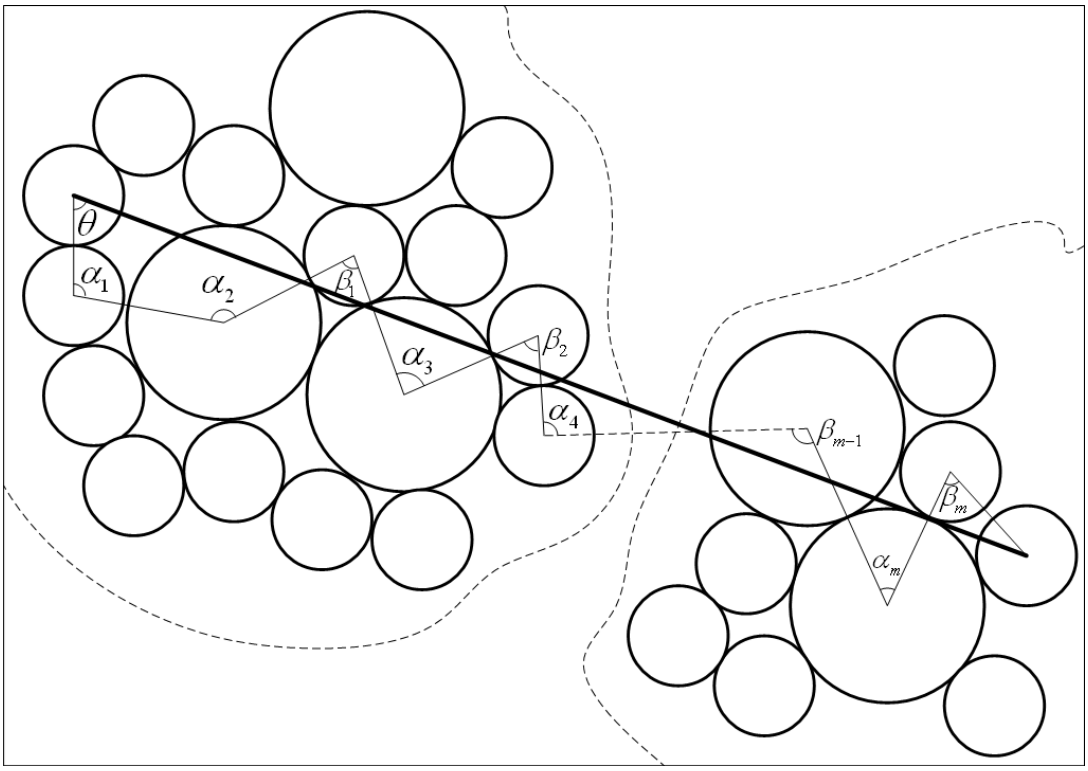

Fig. 4.12 Lines and angles on the one layer of mixed particles

Considering such a “long enough” line, it could be found that the number of particles along it is determined by the structures. More structures need more particles to present. The straight line starts from the center of one particle in one structure and ends at the center of one particle in another structure. The angle θ between the long enough line and the center connecting line of the first two particles, as shown in Fig. 4.12, is called start angle, which would also influence the number of the particles along the long enough line. However, the start angle and structures are individual to each other. With the variation of start angle, there exists a minimum number, N_0 particles near the long enough line, which is directly determined by the structures and could be used to represent the structures. Hence, the number of particles along a long

enough line, function of start angle θ and N_0, could be expressed as:

$$N = F(N_0, \theta) = f(\theta) N_0 \tag{4-20}$$

In Fig. 4.12 there is another twist line connecting the center of particles which are closest to the straight line. As discussed above, this twist line contains all of the possible angles and edges of structures with their percentage. It is noticed that there are some angles turn the line upward and the others turn the line downward relatively to the straight line. Discriminate these two kinds of angles by α_1, α_2, α_3, …, α_{l-1}, α_l for turning upward, and β_1, β_2, β_3, …, β_{m-1}, β_m for turning downward.

The total length of the straight line can be found as

$$\begin{aligned} L &= \sum_{n=1}^{N} \left[R_0 \cos\theta + R_n \cos\left(\theta - \sum \alpha_l + \sum \beta_m\right) \right] \\ &= \sqrt{M_1^2 + M_2^2} \cos(\theta + \varphi) \end{aligned} \tag{4-21}$$

where

$$M_1 = R_0 + \sum_{n=1}^{N} \left[R_n \cos\left(-\sum \alpha_l + \sum \beta_m\right) \right] \tag{4-22}$$

$$M_2 = \sum_{n=1}^{N} \left[R_n \sin\left(-\sum \alpha_l + \sum \beta_m\right) \right] \tag{4-23}$$

$$\begin{aligned} \cos\varphi &= M_1 / \sqrt{M_1^2 + M_2^2} \\ \sin\varphi &= M_2 / \sqrt{M_1^2 + M_2^2} \end{aligned} \tag{4-24}$$

Considering Eq. (4-20), the length of the straight line could be expressed as

$$L = \sqrt{f(\theta) N_0 \left[\sum X_i R_i^2 + g(R, \alpha, \beta) / N \right]} \cos(\theta + \varphi) \tag{4-25}$$

where $g(R, \alpha, \beta)$, sum of $N(N-1)$ terms, is function of edges and angles.

Imaging one layer of particles placing on a large rectangle surface and each side long enough, the area of the minimum gaps trapped by particles is equal to the difference

between the rectangle area and the total area of all of the particles. The total length of perimeters of all the minimum gaps trapped by particles in the rectangle is equal to the total length of perimeters of all the particles. The minimum meniscus radius can be found as

$$r_{c,e} = 2A_{gap} / P_{gap} = \frac{L_1 L_2 - \pi N_0^2 f(\theta) f\left(\pi/2-\theta\right) \sum\left(Y_j r_j^2\right)}{\pi N_0^2 f(\theta) f\left(\pi/2-\theta\right) \sum\left(Y_j r_j\right)} \qquad (4\text{-}26)$$

Equation (4-26) can be used to calculate the minimum meniscus radius occurring in the sintered particles with different radii.

For example, when the sintered particles consist of two kinds of particles with diameters of 100 μm and 50 μm, respectively, with these given particle sizes, the total length of straight line could be simplified as

$$L \approx kf\left(\theta\right) N_0 \sqrt{\sum X_i R_i^2} \qquad (4\text{-}27)$$

where the constant k considers the angle effect. Then Eq. (4.26) can be expressed as

$$r_{c,e} = \frac{k^2 \sum\left(X_i R_i^2\right) - \pi \sum\left(Y_j r_j^2\right)}{\pi \sum\left(Y_j r_j\right)} \qquad (4\text{-}28)$$

The constant k can be determined from the sintered particles with the uniform size, which can be found as

$$k^2 = 1.1333 \qquad (4\text{-}29)$$

Figure 4.13 illustrates the minimum meniscus radius variation for mixed particles with diameters of 100 μm and 50 μm. As shown, the predicted minimum meniscus radius is smaller to the average one, which has been demonstrated in a heat pipe with sintered mixed particles.

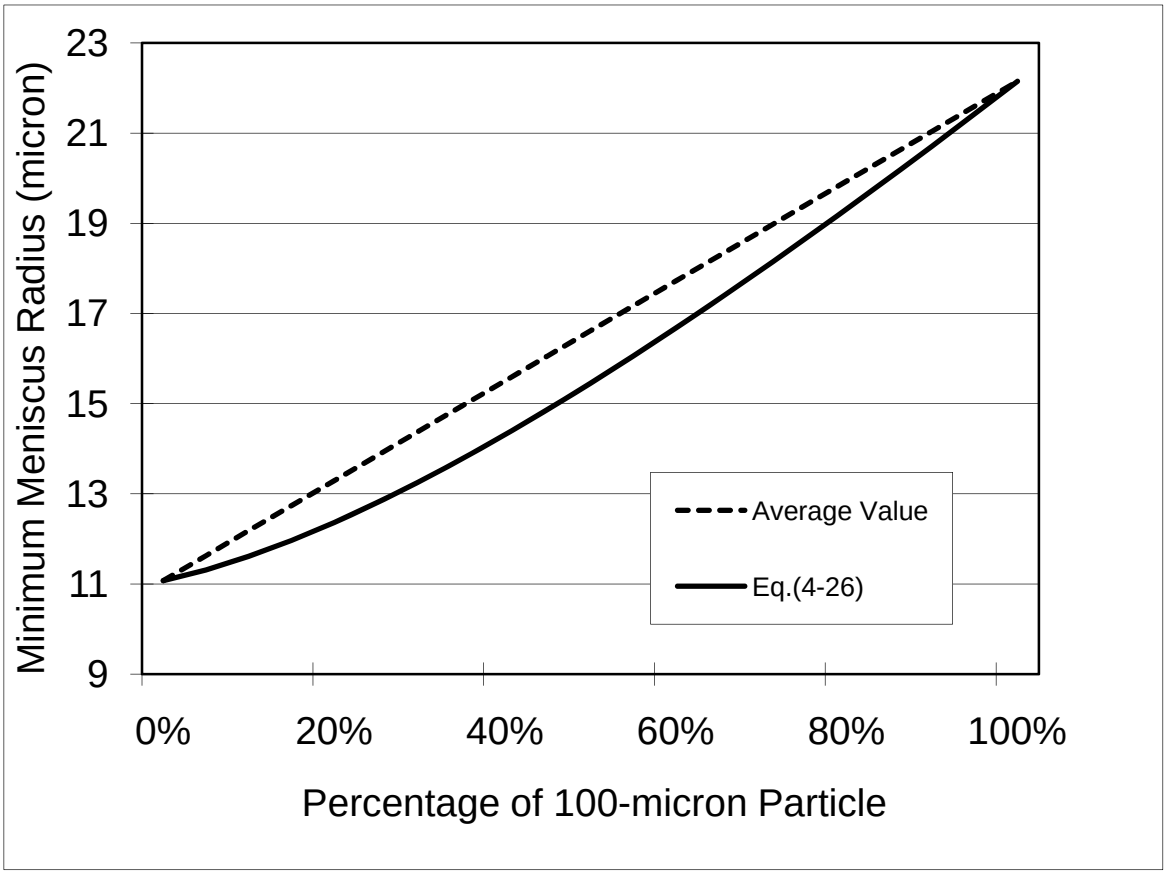

Fig. 4.13. Minimum meniscus radius predicted by Eq.(4-26)

4.3 Application of sintered particles wick structure in prediction of vapor chamber

Based on the statistical analysis of particle distribution, a theoretical model predicting the effective thickness of sintered wick structure is developed including the effect of the wick structure on its thermal resistance. The model can be used to predict the heat flux effect on the thermal resistance occurring in the sintered particles in the evaporator. The theoretical results show that the pore size is non-uniformly

distributed in the wick due to the particle structure arrangements. Liquid in the wick structures with larger pore sizes will recede and dry out first as the heat transfer rate increases. The model was used in the prediction of vapor chamber performance conducted by J. Chang etc. [63], as shown in Fig. 4.14. The chip contains three metallic heaters: a 10 × 12 mm heater in order to provide uniform heating, a 10 × 3 mm heater in order to simulate a localized heating, and a 400 × 400 μm heater in order to simulate the hot spots on actual microprocessors. In the experiment, the highest heat flux from the hotspot heater was approximately 690 W/cm^2. The comparison indicates that the theoretical results predicted by the current model (considering wick structures) are more consistent with experimental results than that by the previous models (without considering wick structures). The theoretical analysis will assist in optimizing the heat transfer performance of sintered wicks in heat pipes and result in a better understanding of mechanisms of heat transfer and fluid flow in the sintered particles.

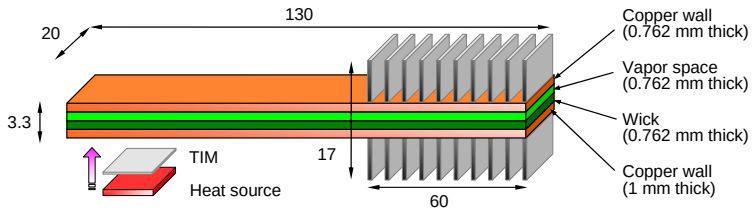

Fig. 4.14. Schematic of vapor chamber[63]

In order to predict the temperature drop occurring in the vapor chamber, the thermal resistances occurring in the evaporator and condenser must be determined. When heat is added on the evaporating section, heat is transferred from the heat pipe

shell through the wick saturated with the working fluid to the liquid-vapor-solid interface, where the thin film evaporation occurs. The vapor flows from the evaporator through the adiabatic section to the condensing section, where the vapor condenses into the condensate and releases the latent heat. The heat is transferred from the condensation film through the wicks saturated with the condensate to the heat pipe shell, where the heat is removed by the liquid cooling or forced convection of air flow. During this heat transfer process, the thermal resistance in the wick plays an important role in determining the total temperature drop in the heat pipe, in particular, for a high heat flux application.

When the heat transfer rate added on the heat pipe is increased, the mass flow rate of working fluid in the flow path increases, which directly results in the increase of the total pressure drop. In order to overcome the pressure drop, the driving pressure occurring in the wick must increase. The increase of the capillary pressure directly is related to the meniscus radius of liquid-vapor interface in the sintered wicks. The capillary pressure occurring in the heat pipe can be expressed as:

$$\Delta p_{cap} = 2\sigma\left(\frac{1}{r_e} - \frac{1}{r_c}\right) \tag{4-30}$$

Where r_e and r_c are the meniscus radii at the liquid-vapor interface in the evaporator and condenser, respectively. For the vapor chamber investigated herein, r_c can be assumed to be equal to infinity. The capillary pressure in the heat pipe will only depend on the meniscus radius of the sintered wick in the evaporator. As revealed in previous sections, if the wick consists of sintered particles with a uniform radius, the

possible arrangements formed in the wick are triangular, rectangular, and hexagonal structures. The percentage of each structure could be determined that the percentages for these three structures are 45%, 28%, and 27%, respectively. The minimum meniscus radii for these structures can be found as 0.103r, 0.273r and 0.654r, for the triangular, rectangular, and hexagonal structure, respectively.

With the increase of input heat, liquid in these structures begin to recede for smaller meniscus radius. The fact is that there are many kinds of structures with different pore sizes in the wick. Hence when the input heat becomes large enough, the liquid in some structures cannot be held any more and recede to the wick structure with smaller pore sizes. There are two factors determining the thermal resistance of the wick: one is the expanded liquid-vapor interface; another is the significantly decreased effective thickness of liquid. Because the thermal resistance at the expanded liquid-vapor-solid interfaces due to the thin film evaporation is much smaller than the thermal resistance of wicks saturated with working fluid, the thermal resistance in the wick can be approximately determined by the effective thickness of wicks saturated with working fluid, i.e.,

$$R = \frac{\delta_{eff}}{k_{eff}} \tag{4-31}$$

where δ_{eff} is the effective thickness of wick saturated with working fluid depending on the heat flux level. The effective thermal conductivity, k_{eff}, can be determined by:

$$k_{eff} = k_s \left(\frac{2 + k_l / k_s - 2\varepsilon\left(1 - k_l / k_s\right)}{2 + k_l / k_s + \varepsilon\left(1 - k_l / k_s\right)} \right) \tag{4-32}$$

where k_s and k_l are the thermal conductivities of solid and liquid phases, respectively. The wick porosity, ε, in Eq. (4-32) is defined as the ratio of the pore volume V_{por} to the total volume V_{tot} of wick structure.

When the heat transfer rate added on the heat pipe is zero, the liquid level in the evaporator would not recede into the wick, the effective thickness of wick, δ_{eff}, is equal to the total thickness of the wick, δ, in the evaporator, as shown in Fig. 4.15(a). When the heat transfer rate added on the evaporator increases, the liquid level recedes into the wick to produce the meniscus radius and the capillary pressure to overcome the liquid pressure drop occurring in the flow path, i.e.,

$$\Delta p_{cap} = \Delta p_l + \Delta p_v + \Delta p_g \tag{4-33}$$

The pumping head due to the capillary pressure, Δp_{cap}, can be determined by Eq. (4-30). The liquid pressure drop, Δp_l, is the result of the combined effect of both viscous and inertial forces. If the flow rate in the wick is very small, the effect of inertial force can be neglected, and the pressure difference in the liquid phase is caused only by the frictional forces at the liquid-solid interface and the liquid-vapor interface due to the vapor flow effect. The total liquid pressure drop can be determined by integrating the pressure gradient over the length of the flow passage, or,

$$\Delta p_l(x) = -\int_0^x \frac{dp_l}{dx} dx \tag{4-34}$$

where the limits of integration are from the evaporator end (x=0) to the condenser end (x=L), and dp_l/dx is the gradient of the liquid pressure resulting from the frictional

forces from the solid wick, wall, and vapor flow at the liquid-vapor interface, which can be written as

$$\frac{dp_l}{dx} = \left(\frac{\mu_l}{KA_w \rho_l} \right) \dot{m}_l \tag{4-35}$$

where $\dot{m}_l$ is the local mass flow rate in the wick, and *K*, the permeability for the sintered particles, can be expressed as:

$$K = \frac{d_s^2 \varepsilon^3}{37.5(1-\varepsilon)^2} \tag{4-36}$$

where d_s is the average diameter of the sintered particles. For uniform heat addition and rejection, Eq. (4-33) can be expressed as

$$\Delta p_l = \left(\frac{\mu_l}{KA_w h_{fg} \rho_l} \right) L_{eff} q \tag{4-37}$$

where $q = \dot{m}_l h_{fg}$ and the effective heat pipe length can be found as

$$L_{eff} = 0.5L_e + L_a + 0.5L_c \tag{4-38}$$

If the heat pipe is charged with an appropriate amount of working fluid and the wetting point occurs at the cap end of condenser, the vapor pressure drop can be calculated by the approach recommended by Peterson [1] and Dunn and Ready [64] Based on the one-dimensional vapor flow approximation, the vapor pressure drop can be determined by

$$\Delta p_v = \left(\frac{C(f_v \cdot \mathrm{Re}_v)\mu_v}{2r_{h,v}^2 A_v \rho_v h_{fg}} \right) L_{eff} q \tag{4-39}$$

where *C* is the constant that depends on the Mach number defined by

$$Ma_v = \frac{q}{A_v \rho_v h_{fg} (R_v T_v \gamma_v)^{1/2}} \tag{4-40}$$

The ratio of specific heats, γ_v, in Eq. (4-40) depends on the molecule types, which is equal to 1.67, 1.4, and 1.33 for monatomic, diatomic, and polyatomic molecules, respectively. Previous investigation summarized by Peterson [1] have demonstrated that the friction factor Reynolds number product, $f_v \cdot \mathrm{Re}_v$, and the constant, C, shown in Eq. (4-39) can be determined by

$$\begin{aligned} &\mathrm{Re}_v < 2300 \quad and \quad Ma_v < 0.2 \\ &f_v \cdot \mathrm{Re}_v = \text{constant}, \quad C=1.0 \end{aligned} \tag{4-41}$$

$$\begin{aligned} &\mathrm{Re}_v < 2300 \quad and \quad Ma_v > 0.2 \\ &f_v \cdot \mathrm{Re}_v = \text{constant}, \quad C=\left[1+\left(\frac{\gamma_v - 1}{2}\right) Ma_v^2\right]^{-1/2} \end{aligned} \tag{4-42}$$

$$\begin{aligned} &\mathrm{Re}_v > 2300 \quad and \quad Ma_v < 0.2 \\ &f_v \cdot \mathrm{Re}_v = 0.038\left(\frac{2r_{h,v}q}{A_v \mu_v h_{fg}}\right)^{3/4}, \quad C=1.0 \end{aligned} \tag{4-43}$$

Because the equations used to evaluate both the Reynolds number and the Mach number are functions of the heat transport capacity, it is first necessary to assume the conditions of the vapor flow, and an iterative procedure must be used to determine the vapor pressure.

As the heat transfer rate increases, the meniscus radius decreases, which can be determined by Eqs. (4-30, 33, 37 and 39). If the determined meniscus radius is between ∞ and 0.654r occurring in the wick, the receding of liquid level will occur in the relatively larger pores, i.e., in the hexagonal structure. When the heat transfer rate further increases, the wick structure with larger pores cannot hold liquid and the wick structure with larger pores such as hexagonal structures will dry out, as shown in Fig. 4.15(b). When this situation occurs, the thermal resistance in the wick will consist

of those occurring in the rectangular and triangular structures saturated with liquid because the vapor generated at the liquid-vapor interface can be easily escaped from the opened hexagonal structures shown in Fig. 4.15(b). The thermal resistance can be expressed as

$$R = \frac{\delta_{eff,\square+\Delta}}{K_{eff}} \tag{4-44}$$

where $\delta_{eff,\square+\Delta}$ is the effective thickness of the wick consisting of the rectangular and triangular structures saturated with liquid, which can be found by the percentages of the wick structures, i.e.:

$$\delta_{eff,\square+\Delta} = 0.73\,\delta \tag{4-45}$$

When the heat transfer rate added on the heat pipe continues to increase, the liquid level will recede into the wick within relatively smaller pores. If the meniscus radius is smaller than 0.654r, which is corresponding to the situation shown in Fig. 4.15(b), the liquid-vapor interface will vary in those wicks with rectangular structures. When the heat transfer rate is higher than that corresponding to the meniscus radius of 0.273r, as shown in Fig. 4.15(c), the wick structure with the rectangular structures cannot hold the liquid and will dry out. If this situation occurs, the thermal resistance in the wick will be primarily from the triangular structures saturated with liquid because the vapor generated at the liquid-vapor interface can be easily escaped from the opened hexagonal and rectangular structures shown in Fig. 4.15(c). The thermal resistance can be expressed as

$$R = \frac{\delta_{eff,\Delta}}{k_{eff}} \tag{4-46}$$

where $\delta_{eff,\Delta}$ is the effective thickness of the wick consisting of the triangular structures saturated with liquid, which can be found by the percentages of the wick structures, i.e.:

$$\delta_{eff,\Delta} = 0.45\,\delta \tag{4-47}$$

If the heat transfer rate added on the heat pipe further increases, the liquid-vapor interface will further recede and the meniscus radius becomes smaller and is between 0.273r and 0.103r, which is in the range of the pore size of the triangular structure. When the heat transfer rate is higher than that corresponding to the minimum meniscus radius of 0.103r, the whole heat pipe will dry out and reaches the capillary limitation.

Clearly, the thermal resistance in the wicks in the evaporator is directly dependent on the heat transfer rate, which determines the meniscus radius variation and liquid distribution in the wick. For a given heat transfer rate, the meniscus radius can be calculated, and the percentage of hexagonal, rectangular, and/or triangular structures in the wick saturated with liquid obtained. The effective thickness of wicks saturated with liquid can be determined and the temperature difference across the wick in the evaporator found.

The calculation about the other parts of total thermal resistance would not be presented here. The detail is in the reference [63]. Fig. 4.16 and 4.17 present the final comparison of experimental results and predictions. And Fig. 4.17 clearly

shows that considering wick structures in the model would have a better prediction.

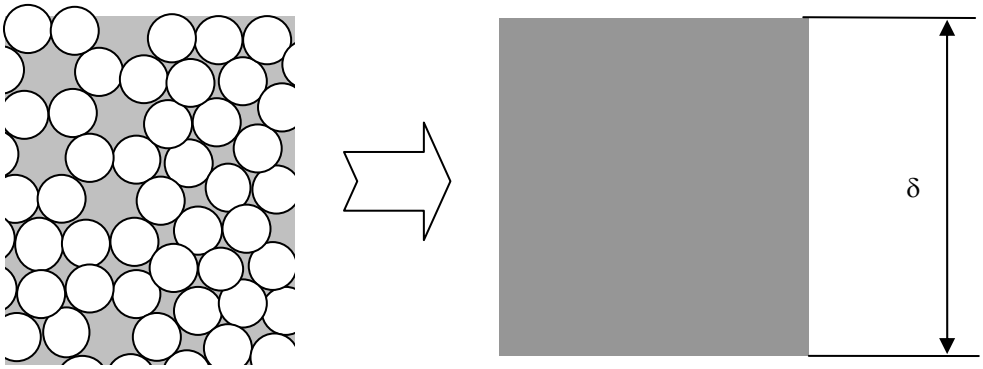

(a) wick structures saturated with liquid at a heat input of 0.0 W

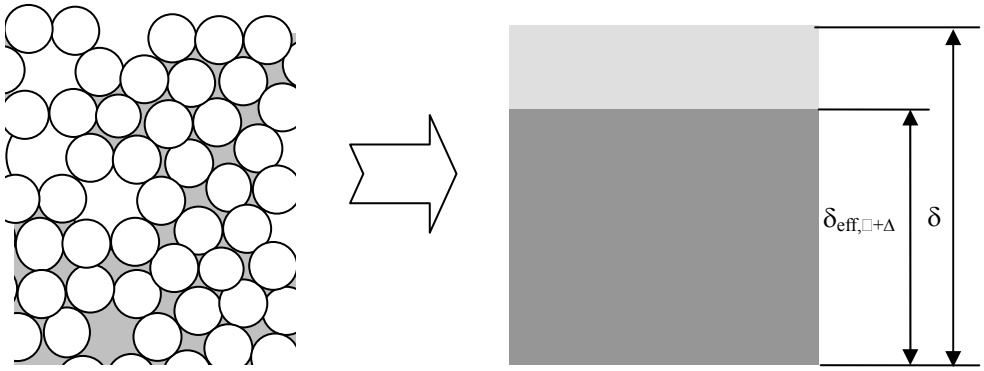

(b) as the heat transfer rate is high, larger pores held by hexagonal structures dry out and only rectangular and triangular structures saturated with liquid exist

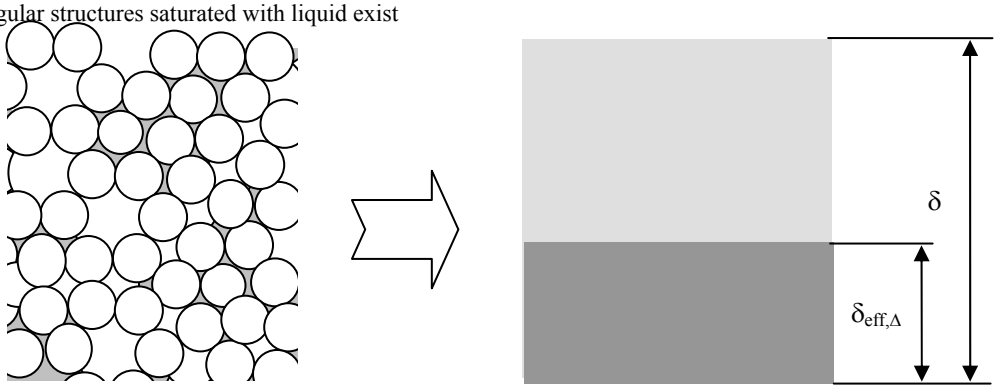

(c) as the heat transfer rate is higher, pores held by hexagonal and rectangular structures dry out and only triangular structures saturated with liquid exist

Fig. 4.15 Schematic of wick structure and effective thickness

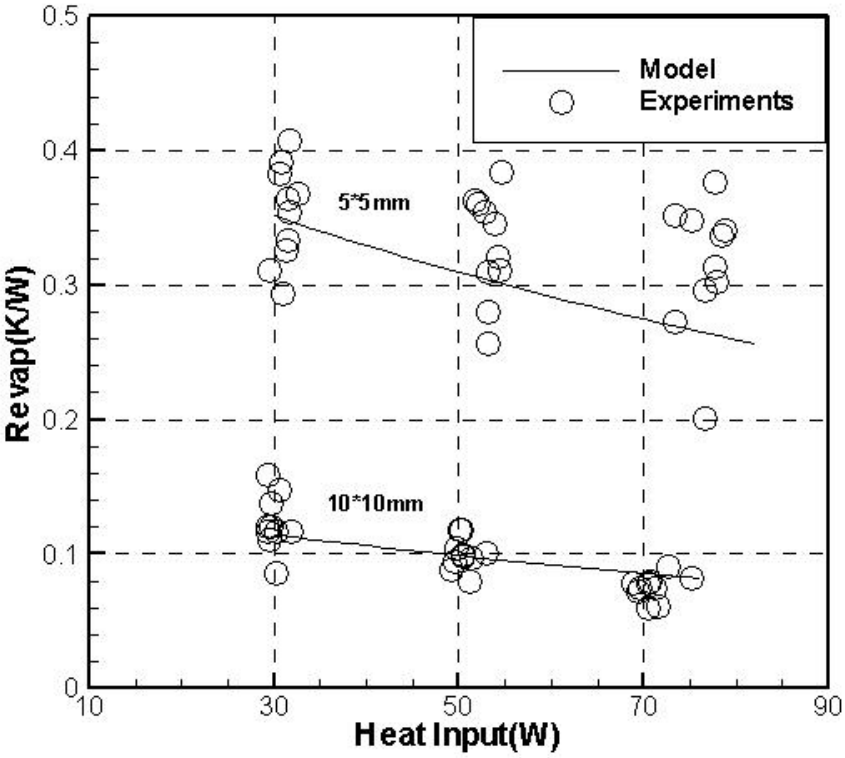

Fig. 4.16 Comparison of theoretical prediction and experimental results

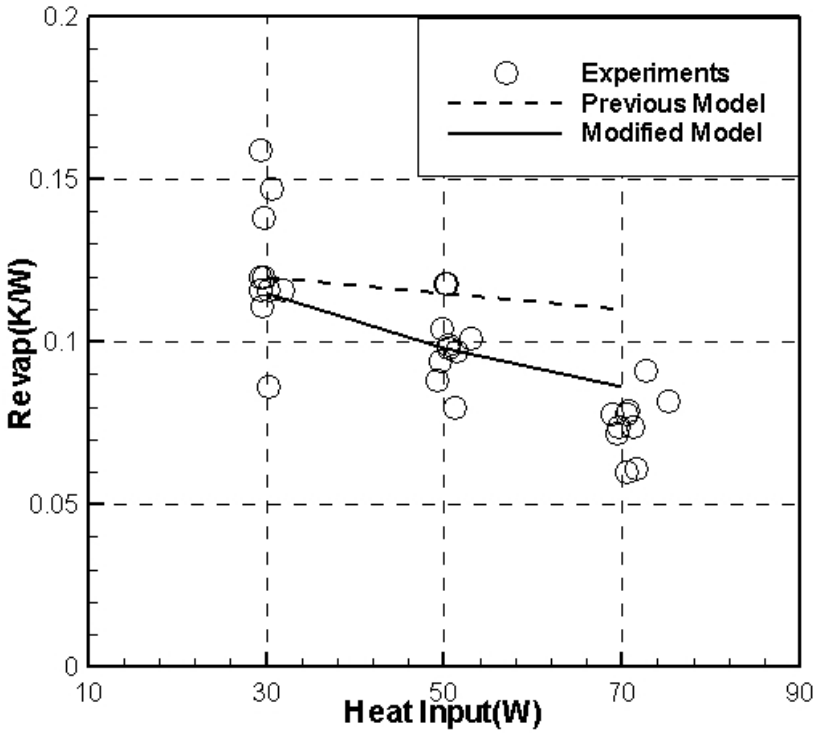

Fig. 4.17 Comparison of different model

4.4 Conclusions

A mathematical model predicting the minimum meniscus radius occurring in the sintered particles with different sizes is developed. For uniform-size particles, the minimum meniscus radius is found equal to 0.443r. When the sintered particles are mixed with different size, the minimum meniscus radius can be predicted by $r_{c,e} = 2A_{gap} / P_{gap} = \frac{k^2 \sum \left(X_i R_i^2 \right) - \pi \sum \left(Y_j r_j^2 \right)}{\pi \sum \left(Y_j r_j \right)}$. The investigation conducted here can result in a better understanding of heat transfer mechanisms occurring in a high-heat-flux heat pipe. Based on the statistical analysis of particle distribution, a theoretical model predicting the effective thickness of sintered wick structure is developed including the effect of the wick structure on its thermal resistance. The model can be used to predict the heat flux effect on the thermal resistance occurring in the sintered particles in the evaporator. The theoretical results show that the pore size is non-uniformly distributed in the wick due to the particle structure arrangements. Liquid in the wick structures with larger pore sizes will recede and dry out first as the heat transfer rate increases. The comparison indicates that the theoretical results predicted by the current model are more consistent with experimental results than that by the previous models. The theoretical analysis will assist in optimizing the heat transfer performance of sintered wicks in heat pipes and result in a better understanding of mechanisms of heat transfer and fluid flow in the sintered particles. Moreover, because the charging process directly affects the heat transfer performance

occurring in a heat pipe, a theoretical analysis predicting the charging process is conducted. The results provide a guideline for the charging process.

CHAPTER 5 CONCLUSIONS

A one dimensional theoretical model predicting oscillating motion in an OHP is presented, which is valid for both open-looped and close-looped OHP. The model indicates that the oscillating motion of liquid slugs in OHP actually has the similarity with that of mass cubes linked by springs. The vapor bubbles act as spring but have different stiffness definitely. The expression of natural frequency of one OHP indicates that in addition to working liquid properties and filling ratio, the distribution of liquid plugs and vapor bubbles is also one very important parameter determining the system frequency. However this kind of distribution is highly random, which depends on the charging process, working fluid, charging ratio, orientation, heat pipe dimensions, heat transfer rate, and boundary conditions. In other words, it is very hard to determine the distribution of the liquid plugs and vapor bubbles in an OHP. Relatively much more stable heat transfer performance of OHPs indicates that average characteristics of heat transfer and fluid flow in OHPs might be meaningful to the application. The results show that in addition to the oscillating motion, the circulation exists in a closed-looped OHP (CLOHP). In other words, the average motion of liquid slugs in the CLOHP would have a fixed flow direction. And this kind of circulation is determined by the turn number or bubble numbers, and temperature drop between the evaporating and condensing sections. It is also found that sensible heat takes a large percentage of the total heat as indicted in previous investigations, but it is not always that high. Actually, the fraction of sensible heat

should have an upper limit which is determined by boundary conditions and input power. With the evaporator temperature increasing, the fraction of sensible heat increases and reaches an upper limit. And when the temperature continuously increases, the fraction goes down after it reaches the peak value. Generally higher working temperature or higher input power, the fraction of sensible heat becomes bigger. The effects of bubble numbers and gravity on the heat transfer performance of OHP are also studied. As the bubble number increases, the heat transfer performance of OHP increases,, but the system stability becomes worse. However, it canot be concluded that that with more bubbles the system is easy to startup. the prediction also shows that the gravity can enhance the heat transfer performance of an OHP.

Thin film evaporation, which occurs at the meniscus region of liquid-vapor interface, is the main heat transfer mechanism for the latent heat in an OHP. When a liquid film is formed in a microgroove, liquid film can be divided into micro meniscus region, where thin film evaporation occurs, and bulk region where heat conduction is dominated. For the bulk region, Galerkin method is employed to obtain the approximating solution. The results showed that most of the heat transferred by the liquid-vapor interface is through the thin film region. The effect of pulsating motion of liquid slugs on the heat transfer performance in a single phase flow was conducted, and found that the pulsating flow cannot enhance the convection heat transfer for a single phase flow. Because the pulsating flow and its coupled heat transfer occurring

in an OHP are much more complicated, the analysis conducted herein by using a single phase flow may not apply for the heat transfer and fluid flow phenomena occurring in an OHP. Clearly, it is necessary to conduct further investigation on this topic.

The vacuuming and charging process for a heat pipe was studied. A detailed model predicting the effects of charging tubing's diameter and length, initial non-condensable gas, and heat transfer condition from the heat pipe is developed. The model can help to select charging tubing with proper geometry, and determine the appropriate vacuuming procedure for a mass production of heat pipes. A mathematical model predicting the minimum meniscus radius occurring in the sintered particles with different sizes is developed. For uniform-size particles, the minimum meniscus radius is found equal to 0.443r. When the sintered particles are mixed with different size, the minimum meniscus radius can be predicted by $r_{c,e} = 2A_{gap} / P_{gap} = \dfrac{k^2 \sum \left(X_i R_i^2 \right) - \pi \sum \left(Y_j r_j^2 \right)}{\pi \sum \left(Y_j r_j \right)}$. The investigation conducted here can result in a better understanding of heat transfer mechanisms occurring in a high-heat-flux heat pipe. Based on the statistical analysis of particle distribution, a theoretical model predicting the effective thickness of sintered wick structure is developed including the effect of the wick structure on its thermal resistance. The model can be used to predict the heat flux effect on the thermal resistance occurring in the sintered particles in the evaporator. The theoretical results show that the pore size is non-uniformly distributed in the wick due to the particle structure arrangements.

Liquid in the wick structures with larger pore sizes will recede and dry out first as the heat transfer rate increases. The comparison indicates that the theoretical results predicted by the current model are more consistent with experimental results than that by the previous models. The theoretical analysis will assist in optimizing the heat transfer performance of sintered wicks in heat pipes and result in a better understanding of mechanisms of heat transfer and fluid flow in the sintered particles.

Reference

[1] Peterson., G. P., 1994, *an Introduction to Heat Pipes: Modeling, Testing and Application,* John Wiley & Sons, New York.

[2] Faghri, A, 1995, *Heat Pipe Science and Technology*, Taylor & Francis.

[3] Akachi, H., Plasek, F. and Stulc, P., 1996, "Pulsating Heat Pipes," *Proc. 5th Int. Heat Pipe Symp.*, Melboune, Australia, pp. 208-217.

[4] Charoensawan, P., Khandekar, S., Groll, M. and Terdtoon, P., 2003, "Closed Loop Pulsating Heat Pipes, Part A: Parametric Experimental Investigations," *Applied Thermal Engineering,* 23, pp. 2009-2020.

[5] Khandekar, S., Charoensawan, P., Khandekar, S., Groll, M. and Terdtoon, P., 2003, "Closed Loop Pulsating Heat Pipes, Part B: Visualization and Semi-empirical Modeling," *Applied Thermal Engineering*, 23, pp. 2021-2033.

[6] Zhang, X. M., Xu, J. L. and Zhou, Z. Q., 2004, "Experimental Study of a Pulsating Heat Pipe Using FC-72, Ethanol, and Water as Working Fluids," *Experimental Heat Transfer,* 17, pp. 47-67.

[7] Miyazaki, Y., 2005, "Cooling of Notebook PCS by Flexible Oscillating Heat Pipe," *Proceeding of IPACK2005, ASME InterPACK'05,* San Francisco, California, USA.

[8] Akdag, U. and Ozdemir, M., 2006, "Heat Transfer in an Oscillating Vertical Annular Liquid Column Open to Atmosphere," *Heat Mass Transfer,* 42, pp.

617-624.

[9] Shafii, M. B., Faghri, A. and Zhang, Y., 2001, “Thermal Modeling of Unlooped and Looped Pulsating Heat Pipes,” *Journal of Heat Transfer*, Vol. 123, pp. 1159-1172.

[10] Shafii, M. B., Faghri A. and Zhang, Y., 2002, “Analysis of Heat Transfer in Un-looped and Looped Pulsating Heat Pipes,” *International Journal of Numerical Methods for Heat & Fluid Flow,* Vol. 12/5, pp. 585-609.

[11] Zhang, Y. and Faghri, A., 2002, “Heat Transfer in a Pulsating Heat Pipe with Open End,” *Int. J. Heat Mass Transfer*, Vol. 45/4, pp. 755-764.

[12] Zhang, Y., Faghri, A. and Shafii, M. B., 2002, “Analysis of Liquid-vapor Pulsating Flow in a U-shaped Miniature Tube,” *Int. J. Heat Mass Transfer*, 45, pp. 2501-2508.

[13] Ma, H. B., Hanlon, M. A. and Chen, C. L., 2006, “An Investigation of Oscillating Motions in a Miniature Pulsating Heat Pipe,” *Microfluid Nanofluid*, 2, pp. 171-179.

[14] Khandekar, S. and Groll, M., 2003, “On the Definition of Pulsating Heat Pipes: an Overview,” *Proc. 5th Minsk International Seminar (Heat pipes, Heat Pumps and Refrigerators)*, Minsk, Belarus.

[15] Khandekar, S. and Groll, M., 2004, “An Insight into Thermo-Hydraulic Coupling in Pulsating Heat Pipes,” *Int. J. of Thermal Science*, Vol. 43/1, pp. 13-20.

[16] Tong, B. Y., Wong, T. N. and Ooi, K. T., 2001, “Closed-loop Pulsating Heat

Pipe," *Applied Thermal Engineering*, 21, pp. 1845-1862.

[17] Khandekar, S., Dollinger, N., and Groll, M., 2003, "Understanding Operational Regimes of Closed loop Pulsating Heat Pipe: An Experimental Study," *Applied Thermal Engineering*, Vol. 23/6, pp. 707-719.

[18] Rittidech, S., Dangeton, W. and Soponronnarit, S., 2005, "Closed-ended Oscillating Heat-pipe (CEOHP) Air-preheater for Energy Thrift in Dryer," *Applied Energy*, 81, pp. 198-208.

[19] Wang, S. and Nishio, S., 2005, "Heat Transport Characteristic in Closed Loop Oscillating Heat Pipes," *Proceeding of IPACK2005, ASME InterPACK'05*, San Francisco, California, USA.

[20] Xu, J. L. and Zhang, X. M., 2005, "Start-up and Steady Thermal Oscillation of a Pulsating Heat Pipe," *Heat Mass Transfer*, 41, pp. 685-694.

[21] Hosoda, M., Nishio, S. and Shirakashi, R., 1999, "Study of Meandering Closed-Loop Heat Transport Device," *JSME International Journal*, Series B, Vol. 42/4, pp. 737-744.

[22] Groll, M. and Khandekar, S., 2003, "Pulsating Heat Pipes: Progress and Prospects," *Proc. Int. Conf. on Energy and the Environment*, Shanghai, China.

[23] Katpradit, T., Wongratanaphisan, T., Terdtoon, P., Kamonpet, P., Polchai, A. and Akbarzadeh, A., 2005, "Correlation to Predict Heat Transfer Characteristics of a Closed End Oscillating Heat Pipe at Critical State," *Applied Thermal Engineering*, 25, pp. 2138-2151.

[24] Khandekar, S., Groll, M., Charoensawan, P. and Terdtoon, P., 2002, “Pulsating Heat Pipes: Thermo-fluidic Characteristic and Comparative Study with Single Phase Thermosyphon,” *Heat Transfer 2002, Proceeding of the Twelfth International Heat Transfer Conference*, pp. 459-464.

[25] Zhang, X., Xu, J. and Shi, H., 2004, “The Effect of the Heating Power and the Inclination Angle on the Pulsating Heat Pipe,” *Proceeding of CSEE*, (Chinese), Vol. 24/11, pp. 222-227.

[26] Gu, J., Kawaji, M. and Futamata, R., 2004, “Effects of Gravity on the Performance of Pulsating Heat Pipes,” *Journal of Thermophysics and Heat Transfer*, Vol. 18/3, pp. 370-378.

[27] Kawaji, M., 2003, “Studies of Vibration-induced Multi-phase Fluid Phenomena and Pulsating Heat Pipe Performance under Microgravity,” *Proceeding of ASME FEDSM’03, 4th ASME_JSME Joint Fluids Engineering Conference*, Honolulu, Hawaii, USA.

[28] Miyazaki, Y. and Akachi. H., 1998, “Self Excited Oscillation for Slug Flow in a Micro Channel,” *Proceedings of the 3rd International Conference on Multiphase Flow,* Lyon, France.

[29] Woon, T. N., Tong, B. Y., Lim, S. M. and Ooi, K. T., 1999, “Theoretical Modeling of Pulsating Heat Pipe,” *Proceeding of the 11th International Heat Pipe Conference*, Tokyo, Japan.

[30] Zou, Z. J., North, M. T. and Wert, K. T., 2001, “High Heat Flux Heat Pipe

Mechanism for Cooling of Electronics," *IEEE Transactions on Components and Packaging Technologies*, Vol. 24/2, pp. 220-225.

[31] Chen, J. C., 1966, "Correlation for Boiling Heat Transfer to Saturated Fluids in Convective Flow," *Ind. Eng. Chem. Proc. Design and Dev.,* Vol. 5/3, pp. 322-339.

[32] Martinelli, R. C., Boelter, L. M. K., Weinberg, E. B. and Yakahi, S., 1943, "Heat Transfer to a Fluid Flowing Periodically at Low Frequencies in a Vertical Tube," *Trans. ASME,* Vol. 65/7, pp. 789-798.

[33] Genin, L. G., Koval, A. P., Manchkha, S. P. and Sviridov, V. G., 1993, "Heat Transfer and Friction for Pulsating Water Flow in a Pipe," *Heat Transfer Res.* Vol. 25/2, pp. 192-195.

[34] Barker, A. R. and Williams, J. E. F., 2000, "Transient Measurement of the Heat Transfer Coefficient in Unsteady, Turbulent Pipe Flow," *Int. J. Heat Mass Transfer*, 43, pp. 3197-3207.

[35] Park, J. S., Taylor, M. F., and McEligot, D. M., 1982, "Heat Transfer to Pulsating, Turbulent Gas Flow," *Proceeding of the 7th International Heat Transfer Conference*, 3, pp. 105-110.

[36] Havemann, H. A., and Rao, N. N. N., 1954, "Heat Transfer in Pulsating Flow," *Nature*, 174/41.

[37] Karamercan, O. E. and Gainer, J. L., 1979, "The Effect of Pulsations on Heat Transfer," *Ind. Eng. Chem. Fundam.*, Vol. 18/1, pp. 11-15.

[38] West, F. B. and Taylor, A. T., 1952, "The effect of Pulsations on Heat Transfer

(turbulent flow of water inside tubes)," *Chem. Eng. Progress*, Vol. 48/1, pp. 39-43.

[39] Lemlich, R., 1961, "Vibration and Pulsation Boost Heat Transfer," Chem. Eng., Vol. 68/10, pp. 171-176.

[40] Dec, J. E., Keller, J. O. and Arpaci, V. S., 1992, "Heat Transfer Enhancement in the Oscillating Turbulent Flow of a Pulse Combustor Tail Pipe," *Int. J. Heat Mass Transfer*, Vol. 35/9, pp. 2311-2325.

[41] Holley, B. and Faghri, A., 2005, "Analysis of Pulsating Heat Pipe with Capillary Wick and Varying Channel Diameter", *International Journal of Heat and Mass Transfer,* 48, pp.2635-2651.

[42] Ma, H. B., Peterson, G. P., 1997, "Temperature Variation and Heat Transfer in Triangular Grooves with an Evaporating Film," *Journal of Thermophysics and Heat Transfer,* Vol. 11/1, pp. 90-97.

[43] Demsky, S. M., Ma, H. B., 2004, "Thin Film Evaporation on a Curved Surface," *Microscale Thermophysical Engineerimg,* 8, pp. 285-299.

[44] Womersly, J. R., 1955, "Oscillatory Motion of a Viscous Liquid in a Thin-walled Elastic Tube-I: The Linear Approximation for Long waves," *Philosophical Magazine,* 46, pp. 199-221.

[45] Uchida, S., 1956, "The Pulsating Viscous Flow Superimposed on the Steady Laminar Motion of Incompressible Fluid in a Circular Pipe," *ZAMP*, 7, pp. 403-422.

[46] Faghri, M., Javadani, K. and Faghri, A., 1979, “Heat Transfer with Laminar Pulsating Flow in a Pipe,” *Lett. Heat Mass Transfer*, **6**, pp. 259-270.

[47] Zhao, T. and Cheng, P., 1995, “A Numerical Solution of Laminar Forced Convection in a Heated Pipe subjected to a Reciprocating Flow,” *Int. J. Heat Mass Transfer*, Vol. 38/16, pp. 3011-3022.

[48] Yu, J., Li, Z. and Zhao, T., 2004, “An Analytical Study of Pulsating Laminar Heat Convection in a Circular Tube with Constant Heat Flux,” *International Journal of Heat and Mass Transfer*, 47, pp. 5297-5310.

[49] Moschandreou, T. and Zamir, M., 1997, “Heat Transfer in a Tube with Pulsating Flow and Constant Heat Flux,” *Int. J. Heat Mass Transfer*, Vol. 40/10, pp. 2461-2466.

[50] Hemida, H. N., Sabry, M. N., Abdel-Rahim, A. and Mansour, H., 2002, “Theoretical Analysis of Heat Transfer in Laminar Pulsating Flow,” *International Journal of Heat and Mass Transfer*, 45, pp. 1767-1780.

[51] Hanlon, M. A., and H. B. Ma, 2003, “Evaporation Heat Transfer in Sintered Porous Media,” *ASME Journal of Heat Transfer*, 125, pp. 644-653

[52] Peterson, G. P., 1994, An Introduction to Heat Pipe, John Wiley & Sons, Inc.,.

[53] Faghri, A., 1995, Heat pipe science and technology, Taylor & Francis, USA.

[54] Harr, M. E., 1977, Mechanics of particulate media: a probabilistic approach, McGraw-Hill, New York, Chap. 1.

[55] Graton, L. C., Fraser, H. J., 1935, “Systematic packing of spheres with particular relation to porosity and permeability,” *J. Geology*, Vol. 43/8, pp. 785-909.

[56] Rodriguez, J., Allibert, C. H., and Chaix, J. M., 1986, “A Computer Method for Random Packing of Spheres of Unequal Size,” *Powder Tech*., 47, pp. 25 –33.

[57] Yang, R. Y., Zou, R. P., and Yu, A. B., 2003, “Effect of material properties on the packing of fine particles,” *J. App. Phys*., 94, pp. 3025-3034.

[58] Kurashige, M., Mishima, M., Imai, K., 1999, “Simulated effective thermal conductivity of sintered, randomly packed sphere and statistical structure of packing,” *J Thermal Stresses*, 22, pp.713 –733.

[59] Chi, S. W., 1976, Heat Pipe Theory and Practice, McGraw-Hill, New York.

[60] Ferrell, J. K., and Alleavitch J., 1970, “Vaporization heat transfer in capillary wick structures”, *Chemical Engineering Progress, Symp. Ser.*, 66(102), pp. 82-91.

[61] Luikov, A.V., 1980, Heat and Mass Transfer, Chapter 5, Transport Phenomena in Capillary-Porous Bodies, Mir Publishers, Moscow.

[62] Borgermeyer, B. and Ma, H., 2007, “Experimental investigation of oscillating motions in a flat plate pulsating heat pipe”, *J. Thermophysics and Heat Transfer*, 21(2), pp. 405-409.

[63] Chang, J. Y., Vadakkan, U., Prasher, R., and Prstic, S., 2005, “Thermal performance of vapor chambers under hot spot heating conditions”, *Proceeding of InterPack 2005*, San Francisco, CA, USA

[64] Dunn, P.D. and Reay, D. A., 1994, *Heat Pipes*, 4th edition, Pergamon, Elsevier Science Inc.,

New York.

Vita

Peng Cheng was born in Changzhi, Shanxi Province, China, in 1979. He went to high school in 1995, and after three years learning, entered the Tsinghua University, China, in 1998. His major of undergraduate was Engineering Mechanics. After graduation in summer 2002, he continued his study in Dr. Chunxiao Xu's turbulence lab in Tsinghua University for two and a half of years, and obtained Master of Science in Engineering in winter of 2004. His master thesis focused on the Large Eddy Simulation of atmospheric flow in a city scale, in which the dispersion of pollutant released by power plants or vehicles along complicated city terrain was one important objective. He joined Dr. Hongbin Ma's thermal lab in January 2005 as research assistant, pursuing his Ph.D degree in the department of Mechanical & Aerospace Engineering in University of Missouri-Columbia. His research focused on the working mechanism of Oscillating Heat Pipe, Thin Film Evaporation and Meniscus Radius of Sintered wick. After graduation, he will continue his research in the filed of thermal management, in Dr. Ma's lab with postdoctoral fellowship.